Propagation Properties of Duobinary Transmission in Optical Fibers

by

Leaf Alden Jiang

Submitted to the Department of Electrical Engineering and Computer Science

in partial fulfillment of the requirements for the degrees of

Bachelor of Science in Computer Science and Engineering

and

Master of Electrical Engineering

at the

MASSACHUSETTS INSTITUTE OF TECHNOLOGY

May 1998

Author ....

Department of Electrical Engineering and Computer Science

May 8, 1998

Certified by. .....

Per B. Hansen

Member of the Technical Staff, Bell Laboratories

Thesis Supervisor

Certified by... .....

Erich Ippen

Professor

Thesis Supervisor

Accepted by ....

Arthur C. Smith

Chairman, Department Committee on Graduate Students

Propagation Properties of Duobinary Transmission in Optical Fibers

by

Leaf Alden Jiang

Submitted to the Department of Electrical Engineering and Computer Science
on May 8, 1998, in partial fulfillment of the
requirements for the degrees of
Bachelor of Science in Computer Science and Engineering
and
Master of Electrical Engineering

Abstract

The propagation properties of duobinary encoded optical signals are investigated. Three variations of duobinary encoding are presented: AM-PSK, alternating-phase, and blocked-phase. A computational model for optical transmission of duobinary signals is developed, which gives insight into the issue of optimal filtering in duobinary transmission systems. The main result is that the baseband electrical filters in the transmitter and receiver should have a bandwidth at approximately 0.6 the bitrate and have a slow roll-off. The relationship between noise and dispersion penalty in an optically pre-amplified receiver is then discussed. It is found that the ratio of the noise power of the marks to the spaces determines the rate at which the receiver sensitivity degrades as the channel dispersion is increased. Next, the stimulated Brillouin scattering threshold of duobinary signals is experimentally and theoretically shown to increase linearly with bitrate, and compared to binary modulation format at 20 Gbit/s, a forty-fold increase in launch power is possible. Finally, the computational model for optical transmission is used to show that duobinary format has a greater channel efficiency than binary format. This is important for tighter channel spacing in wavelength-division multiplexed optical channels.

Thesis Supervisor: Per B. Hansen
Title: Member of the Technical Staff, Bell Laboratories

Thesis Supervisor: Erich Ippen
Title: Professor

Acknowledgments

First and foremost, I would like to thank my mentor at Bell Labs, Per Hansen, for taking me under his tutelage, answering all my questions, adding valuable insights, making sure that I made progress, taking an active role in my research, having a positive and friendly personality and making this thesis possible. I would also like to thank Torben Nielsen, a member of the technical staff at Bell Labs, for his invaluable help with setting up equipment in the lab, providing much of the computer code to control the GPIB equipment, helping me fix the numerous bugs in my simulator, and answering many of my questions.

I would like to thank my family for their enormous support throughout the years, for the countless hours they saved me by cooking dinners, preparing lunches, doing the laundry, cleaning up my room, always making sure that I was nurished and rested, and letting me set up one of the rooms in our house exclusively for studying and working on this thesis.

I would like to thank Prof. Ippen for visiting me several times at Bell Labs, providing valuable input regarding FWM and SBS, and advising my thesis. I would also like to thank the VI-A office for their continued efforts in running the VI-A program.

Contents

List of Figures

List of Tables

Chapter 1

Introduction

Ideas from communication theory developed originally for microwaves and electrical signals are often applied to optical signals. Duobinary transmission is one such idea that was developed in the early 1960's in the context of electrical signals and was later applied to optical signals in fibers in the late 1990's.

As the demand for faster communications increases, there has been a natural evolution towards a better usage of channel bandwidth. In the radio and microwave domains, radios, televisions, and especially cellular phones have led to efficient usage of the scarce and precious channel spectrum through the usage of bandwidth efficient modulation techniques: single-sideband modulation, time division multiplexing, and M-ary signaling schemes for example. In comparison, optical communications in fiber has such a large usable bandwidth that efficient channel usage has not been an issue until recently. Since spectral efficiency was previously not an issue in optical fiber communications, binary NRZ modulation is still currently the most popular modulation format in optical fibers due to its simplicity of implementation. One way of achieving a more efficient use of the channel bandwidth was through innovative coding schemes called partial response signaling (PRS). PRS is a method of encoding or decoding a data stream in order to decrease the amount of error from intersymbol interference (ISI). Duobinary format is a common form of partial response signaling. A binary datastream can be encoded into a duobinary signal simply by adding the binary data stream to a one bit delayed version of itself. The result is a three-level

signal.

Lender was one of the first to publish on duobinary signaling [24] [25]. He pointed out that the advantage of using duobinary signaling in electrical lines is that a bit rate of $2B$ can be sustained in a channel of single-sided bandwidth B with a reduced amount of ISI and without the need for ideal low-pass rectangular baseband filters as would be necessary to achieve the same performance using binary format.

Up until the 1990's, fiber optic communications had plenty of bandwidth. Just as had happened in the microwave spectrum in the 1960's, bit rates and number of channels in optical fibers started to increase and fill the 3 THz bandwidth of erbium-doped fiber amplifiers (EDFA). Very quickly, the bandwidth of the entire amplifier was used by densely-packed wavelength-division multiplexed (WDM) binary channels[9] [10] [8] [11]. In these experiments, terabit per second bit rates over $\approx$100 km were reported. The next step after filling the bandwidth of EDFAs was to increase the spectral efficiency (the bit rate divided by the used bandwidth) by using a different modulation format. Usage of coherent techniques with a local-oscillator proves to be very difficult in fiber since slight perturbations in the signal's phase can easily cause a dramatic increase in the bit error rate. Duobinary format is the natural next step in improving the bandwidth efficiency since it has a compressed spectrum and the receiver does not have a local-oscillator. In a fairly recent experiment using 132 20 Gbit/s duobinary modulated channels with 33.3 GHz spacing, 2.6 Tbit/s over 120 km (corresponding to a spectral efficiency of 0.6 bit/s/Hz) was demonstrated, a factor of two improvement over densely packed binary channels [55]. In the the 1997 Optical Fiber Conference, the feasibility of over 1 bit/s Hz high spectral efficiency WDM with optical duobinary coding and polarization interleave multiplexing was considered [21].

Besides a thrust toward a more efficient use of available optical bandwidth, the recent interest in duobinary signaling in optical fibers grew from its low stimulated Brillouin scattering (SBS) threshold and its narrow spectrum. As optical modulators increase in speed from 2.5 Gbit/s to 10 Gbit/s, and now to about 40 Gbit/s, dispersion becomes a more important issue. The spectral width of duobinary signals is about half of that of binary signals and since a narrower spectrum implies a

smaller dispersion power penalties, duobinary signals help alleviate the problem of ever increasing modulation rates. Increased modulation rates lead to other problems as well. A higher launch power is necessary to obtain the same BER when increasing the modulation rate. Stimulated Brillouin backscattering (SBS) presents an upper limit to the launch power of an NRZ signal. This upper limit is called the SBS threshold. Duobinary signals have higher SBS thresholds than binary signals since binary signals have a large spectral component at the carrier frequency, not present in the duobinary power spectral density (psd), which efficiently scatters from acoustic waves in the fiber at high launch powers.

The rediscovery of duobinary transmission in optical fibers has prompted a deluge of research to use this transmission format to increase capacity of fiber while still offering reasonable hardware (receiver and transmitter) realizations. One of the first duobinary experiments (in 1994) was the propagation of a three-level optical duobinary signal over an unrepeatered 100 km span of silica core fiber [18]. Even though the back-to-back receiver sensitivity (at a BER of 10^{-9}) of the three-level duobinary format was 3 dB lower than binary format, the receiver sensitivity after 100 km of transmission through silica-core fiber using duobinary format was 2 dB better than binary format. One year later (1995), a simple optical modulation scheme yielding an AM-PSK duobinary optical signal using a lithium niobate Mach-Zender modulator driven by an electrical three-level duobinary signal was proposed [40]. This scheme proved to be advantageous over the previous three-level optical level scheme since it yielded a two-level intensity signal in the fiber which allowed for direct detection and a better back-to-back sensitivity. In the same year a 210 km repeaterless 10 Gbit/s transmission experiment through nondispersion-shifted fiber (17 ps/nm/km) with a measured bit error ratio lower than 10^{-12} was performed [41]. In comparison, 10 Gbit/s binary transmission through nondispersion-shifted fiber achieves the same BER at about 60-80 km of nondispersion-shifted fiber. A year later (1996), duobinary transmission was coupled with fiber-grating based compensation and 100 km spans between EDFAs to yield 10 Gbit/s transmission over 700 km of standard single-mode fiber, the longest distance achieved at 10 Gbit/s using a single dispersion

compensating element to that date [27].

To summarize, the four attractive features of duobinary modulation in optical fiber transmission are: (1) it has a narrower bandwidth than binary format and hence suffers less from dispersion, (2) it has a greater spectral efficiency than binary format due to its narrower bandwidth and hence allows tighter packing of wavelength division multiplexed channels, (3) it suffers less from stimulated Brillouin backscattering, the major limiting factor in repeaterless transmission, and (4) is easy to implement since the transmitter only requires modest changes from an externally modulated binary transmitter and since the receiver is a direct detection receiver, the same as for binary format.

This thesis will discuss, clarify, and raise several major issues concerning the propagation properties of duobinary transmission in optical fibers. Chapter 2 introduces duobinary signaling, the components necessary for its generation, and practical issues and difficulties in constructing a high performance duobinary transmitter. Chapter 3 presents the model used in this thesis to simulate duobinary systems, and contains an overview of the simulator, algorithms for calculating the BER and sensitivity of duobinary receivers, and a clarification of confusing nomenclature. The noise terms of an optically pre-amplified receiver are then analytically derived. Various simplifications of the noise variances are explained and justified. Chapter 4 implements the simulator to gain insights into *why* duobinary signaling has better transmission properties than binary signaling. There was much confusion over this issue and several different explanations existed [36] [52]. It is important to understand the improved propagation properties of duobinary signaling in order to pick optimal system parameters such as the transmitter and receiver electrical filter bandwidths. The issue of optimal filtering from a set of common filters will be discussed. RZ duobinary signals are considered as well. Chapter 6 provides an extensive account of the stimulated Brillouin scattering (SBS) of a duobinary signal. The duobinary power density spectrum and SBS threshold are found analytically. Simulations and experimental data agree quite well with the theoretically predicted SBS thresholds for the NRZ duobinary formats. Chapter 7 discusses duobinary transmission in the context of

wavelength-division multiplexing. The benefit of duobinary transmission in multi-channel systems is due to the narrow spectrum of duobinary signals and allows for tighter packing of channels. Finally, future directions and research are presented.

Chapter 2

Duobinary Signal Format

2.1 Duobinary Signaling

Duobinary signaling codes a binary bit stream by adding the bit stream to itself shifted by one position to the right (see figure 2-1). For example, the binary bit sequence 10110010 is encoded into a three-level duobinary sequence by delaying the binary sequence by one bit and adding it to itself. The first three lines in figure 2-2 illustrate duobinary encoding. The first bit of the shifted binary sequence is arbitrarily chosen as 0.

The transfer function of the duobinary encoder in figure 2-1 is easily seen to be $H(z) = 1+z^{-1}$. To decode a duobinary signal, the inverse transfer function is needed so that $H(z)G(z) = 1$. The duobinary decoder is $G(z) = 1/(1+z^{-1})$ and is equivalent to subtracting a previous output from the current input to obtain the current output. The recovered binary sequence in figure 2-2 assumes that the initial state of the decoder is 0 which must match the arbitrarily chosen first bit of the shifted binary sequence in the encoder.

One problem with duobinary encoding is that errors tend to propagate since the

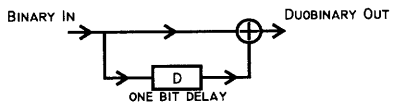

Figure 2-1: Construction of a duobinary signal from a binary signal

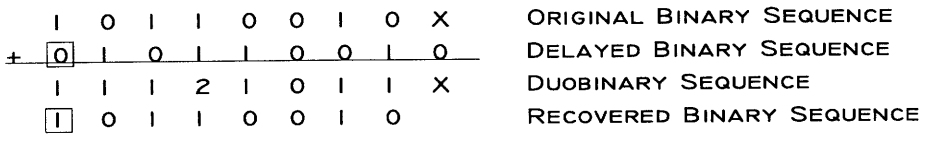

Figure 2-2: Example of creating a duobinary signal from a binary signal

output of the decoder is dependent on previous, possibly fallacious, output. If the previous output is incorrect, so will subsequent output. This problem has been solved precoding the input binary data stream. The transfer function of the precoding is simply $P(z) = 1/(1 - z^{-1})$ [18].

Instead of having levels at 0, 1, and 2; the levels could easily be biased so that they are -1, 0, and 1. With the new levels, the upper and lower levels differ from each other by a π-phase shift. This is called amplitude-modulated phase shift keying duobinary modulation (or AM-PSK duobinary) where the "PSK" denotes the π-phase shifts.

2.2 Generation of Duobinary Signals

This section will explain how a duobinary signal is generated in the electrical and optical domain.

A duobinary transmitter is shown in figure 2-3. A continuous wave or pulsed lightwave generated by a laser diode is modulated by an external Mach-Zender (MZ) modulator. The two arms of the MZ modulator are driven by two electrical signals in push-pull fashion.[1] The two electrical signals driving the MZ modulator are duobinary encoded and filtered data bits.

2.2.1 The Optical Section of the Duobinary Transmitter

The laser diode and the Mach-Zender(MZ) modulator make up the optical section of the duobinary transmitter. In the experiments in this thesis, laser diodes lasing in the 1.5 μm telecommunications window were used. The Mach-Zender modulator

[1]Push-pull means that each arm of the MZ are driven by opposite voltages. For example, if one arm of the modulator has voltage +V, the other arm has voltage -V. Push-pull operation avoids chirping of the output signal.

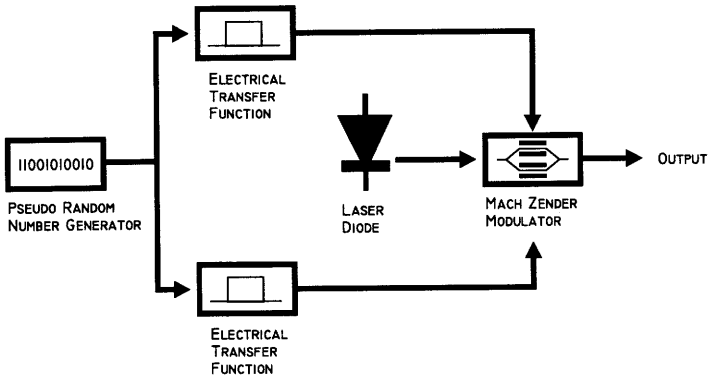

Figure 2-3: A duobinary transmitter.

splits an incoming light signal into two waveguide branches (see figure 2-4). The two branches experience different optical delays, depending on the voltage applied to each arm, and then recombine constructively or destructively. If the electric field in the upper branch experiences a phase shift of

$$\phi_1 = \frac{V_1}{V_\pi}\pi \tag{2.1}$$

and the electric field in the lower arm experiences a phase shift of

$$\phi_2 = \frac{V_2}{V_\pi}\pi \tag{2.2}$$

then the output electric field is given by

$$E_{out} = \frac{E_{in}}{\sqrt{2}}\left(e^{i\phi_1} + e^{i\phi_2 + i\phi_0}\right) \tag{2.3}$$

where ϕ_0 is the phase shift due to the biasing voltage. Expressing (2.3) in terms of voltage yields

$$E_{out} = \sqrt{2}E_{in}e^{i\left(\frac{V_1+V_2}{2V_\pi}\pi + \frac{\phi_0}{2}\right)}\cos\left(\frac{V_1 - V_2}{2V_\pi}\pi - \frac{\phi_0}{2}\right) \tag{2.4}$$

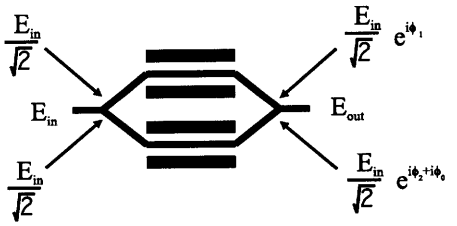

Figure 2-4: Mach-Zender modulator and respective E-fields.

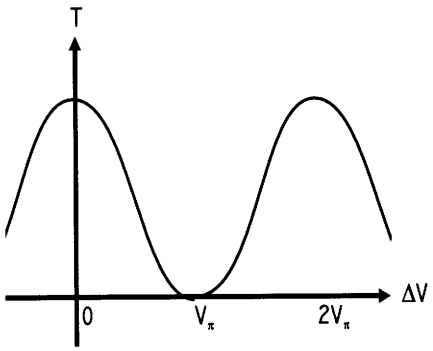

Figure 2-5: Transmission as a function of electrode voltage difference of the MZ modulator

Using (2.4) and the definition $\Delta V = V_1 - V_2$, the output power of the MZ can be expressed as

$$|E_{out}|^2 = 2E_{in}^2 \cos^2\left(\frac{\Delta V}{2V_\pi}\pi - \frac{\phi_0}{2}\right) \tag{2.5}$$

and the chirp, which is the derivative of the phase of E_{out} ($\delta\omega = 2\pi d\phi(t)/dt$) is

$$\delta\omega = \frac{\pi}{2V_p i}\frac{d}{dt}(V_1 + V_2)\,. \tag{2.6}$$

The transmission through the MZ is sinusoidal with respect to the difference of voltages applied through the electrodes, V_1 and V_2 (see equation (2.5) and figure 2-5). In addition, to have a chirpless output ($\delta\omega = 0$), equation (2.6) implies $V_1 = -V_2$. This condition is the same as push-pull operation.

2.2.2 The Electrical Section of the Duobinary Transmitter

The electrical section of the duobinary transmitter consists of a data generator, a duobinary encoder and a low-pass filter. For transmission experiments, the data

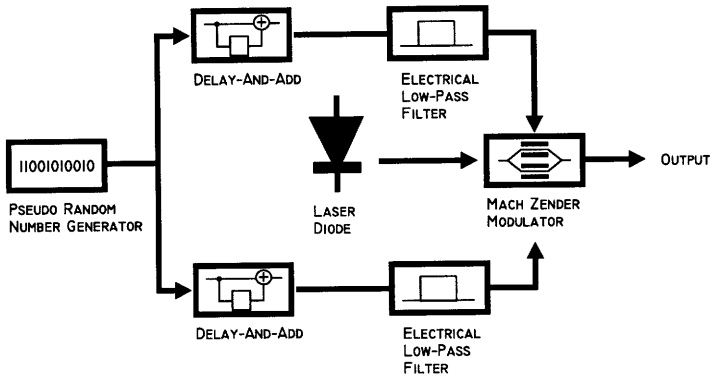

Figure 2-6: Push-pull or AM-PSK duobinary transmitter. The delay, τ, is one-bit period.

generator is often a pseudo-random bit sequence which has properties of random data.

Pseudo-random data generation has three properties that reflect the data's randomness [16]. Firstly, the number of marks and spaces (or zeros and ones) in a sequence differ by at most 1. Secondly, the probability of a contiguous string of marks or a continugous string of spaces is inversely proportional to the length of the string. This means that among the number of runs of marks or spaces in the pseudorandom binary sequence (PRBS), one-half the runs of each kind are of length one, one-fourth are length two, one-eighth are length three, and so on. Finally, the autocorrelation of the PRBS is approximately zero everywhere except at the origin. The generation of a PRBS sequence is often implemented by using a shift register with feedback. A good discussion of how to generate pseudorandom binary sequences can be found in [22, p.284].

For an AM-PSK duobinary transmitter (see figure 2-6), the MZ modulator is biased so that when $\Delta V = 0$ the transfer function in figure 2-5 is at a null. The delay-and-add element in figure 2-6 can be replaced by an analog low-pass filter (LPF) with a cutoff at 1/4 the bitrate. This filter will also produce a three-level signal. The electrical LPF following the delay-and-add block represents the limited bandwidth of the driving electronics, inserted electrical filters, and electrical amplifiers. When the cutoff of this filter is chosen correctly (namely at 6.5 the bitrate), the spectral narrowing of the duobinary signal is actually beneficial.

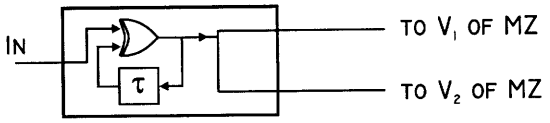

Figure 2-7: Alternating phase duobinary encoder.

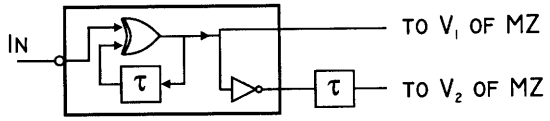

Figure 2-8: Blocked phase duobinary encoder.

The problem with AM-PSK duobinary modulation is that it is difficult to generate a high-speed (>10Gbit/s) three-level electrical signal. Each MZ modulator is rated with the voltage, V_π, necessary to go from maximum to minimum transmission thru the MZ. This voltage is often higher than what can be generated with a bit error rate test set (BERT) and necessitates the use of electrical amplifiers. Amplification of a three-level signal is especially troublesome since amplifiers usually operate in saturation. This means that the middle-level, if not saturated already, will probably lie asymmetrically between the upper and lower levels. In order to achieve a good optical eyepattern, the electrical signal fed into the MZ modulator should have its middle-level located half-way between the high and low electrical levels. Often this is very difficult to achieve. A two-level scheme would be much simpler to implement for this reason. In addition, modulation between a "-1" and "+1" requires a $2V_\pi$ voltage swing — twice as much as what is necessary for binary modulation.

There are two schemes to achieve duobinary modulation with two-level electrical signals: alternating phase duobinary and blocked-phase duobinary modulation (see figure 2-7 and 2-8). These schemes use a differential encoder and some delay elements.

Unfortunately, both alternating-phase duobinary modulation and blocked phase duobinary modulation are not push-pull schemes, and hence the output from the MZ is chirped when operating in NRZ mode. On the other hand, the chirping is not seen when using an RZ pulse source since the chirping occurs at the transition edges of the electrical signals. Hence, if the electrical signal is delayed relative to the optical pulse stream so that the optical signal has zero intensity on the transition edges of

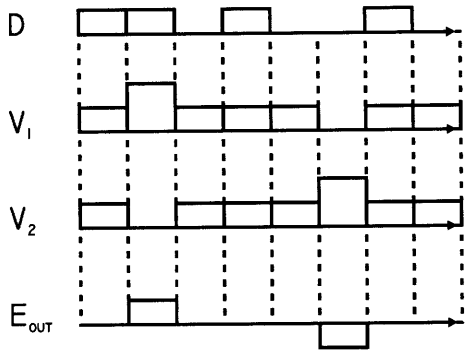

Figure 2-9: AM-PSK duobinary encoding of 8 random bits.

the electrical signal, the output light will be chirpless. The simulated sensitivities for RZ linear transmission systems will be discussed in chapter 4.

2.3 Binary PAM Signals Overview

In the previous section, we saw how to generate AM-PSK, alternating phase, and blocked phase duobinary signals. This section will give a qualitative feel for how these signals look in the time domain by illustrating several eyepatterns.

Figure 2-9, 2-10, and 2-11 show the AM-PSK, blocked phase, and alternating phase duobinary encoding on a sample input data pattern, D, with a length of 8 bits. The symbols V_1 and V_2 represent the voltages on both arms of the MZ modulator, and E_{out} is the optical field output from the MZ which is simply $E_{out} = V_1 - V_2$ when the MZ is biased correctly and the electronics have infinite bandwidth. AM-PSK duobinary signals never have a transition between "-1" and "+1" levels between neighboring bits. This means that the modulation is never driven between two extremes (ΔV from 0 to $2V_\pi$)) on the ΔV versus MZ transmission plot in figure 2-5. This is an advantageous property of AM-PSK duobinary modulation since it requires time for the finite bandwidth electronics to effect a large swing of $2V_\pi$ volts. The longer it takes the electronics to drive the arms on the MZ from 0 to $2V_\pi$, the more closed the transmitted eye will be. Unfortunately, alternating-phase and blocked-phase duobinary signals can have transitions between "-1" and "1" between neighboring bits.

Throughout this thesis, simulations will be used to gain insights into several issues

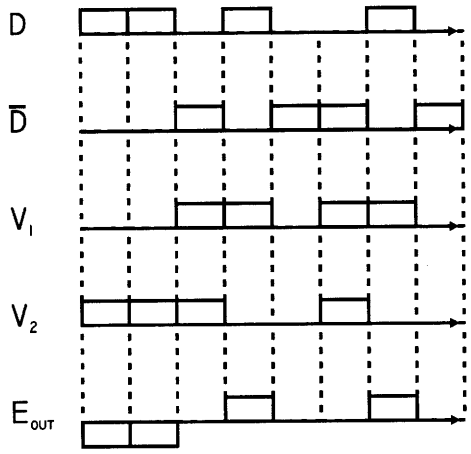

Figure 2-10: Blocked-phase duobinary encoding of 8 random bits.

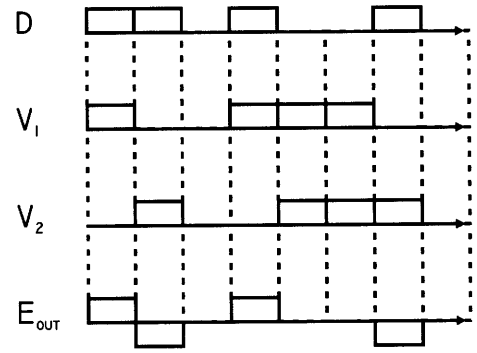

Figure 2-11: Alternating-phase duobinary encoding of 8 random bits.

concerning duobinary format. The fundamental question is whether or not these simulations simulate reality. A simple check would be to compare simulated and real eyepatterns for NRZ binary signals. Figure 2-12 shows just that. The left-hand column contains eye diagrams of binary modulated signals obtained from a sampling scope for different lengths of fiber (0 to 60 km). The right-hand column shows the corresponding simulated eyepatterns.

The reader may be wondering how the eyepatterns of binary, AM-PSK duobinary, alternating phase duobinary, and blocked phase duobinary formats compare. Figure 2-13 shows the eyepatterns for these formats at 0 and 80 km. At 0 km, the alternating phase duobinary format eyepattern differs from the AM-PSK and blocked phase duobinary format eyepatterns since the electrical filter in the transmitter has a 3-dB cutoff at the bit rate rather than at half the bit rate. As will be seen in chapter 6, alternating phase duobinary has its first null at the bitrate whereas the other two duobinary formats have their first null at half the bitrate. At 100 km, the alternating phase and blocked phase duobinary formats are seriously degraded due to the chirp on their pulse edges.

2.4 Autocorrelation and Power Spectral Densities of Binary PAM Signals

Determination of the stimulated Brillouin backscattering threshold for binary pulse amplitude modulated (PAM) signals in chapter 6 and interpreting the results of propagation simulations in chapter 4 requires the understanding of the autocorrelation function and power spectral densities of binary PAM signals. This section will derive the autocorrelation function and power spectral density for NRZ Binary, NRZ AM-PSK duobinary, NRZ alternating phase duobinary, NRZ blocked phase duobinary, RZ Binary, RZ alternating phase duobinary, and RZ blocked phase duobinary signals in respective order. The main results are given by equations (2.23), (2.25), (2.26), (2.27), (2.33), (2.35), and (2.36) for the power spectral densities and (2.20), (2.24),

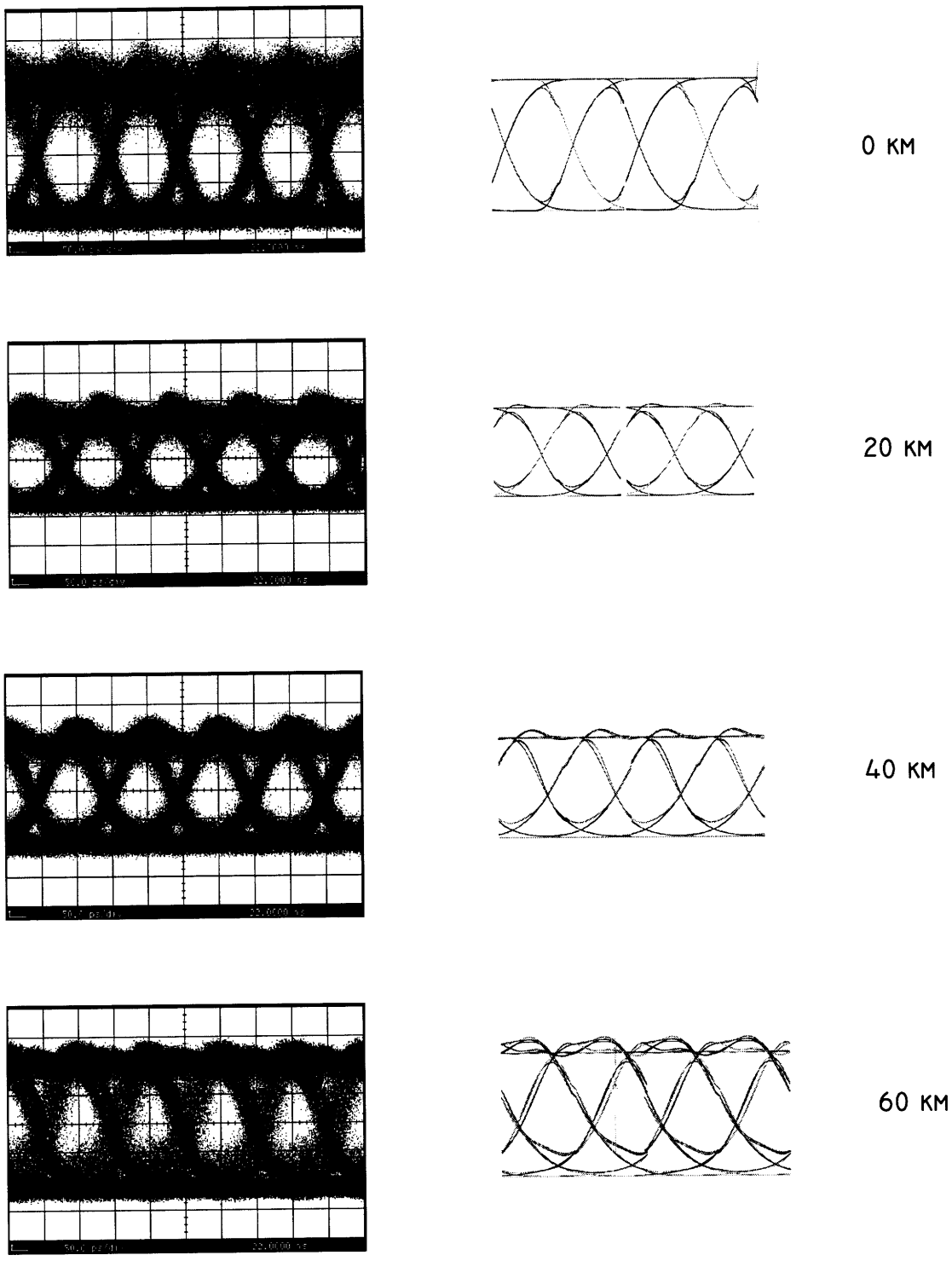

Figure 2-12: A comparison of experimental eyepatterns versus simulated eyepatterns at 0 and 80 km of standard silica core fiber (17 ps/nm/km).

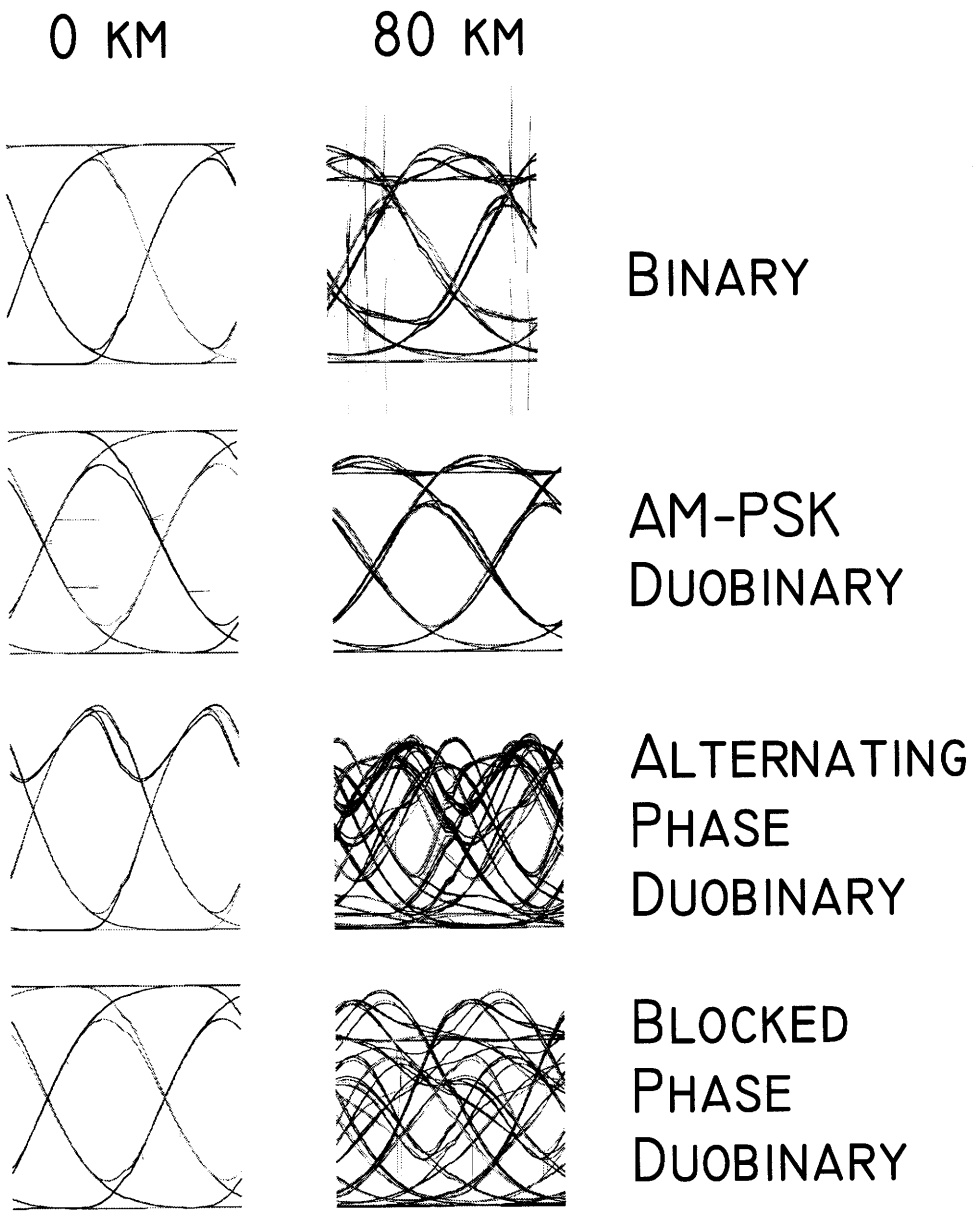

Figure 2-13: A comparison of experimental eyepatterns versus simulated eyepatterns at several lengths of standard silica core fiber (17 ps/nm/km).

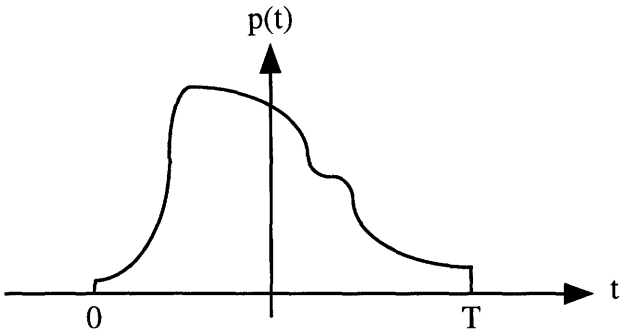

Figure 2-14: An arbitrary pulse shape of a mark. Notice that the pulse is defined to be zero outside the interval $0 < t < T$.

and (2.32) for the autocorrelation functions.

2.4.1 NRZ Binary Format

Consider the random binary signal that alternates between the values $\pm\frac{A}{2}$. A signal of this form can be represented as

$$X(t) = \sum_k a_k p(t - kT) \tag{2.7}$$

where T is the bit rate period ($T = 100$ ps in the case of 10 GBit/s), $p(t - kT)$ for $0 < t < T$ is the pulse shape of the kth bit (see figure 2-14), and $a_k = \pm 1$. For the NRZ binary signal, the pulse shape is taken to be a perfect square of height $A/2$. The autocorrelation of the stationary, ergodic NRZ binary random process is calculated by considering two intervals: $|\tau| \leq T$ and $|\tau| > T$. For the case that $|\tau| \leq T$,

$$R_{XX}(\tau \mid |\tau| < T) = E\{X(t)X(t-\tau)\} = \sum_{i=1}^{4} E\{X(t)X(t-\tau) \mid B_i\} P(B_i) \tag{2.8}$$

where the autocorrelation is computed by integrating over the first bit slot ($0 < t < T$) and the events B_i are conditions on the adjacent pair of overlapping bits in the region $0 < t < T$. These events are defined in table 2.1. Assuming that X(t) is ergodic, (2.8) can be written as a time average:

$$R_{xx}(\tau \mid 0 < \tau < T)$$

Event	$a_{-1}(B_i)$	$a_0(B_i)$	$P(B_i)$
B_1	1	1	1/4
B_2	1	-1	1/4
B_3	-1	1	1/4
B_4	-1	-1	1/4

Table 2.1: Events corrsponding to the value of the first and second bit in the random binary process X(t).

$$
\begin{aligned}
&= \sum_{i=1}^{4} \frac{1}{T} \int_0^T X_i(t) X_i(t-\tau) dt P(B_i) \\
&= \sum_{i=1}^{4} \frac{1}{T} \int_0^T \sum_{k=-\infty}^{k=\infty} a_k(B_i) p(t-kT) \sum_{m=-\infty}^{\infty} a_m(B_i) p(t-\tau-kT) dt P(B_i) \quad (2.9) \\
&= \sum_{i=1}^{4} \frac{1}{T} \int_0^T a_0(B_i) p(t) \left[a_{-1}(B_i) p(t-\tau+T) + a_0(B_i) p(t-\tau) \right] dt P(B_i) \\
&= \sum_{i=1}^{4} \frac{1}{T} \left[\int_0^{\tau} a_0(B_i) a_{-1}(B_i) p(t) p(t-\tau+T) dt \right. \\
&\quad \left. + \int_{\tau}^{T} a_0(B_i) a_0(B_i) p(t) p(t-\tau) \right] P(B_i) \quad (2.10) \\
&= \frac{1}{T} \int_0^T p(t) p(t-\tau+T) dt E\left\{a_0 a_{-1}\right\} + \frac{1}{T} \int_0^T p(t) p(t-\tau) dt E\left\{a_0 a_0\right\} \quad (2.11) \\
&= \frac{1}{T} p(\tau) * p(-\tau) * \delta(\tau - T) E\left\{a_0 a_{-1}\right\} + \frac{1}{T} p(\tau) * p(-\tau) E\left\{a_0 a_0\right\} \quad (2.12) \\
&= \frac{1}{T} \left\{ 0 + \frac{(T-\tau) A^2}{4} \right\} \\
&= \frac{A^2}{4} \left(1 - \frac{\tau}{T} \right), \qquad 0 < \tau < T \quad (2.13)
\end{aligned}
$$

The integration in (2.9) is computed over one bit slot with pulses that are assumed to be perfect rectangles. In step (2.11), the limits of the integral were extended from 0 to T since $p(t-\tau)$ and $p(t-\tau+T)$ are zero in the extended integrated region. Figure 2-15 shows a picture of the integration which yielded (2.13).

In (2.13), τ was assumed positive. If negative τ are considered as well, (2.11) receives an extra term due to the expectation between the 0th and 1st bit slots.

$$R_{xx}(\tau \mid |\tau| < T) \quad (2.14)$$

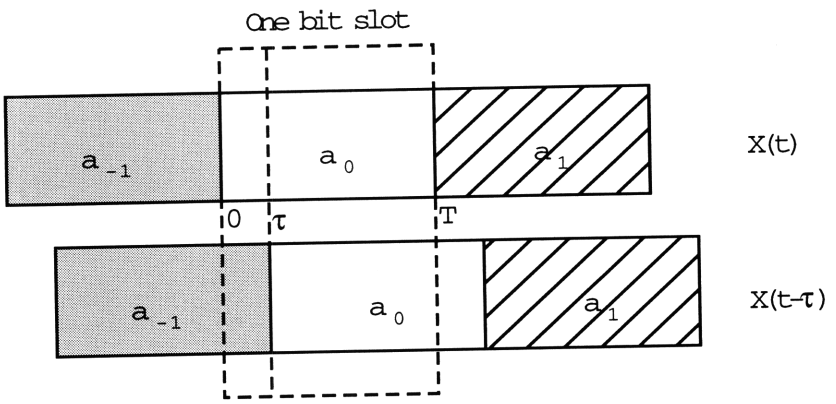

Figure 2-15: The autocorrelation of a binary signal with $0 < \tau < T$. Each box represents a bit which is either a mark or a space. The dashed boxes denote the limits of both integrals in (2.11).

$$
\begin{aligned}
&= \frac{1}{T}\int_0^T p(t)p(t-\tau+T)dtE\left\{a_0a_{-1}\right\} + \frac{1}{T}\int_0^T p(t)p(t-\tau)dtE\left\{a_0a_0\right\} \quad (2.15)\\
&\quad + \frac{1}{T}\int_0^T p(t)p(t-\tau-T)dtE\left\{a_0a_1\right\}\\
&= \frac{1}{T}p(\tau) * p(-\tau) * \delta(\tau-T)E\left\{a_0a_{-1}\right\} + \frac{1}{T}p(\tau) * p(-\tau)E\left\{a_0a_0\right\}\\
&\quad + \frac{1}{T}p(\tau) * p(-\tau) * \delta(\tau+T)E\left\{a_0a_1\right\} \quad (2.16)\\
&= \frac{1}{T}\left\{0 + \frac{(T-\tau)A^2}{4} + 0\right\}\\
&= \frac{A^2}{4}\left(1 - \frac{|\tau|}{T}\right), \qquad |\tau| < T \quad (2.17)
\end{aligned}
$$

Next, the autocorrelation for $|\tau| > T$ is considered. The event space is also given by table 2.1 except with a_{-1} replaced with a_i where $i \neq 0$. Similar to the derivation of the autocorrelation for $|\tau| < T$, (2.12), the autocorrelation for $|\tau| > T$ is

$$
\begin{aligned}
&R_{xx}(\tau \mid \tau > T)\\
&= \sum_{i=1}^{4}\frac{1}{T}\int_0^T X_i(t)X_i(t-\tau)dtP(B_i)\\
&= \sum_{i=1}^{4}\frac{1}{T}\int_0^T \sum_{k=-\infty}^{k=\infty} a_k(B_i)p(t-kT)\sum_{m=-\infty}^{\infty} a_m(B_i)p(t-\tau-kT)dtP(B_i)\\
&= \sum_{i=1}^{4}\frac{1}{T}\int_0^T a_0(B_i)p(t)\left[a_n(B_i)p(t-\tau-nT)\right.\\
&\quad \left. + a_{n+1}(B_i)p(t-\tau-(n+1)T)\right]dtP(B_i)
\end{aligned}
$$

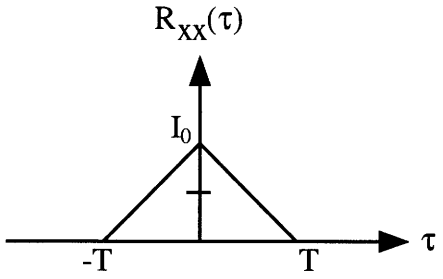

Figure 2-16: Binary signal autocorrelation function.

$$
\begin{aligned}
&= \sum_{i=1}^{4} \frac{1}{T} \left[\int_0^{\tau} a_0(B_i) a_n(B_i) p(t) p(t-\tau-nT) dt \right. \\
&\quad \left. + \int_{\tau}^{T} a_0(B_i) a_{n+1}(B_i) p(t) p(t-\tau-(n+1)T) dt \right] P(B_i) \\
&= \frac{1}{T} \left\{ \int_0^{\tau} p(t) p(t-\tau-nT) dt E\{ a_0 a_n \} \right. \\
&\quad \left. + \int_{\tau}^{T} p(t) p(t-\tau-(n+1)T) dt E\{ a_0 a_{n+1} \} \right\} \qquad (2.18) \\
&= \frac{1}{T} p(\tau) * p(-\tau) * \delta(\tau - nT) E\{ a_0 a_n \} \\
&\quad + \frac{1}{T} p(\tau) * p(-\tau) * \delta(\tau - (n+1)T) E\{ a_0 a_{n+1} \} \\
&= 0, \qquad T < \tau \qquad (2.19)
\end{aligned}
$$

Equations (2.17) and (2.19) can be combined to yield the autocorrelation of a binary signal

$$
R_{XX}(\tau) = \begin{cases} \frac{A^2}{4} \left(1 - \frac{|\tau|}{T} \right) & : \quad |\tau| < T \\ 0 & : \quad |\tau| \geq T \end{cases} \qquad (2.20)
$$

The autocorrelation is plotted in figure 2-16.

The power density spectrum of the random NRZ binary signal can be found by taking the Fourier transform of the autocorrelation, R_{XX}. This is known as the Wiener-Khintchine Theorem [2]. Therefore the spectrum is given by

$$
\begin{aligned}
I_{\text{NRZ Binary with zero mean}}(f) &= \int_{-\infty}^{\infty} R_{XX}(\tau) e^{-j2\pi f \tau} d\tau \\
&= \frac{A^2}{4} T \text{sinc}^2(\pi f T) \qquad (2.21)
\end{aligned}
$$

[2] A nice proof of this theorem is shown in [56, p.360]

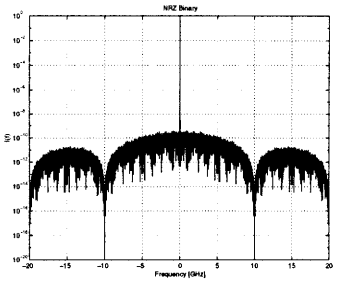

Figure 2-17: Analytical (smooth lines) and simulated spectra (jagged lines) of NRZ binary modulation

In general, the power spectral density for correlated sequences with zero mean is [45, p.101]

$$I(f) = \frac{|P(f)|^2}{T}\left(E\left\{a_0 a_0\right\} + 2\sum_{k=1}^{\infty}\left[E\left\{a_0 a_k\right\}\cos 2\pi k f T\right]\right) \tag{2.22}$$

where $P(f)$ is the Fourier transform of the pulse waveform $p(t)$, the expectation obeys the relation $E\left\{a_0 a_k\right\} = E\left\{a_0 a_{-k}\right\}$ and $E[a_k] = 0$. Note that for a square pulse of duration T and height A, $P(f) = AT\text{sinc}\pi fT$.

If the constant $A/2$ is added to the binary signal, $X(t)$, the offset of the NRZ binary signal is changed so that the signal alternates between 0 and A, the new spectral density is given by

$$I_{\text{NRZ Binary}}(f) = \frac{I_0}{2}(T\text{sinc}^2(\pi fT) + \delta(f)) \tag{2.23}$$

where the pulse amplitude is related to the total average power by $A = \sqrt{2I_0}$. Half of the power is in the carrier frequency (represented the $\delta(f)$ term). Both the analytical and simulated spectra are shown in Figure 2-17. The simulated spectra in this section were generated from a $2^7 - 1$ PRBS with 32 samples per bit for a total of 4096 points.

2.4.2 NRZ AM-PSK Duobinary Format

An AM-PSK duobinary signal is the sum of a binary signal (which alternates between the values $-A/2$ and $A/2$) with a delayed version of itself. If $Y(t)$ represents an AM-PSK duobinary random process, $Y(t) = X(t) + X(t-T)$, where T is one bit period and $Y(t)$ has values 0 or $\pm A$. The autocorrelation of a zero mean AM-PSK duobinary

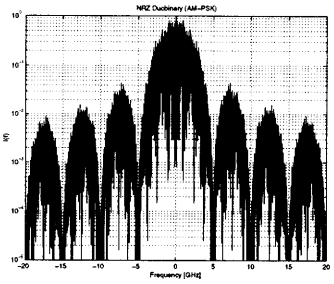

Figure 2-18: NRZ AM-PSK duobinary power spectrum at 10 Gb/s

$a_0 \backslash a_1$	-1	0	1
-1	0	1/8	1/8
0	1/8	1/4	1/8
1	1/8	1/8	0

Table 2.2: The joint probability density function,$P[a_0, a_1]$, for neighboring bits in an alternating phase sequence. These joint probabilities assume that (1) there are an equal number of marks and spaces, (2) the number of "-1"'s equals the number of "1"'s, and (3) cannot have two "-1"'s or two "1"'s follow each other, i.e. 101, 110, and $-10-1$ are prohibited. The expectation value is $E\{a_0 a_1\} = -1/4$.

signal is

$$\begin{aligned} R_{YY}(\tau) &= E\{[X(t)+X(t-T)][X(t-\tau)+X(t-\tau-T)]\} \\ &= 2R_{XX}(\tau)+R_{XX}(\tau+T)+R_{XX}(\tau-T) \end{aligned} \tag{2.24}$$

where R_{XX} is defined by (2.20). The power spectral density is found by integrating (2.24) and is

$$\begin{aligned} I_{\text{NRZ AM-PSK Duobinary}}(f) &= \left(2+e^{j2\pi ft}+e^{-j2\pi ft}\right) I_{\text{NRZ Binary}}(f) \\ &= TI_0(1+\cos 2\pi fT)\text{sinc}^2(\pi fT) \end{aligned} \tag{2.25}$$

The spectrum of the duobinary format is shown in figure 2-18. The magnitude of the pulses is related to the total average power by $A = \sqrt{2I_0}$.

2.4.3 NRZ Alternating Phase Duobinary Format

The alternating phase duobinary electrical signal is created by correlating adjacent

$a_0 \backslash a_2$	-1	0	1
-1	1/16	1/8	1/16
0	1/8	1/4	1/8
1	1/16	1/8	1/16

Table 2.3: The joint probability density function, $P[a_0, a_2]$, for an alternating phase sequence. The expectation value is $E\{a_0 a_2\} = 0$.

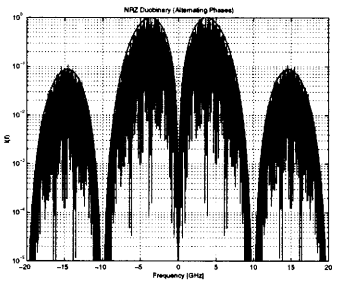

Figure 2-19: Analytical and simulated spectra for NRZ alternating phase duobinary modulation

bits of a binary signal. The result is a signal that has levels at $-A$, 0, and $+A$. The joint probabilities for the alternating phase random process are given in [45, p.225] and also in tables 2.2 and 2.3. The joint probabilities can be substituted into (2.22) to obtain the spectrum of the alternating phase duobinary signal,

$$\begin{aligned} I_{\text{NRZ Alternating Phase Duobinary}}(f) &= \underbrace{AT\text{sinc}^2(\pi f T)}_{|P(f)|^2/T} \underbrace{\frac{1}{2}(1-\cos 2\pi f T)}_{\text{Autocorrelation part}} \\ &= TI_0\text{sinc}^2(\pi f T)(1-\cos 2\pi f T) \end{aligned} \tag{2.26}$$

where the average power of the signal is $I_0 = A^2/2$. Notice that the alternating phase duobinary spectrum is similar to the zero mean binary signal spectrum except that it is multiplied by a cosine term that arises from the autocorrelation. Notice that there is no $\delta(f)$ term in this expression since the time representation of this signal integrates to zero. Both the analytical and simulated spectra for NRZ alternating phase duobinary signals are shown in Figure 2-19.

2.4.4 NRZ Blocked Phase Duobinary Spectrum

The blocked phase duobinary signal is similar to alternating phase duobinary signals since it is generated by correlating adjacent bits of a binary bit stream. To derive the autocorrelation function, the following assumptions about the blocked phase duobinary signal are used:

1. "Marks" with opposite phase can never be neighboring bits. That is, adjacent "marks" must have the same polarity.

2. The block of "marks" has equal chance of being $+A$ as it does $-A$.

3. Only neighboring bits are correlated since the blocked phase duobinary signal is constructed by correlating neigboring bits of a binary random signal.

With these assumptions, the expectation values of the blocked phase duobinary signal are:

$$\begin{aligned} E\{a_0 a_0\} &= \frac{1}{2}A \\ E\{a_0 a_1\} &= \frac{1}{4}A \\ E\{a_0 a_{\geq 2}\} &= 0 \end{aligned}$$

This can be substituted into (2.22) to obtain an expression for the spectrum of the NRZ blocked-phase duobinary signal:

$$\begin{aligned} I_{\text{NRZ Blocked Phase Duobinary}}(f) &= \underbrace{A^2 T \text{sinc}^2(\pi f T)}_{|P(f)|^2/T} \underbrace{\frac{1}{2}(1+\cos 2\pi f T)}_{\text{Autocorrelation part}} \\ &= T I_0 \text{sinc}^2(\pi f T)(1+\cos 2\pi f T) \end{aligned} \tag{2.27}$$

where $I_0 = A^2/2$. Both the analytical and simulated spectra for NRZ alternating phase duobinary signals are shown in Figure 2-20. Notice that the power spectrum is the same as the NRZ AM-PSK duobinary case but this does not mean that the Fourier transforms of the signals are the same. In chapter 4, it will be shown that even

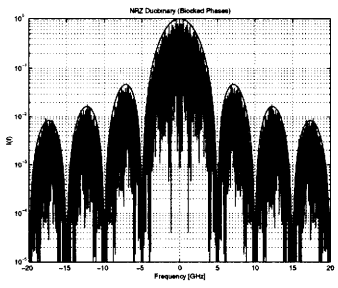

Figure 2-20: Analytical and simulated spectra for NRZ blocked phase duobinary modulation

though the two formats have the same power spectrum, their dispersion penalties are vastly different.

2.4.5 RZ Binary Spectrum

In the previous sections, each NRZ bit was represented by a square pulse. In this section, return-to-zero (RZ) format with gaussian pulses will be considered. Assume that the time domain signal, $p(t)$ can be represented as follows:

$$p(t) = \begin{cases} A\exp\left[-\alpha\left(t-\frac{T}{2}\right)^2\right] & : \quad 0 < t < T \\ 0 & : \quad \text{otherwise} \end{cases} \tag{2.28}$$

where the average power of the signal is related to the pulse amplitude by $I_0 = \frac{1}{2T}\int_0^T |p(t)|^2 dt = \frac{A^2}{2T}\sqrt{\frac{\pi}{2\alpha}}$ assuming that the pulse decays nearly to 0 at $t = 0$ and $t = T$. An RZ binary pulse stream can be written as a summation as in (2.7) with $a_k = 0$ or 1. Note that this signal has a non-zero mean and therefore (2.22) cannot be used to find the autocorrelation function of an RZ binary signal. Note that at the bit edges, the gaussian pulse will have a non-zero amplitude (or a finite extinction ratio) of value $p(t=0) = A\exp\left[-\alpha\frac{T^2}{4}\right]$. To find the autocorrelation function, two regions are considered: $|\tau| < T$ and $|\tau| > T$. For $|\tau| < T$, assuming ergodicity and using an equation similar to the NRZ binary case (2.10), the autocorrelation function is:

$$\begin{aligned} &R_{xx}(\tau \mid 0 < \tau < T) \\ &= \sum_{i=1}^{4} \frac{1}{T}\left[\int_0^{\tau} a_0(C_i)a_{-1}(C_i)p(t)p(t-\tau+T)dt\right. \end{aligned}$$

Event	$a_{-1}(C_i)$	$a_0(C_i)$	$P(C_i)$
C_1	1	1	1/4
C_2	1	0	1/4
C_3	0	1	1/4
C_4	0	0	1/4

Table 2.4: Events corrsponding to the value of the first and second bit in the random binary process X(t).

a_0	a_n	a_{n+1}	$P(a_0, a_n, a_{n+1})$
0	1	1	1/8
0	1	0	1/8
0	0	1	1/8
0	0	0	1/8
1	1	1	1/8
1	1	0	1/8
1	0	1	1/8
1	0	0	1/8

Table 2.5: Probabilities for the bits of an RZ binary signal for $\tau > T$.

$$+ \int_{\tau}^{T} a_0(C_i)a_0(C_i)p(t)p(t-\tau)\Big] P(C_i) \tag{2.29}$$

$$= \frac{A^2}{4T}\sqrt{\frac{\pi}{2\alpha}}\left(2\text{erf}\left(\sqrt{\frac{\alpha}{2}}(T-\tau)\right)e^{-\frac{\alpha}{2}\tau^2} + \text{erf}\left(\sqrt{\frac{\alpha}{2}}\tau\right)e^{-\frac{\alpha}{2}(T-\tau)^2}\right) \tag{2.30}$$

where the events C_i are tabulated in table 2.4.

The autocorrelation of the RZ signal can be found for $\tau > T$ by using (2.18) except that the expectation values for the a_i's are tabulated in table 2.5. The resulting autocorrelation for the RZ gaussian binary signal is

$$R_{XX}(\tau) = \begin{cases} \frac{I_0}{2}\left(2\text{erf}\left(\sqrt{\frac{\alpha}{2}}(T-\tau)\right)e^{-\frac{\alpha}{2}\tau^2} + \text{erf}\left(\sqrt{\frac{\alpha}{2}}\tau\right)e^{-\frac{\alpha}{2}(T-\tau)^2}\right) & : \quad |\tau| < T \\ \frac{I_0}{2}\left(\text{erf}\left(\sqrt{\frac{\alpha}{2}}(T-\tilde{\tau})\right)e^{-\frac{\alpha}{2}\tilde{\tau}^2} + \text{erf}\left(\sqrt{\frac{\alpha}{2}}\tilde{\tau}\right)e^{-\frac{\alpha}{2}(T-\tilde{\tau})^2}\right) & : \quad |\tau| \geq T \end{cases} \tag{2.31}$$

where I_0 is the average power and $\tilde{\tau} = \text{mod}(\tau, T)$ is the remainder of τ/T. This function is plotted in figure 2-21. Equation (2.31) can be simplified for narrow gaussian pulses in which the standard deviation of the pulse is approximately less than

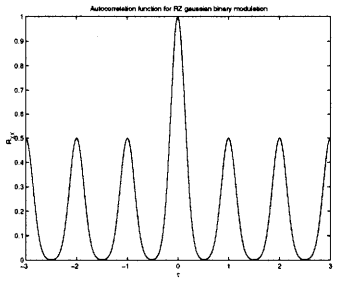

Figure 2-21: The autocorrelation function for RZ gaussian binary modulation. In this plot, $T = 1$, $\alpha = 50$, and $I_0 = 1$.

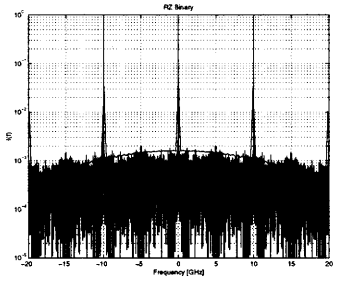

Figure 2-22: Analytical and simulated spectra for RZ binary modulation

one-fifth the time of the bit slot. In this special case, the erf terms are approximately equal to 1 and (2.31) can be written as

$$R_{XX}(\tau) = \begin{cases} \frac{I_0}{2}\left(2e^{-\frac{\alpha}{2}\tau^2} + e^{-\frac{\alpha}{2}(T-\tau)^2}\right) & : \quad |\tau| < T \\ \frac{I_0}{2}\left(e^{-\frac{\alpha}{2}\tilde{\tau}^2} + e^{-\frac{\alpha}{2}(T-\tilde{\tau}^2)}\right) & : \quad |\tau| \geq T \end{cases} \tag{2.32}$$

The power density spectrum of RZ gaussian binary modulated signals can be found by taking the Fourier transform of (2.31). Since it is not easy to take the Fourier transform of a piecewise function that contains error functions, we take the Fourier transform of (2.32) and realize that this is only accurate for narrow pulses (αT^2 large),

$$I_{\text{RZ Binary}}(f) = I_0\sqrt{\frac{\pi}{2\alpha}}\left(1 + \frac{1}{T}\sum_k \delta(f - \frac{k}{T})\right)\exp[-2\pi^2 f^2/\alpha] \tag{2.33}$$

The power density spectrum of the RZ binary spectrum is plotted in figure 2-22. Half the power of the signal is in the exponential envelope and the other half is distributed amongst the spikes or delta functions of the power spectrum.

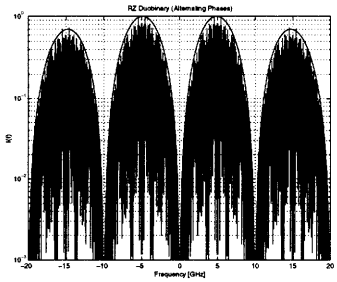

Figure 2-23: Analytical and simulated spectra for RZ alternating phase duobinary modulation

2.4.6 RZ Alternating Phase Duobinary Format

The RZ alternating phase duobinary spectrum and the RZ blocked phase duobinary spectrum have zero means. This implies that it is possible to use (2.22) to find these spectra. Therefore it will be handy to find the Fourier transform of (2.28):

$$\begin{aligned} P(f) &= \int_{-\infty}^{\infty} A \exp\left[-\alpha\left(t-\frac{T}{2}\right)^2\right] e^{-j2\pi ft} dt \\ &= A\sqrt{\frac{\pi}{\alpha}} e^{-\frac{\pi^2 f^2}{\alpha} - j\pi fT} \end{aligned} \tag{2.34}$$

where again it is assumed that the gaussian pulse decays to approximately zero before the next bit slot.

The RZ alternating phase duobinary spectrum has the same correlation between adjacent bits as does the NRZ alternating phase duobinary signal. Therefore, we can use the autocorrelation part of (2.26) and (2.34) in (2.22) to obtain the power spectral density

$$\begin{aligned} I_{\text{RZ Alternating Phase Duobinary}}(f) &= \frac{(A^2)\frac{\pi}{\alpha} e^{-\frac{2\pi^2 f^2}{\alpha}}}{T} \frac{1}{2}(1-\cos 2\pi fT) \\ &= I_0 \sqrt{\frac{2\pi}{\alpha}} e^{-\frac{2\pi^2 f^2}{\alpha}} (1-\cos 2\pi fT) \end{aligned} \tag{2.35}$$

where this expression is more accurate for narrower pulses (αT^2 large). Both the analytical and simulated spectra for RZ alternation phase duobinary signals are shown in Figure 2-23.

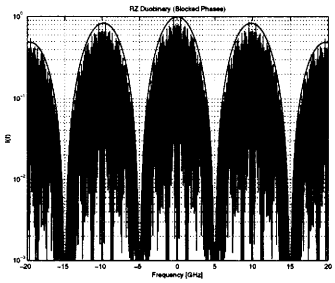

Figure 2-24: Analytical and simulated spectra for RZ blocked phase duobinary modulation

2.4.7 RZ Blocked Phase Duobinary Format

The blocked phase duobinary spectrum has the same correlation between adjacent bits as does the NRZ blocked phase duobinary signal. Therefore, the autocorrelation part of (2.27) and (2.34) can be substituted into (2.22) to obtain

$$\begin{aligned} I_{\text{RZ Blocked Phase Duobinary}}(f) &= \frac{(A^2)\frac{\pi}{\alpha}e^{-\frac{2\pi^2 f^2}{\alpha}}}{T}\frac{1}{2}(1+\cos 2\pi fT) \\ &= I_0\sqrt{\frac{2\pi}{\alpha}}e^{-\frac{2\pi^2 f^2}{\alpha}}(1+\cos 2\pi fT) \end{aligned} \tag{2.36}$$

where this equation is more accurate for narrower pulses. Both the analytical and simulated spectra for RZ blocked phase duobinary signals are shown in Figure 2-24.

Chapter 3

Computational Model for Optical Fiber Transmission

The simulation of binary or duobinary signals in an optical fiber involves modeling of the generation, propagation and reception of the transmitted signal. The trade off of any simulation is between accuracy and time. This chapter will discuss a model for the noise and propagation for a single span transmission system. Chaotic effects which are computationally time consuming such as stimulated Brillouin and Raman scattering are not considered in the model. Rather, an analytic expression for the threshold power for which these stimulated scattering processes become dominant is considered in chapter 6. The first section of this chapter will give a brief overview of the computational model used and the second section will focus on the derivation of noise terms for an optically pre-amplified receiver.

3.1 The Simulator

The workings of the simulator used to predict the sensitivities of various modulation formats and used extensively in chapter 4 is explained in this chapter.

Figure 3-1 shows an overview of the simulator from the signal generation to the signal reception. The simulator in [52] normalized their electrical signals in the receiver so that the maximum ripple value equaled V_π of the MZ modulator, that is,

they do not overdrive the modulator, but rather the underdrive it. Better sensitivities are obtained when the average value of the ones of the electrical signal correspond to V_π since this maximizes the transmitted eye opening. The following channel or fiber span can either be modeled with or without nonlinearities. Simulating nonlinearities takes longer and therefore is used only when the launch powers are high enough for nonlinearities to make a difference. When simulating a linear channel, one must check to make sure that the nonlinear length is much less than the dispersion length, i.e. $L_{NL} = 1/\gamma P \ll L_D = T_0^2/|\beta_2|$, where γ is the nonlinearity coefficient [2], and β_2 is dispersion. To speed up nonlinear simulations, a multiresolution method outlined in appendix D was used.

The nomenclature associated with filtering can be somewhat confusing and must be clarified before simulating any optical system. When the bandwidth of an optical low-pass filter is specified, say 10 GHz, the number corresponds to the full width at half-maximum bandwidth or double-sided bandwidth that spans between the two 3-dB power cutoff frequencies. For an electrical filter, the bandwidth refers to the single-sided bandwidth. In addition, the 3-dB cutoff of an electric or optical filter refers to the power or $|H(j\omega)|^2$ and not the magnitude of the signal.

Figure 3-2 shows how the sensitivity was calculated for a receiver with a linear channel. This figure shows the details to the highlighted box in figure 3-1. The initial guess for the receiver sensitivity at L km, or the necessary received optical power to achieve a 10^{-9} BER, is found using a formula for the back-to-back sensitivity derived by Rühl [44] minus the loss of L km of fiber,

$$P_{AV} = \frac{1}{2GL_OL_I(\frac{1-r}{1+r})} \cdot \left\{ 36C\frac{1+r}{1-r} \pm 12 \cdot \sqrt{36C^2\frac{r}{(1-r)^2} + I_{circ} + N_{00}} \right\} \cdot e^{-\alpha L}. \quad (3.1)$$

where G is the gain of the optical preamplifier, L_I and L_O are the entrance and exit loss of the optical preamplifier, r is the extinction ratio, C is the signal-dependent noise divided by the signal power, I_{circ} is the circuit noise of the receiver, and N_{00} is the signal independent noise arising from the detected amplified spontaneous emission. Successive guesses for the sensitivity are tried until the sensitivity yields a BER

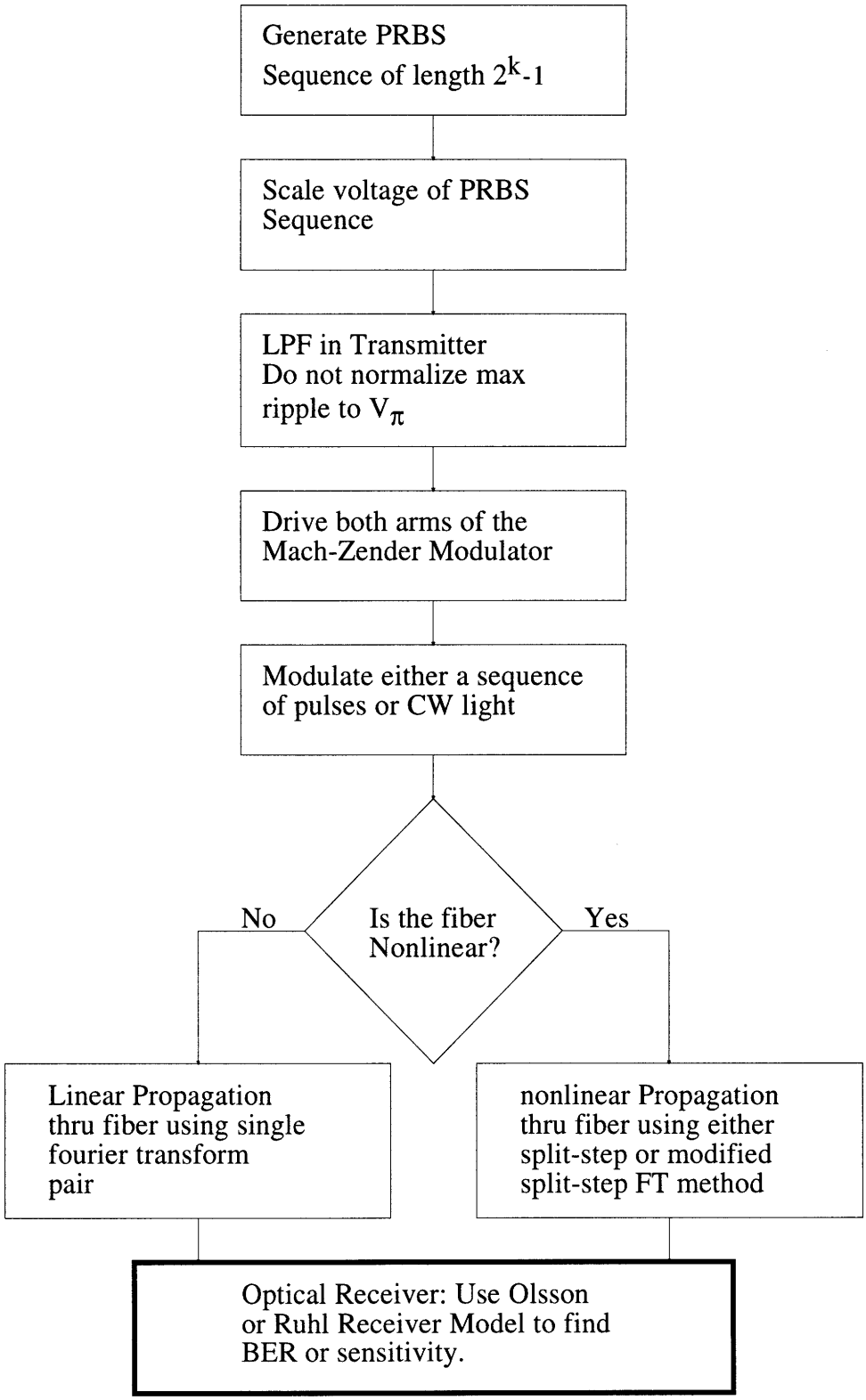

Figure 3-1: A flow diagram showing an overview of the simulator.

within one percent of 10^{-9}. Successive guesses for the sensitivity use the fact that the received power in watts is approximately linearly related to Q. The quality of the received signal is defined as [1, p.165]

$$Q = \frac{\mu_{mark} - \mu_{space}}{\sigma_{mark} + \sigma_{space}} \tag{3.2}$$

where μ denotes the mean and σ denotes the standard deviation. Q is related to the BER by

$$BER = \frac{1}{2}\text{erfc}\left(\frac{Q}{\sqrt{2}}\right) \tag{3.3}$$

which can be approximated by

$$\log_{10} Q = \log_{10}\left(1.438\sqrt{-\ln(BER) - 1.055 - 0.376}\right). \tag{3.4}$$

Note that $Q = 6$ corresponds to a BER of 10^{-9}. Successive guesses to the sensitivity can be obtained by making linear interpolations using the last two values for the receiver power (Watts) versus Q.

Figure 3-3 shows how the BER is calculated. This figure shows the details to the highlighted box in figure 3-2. The BER is calculated by finding the decision point (phase and voltage level) where the BER is minimized. This can be done by either finding the minimum BER from an array of points in the eye (as shown in figure 3-3) or by finding the point where the error of the marks equals the error of the spaces (which is computationally faster).

3.2 Derivation of Noise Terms for an Optically Preamplified Receiver

This section contains the derivation of the noise variances for an optically preamplifed receiver which are used to calculate the BER of a received signal (this is the third step in the flow graph in figure 3-3). This derivation follows Cartledge's formulation [4] and the underlying mathematical background for the noise statistics can be found

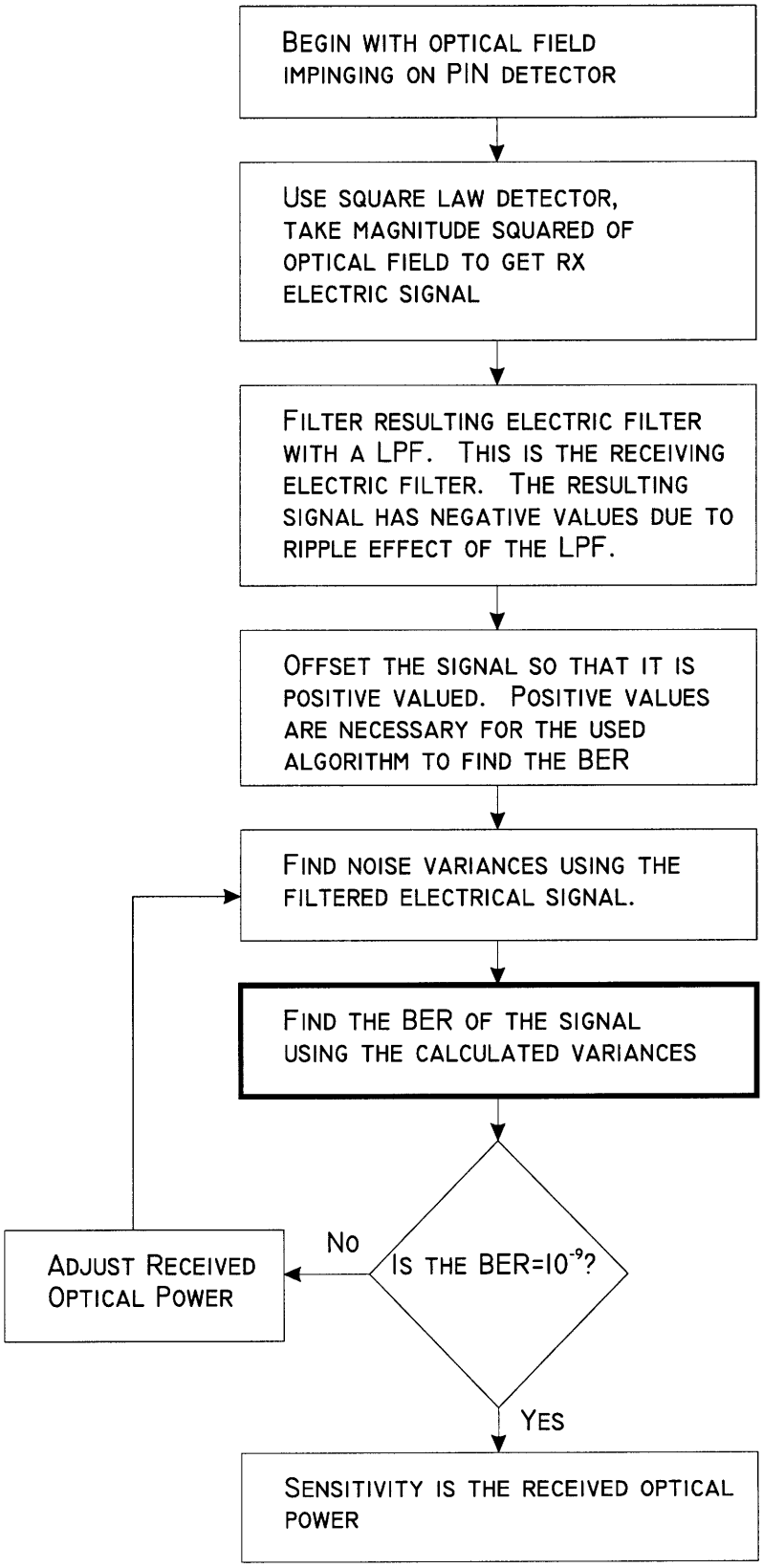

Figure 3-2: A flow diagram showing how the sensitivity is calculated from the receiver model.

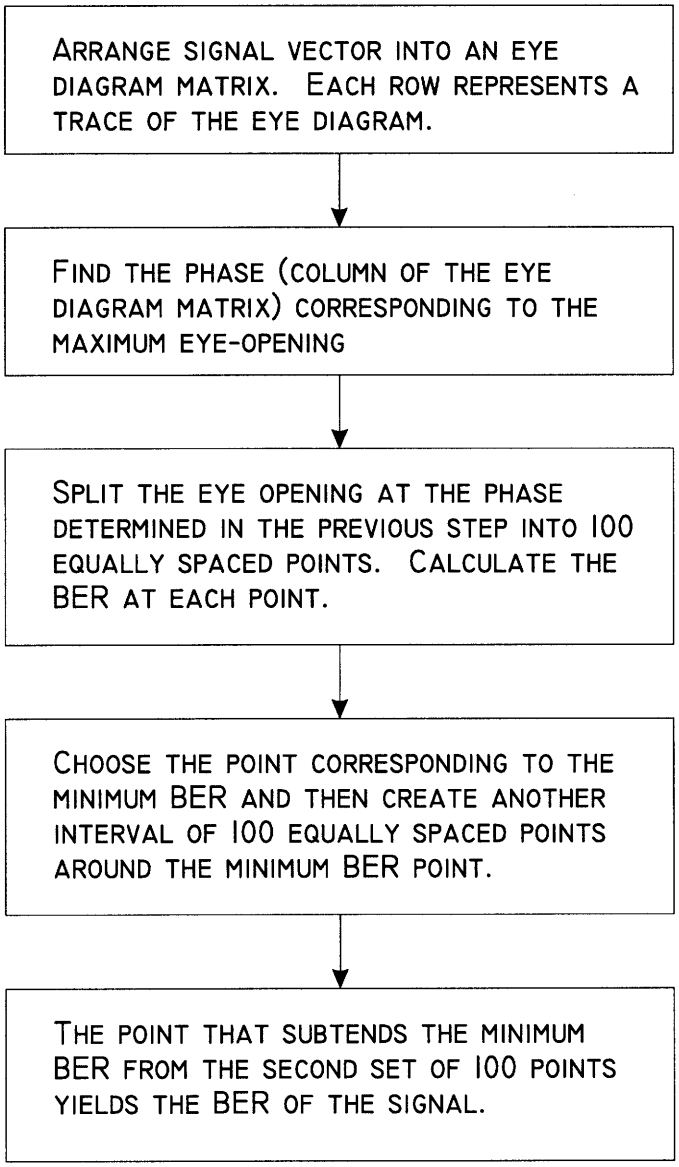

Figure 3-3: A flow diagram showing how the BER is calculated.

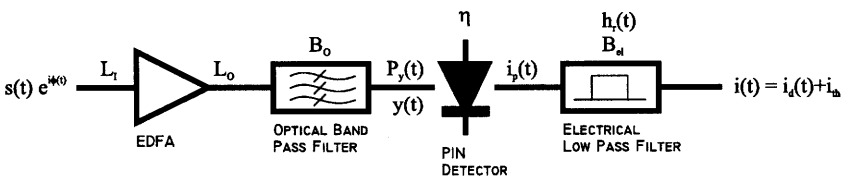

Figure 3-4: The model for the optically preamplified receiver.

in [35]. The last part of this chapter explains some of the failings of this model.

3.2.1 Derivation of the Noise Terms

The goal of this section is to derive the noise variances for an optically preamplified receiver. The model for the receiver is shown in figure 3-4. The receiver consists of an EDFA optical preamplifier, a PIN photodiode and receiver electronics (modeled as a LPF with an effective bandwidth, B_{el}). The decision of whether a received bit is a zero or a one is decided from the value of $i(t)$.

The optical signal incident to the EDFA can be written as $s(t)e^{j\phi_s(t)}$, where $s(t)$ is the magnitude of the optical signal and $\phi_s(t)$ is its phase. The EDFA has facet losses from imperfect coupling of L_I at the input and L_O at the output. The EDFA noise power can be modeled as additive white noise with a power spectral density of $(G-1)n_{sp}h\nu$ per polarization where G is the EDFA gain [7], and n_{sp} is the spontaneous-emission or population-inversion factor equal to $N_2/(N_2-N_1)$ where N_1 and N_2 are the atomic populations for the ground and excited states, respectively. The optical signal plus amplifier white noise leaves the amplifier and experiences a loss, L_O due isolators and couplers which are part of the EDFA. The optical signal then travels through an optical filter with bandwidth B_o that reduces the bandwidth of the white noise but allows the signal to pass unattenuated. The optical signal before hitting the PIN photodiode can be written as

$$y(t) = \underbrace{\sqrt{L_I G L_O}\, s(t) \exp(j\phi_s(t))}_{\text{signal}} + \underbrace{\sqrt{L_O}\, n(t)}_{noise} \tag{3.5}$$

where $n(t)$ is the additive white noise from the EDFA. The noise term, $n(t)$ can be

separated into its quadrature components: $n(t) = n_c(t) + jn_s(t)$. The mean and the variances are

$$E[n_c(t)] = E[n_s(t)] = 0 \tag{3.6}$$

and

$$E[n_c^2(t)] = E[n_s^2(t)] = (G-1)h\nu n_{sp}B_o \tag{3.7}$$

which means that

$$E[n^2(t)] = E[n_c(t)^2 + n_s(t)^2 + 2jn_c(t)n_s(t)] = E[n_c(t)^2] + E[n_s(t)^2] = 2(G-1)h\nu n_{sp}B_o. \tag{3.8}$$

Since the quadrature components are independent, their cross correlation is zero since $E[n_c(t)n_s(t)] = E[n_c(t)]E[n_s(t)] = 0$.

The optical power hitting the PIN photodiode in figure 3-4 is

$$\begin{aligned} P_y(t) = y^*(t)y(t) \quad = \quad & \underbrace{L_I G L_O s^2(t)}_{\text{signal}} \\ & + \underbrace{L_O\left(n_c^2(t) + n_s^2(t)\right)}_{\text{spontaneous-spontaneous beat noise}} \\ & + \underbrace{2L_O\sqrt{GL_I}s(t)\left\{n_c(t)\cos\phi_s(t) + n_s(t)\sin\phi_s(t)\right\}}_{\text{signal-spontaneous beat noise}} \end{aligned} \tag{3.9}$$

At high optical preamplifier gain, G, signal-spontaneous beat noise dominates over spontaneous-spontaneous beat noise. The opposite is also true. Spontaneous-spontaneous beat noise dominates over signal-spontaneous beat noise at low optical preamplifier gains.

The optical power, $P_y(t)$, is converted into an electric current by the PIN photodiode and can be expressed as

$$i_p(t) = \frac{\eta q}{h\nu}P_y(t) + i_{\text{dark}} \tag{3.10}$$

where η is the quantum efficiency, q is the electronic charge, and i_{dark} is the dark

current. The current from the PIN photodiode is then filtered before it is presented to the decision circuitry. The current seen by the decision circuitry is

$$\begin{aligned} i(t) &= h_r(t) * i_p(t) + i_{th} \\ &= \left(\frac{\eta q}{h\nu} P(t) + i'_{\text{dark}}\right) + i_{th} \end{aligned} \tag{3.11}$$

where $h_r(t)$ is the impulse response of the receiver electronics, $P(t) = P_y(t) * h_r(t)$ is the filtered signal plus beat noises, $i'_{\text{dark}} = i_{\text{dark}} * h_r(t)$ is the filtered dark current, and i_{th} is the current due to thermal noise. The component of the current in (3.11) from the PIN photodiode is the detected current, $i_d(t)$, which is defined as

$$i_d(t) = \frac{\eta q}{h\nu} P(t) + i'_{\text{dark}} \tag{3.12}$$

If the arrival time of photons incident upon the PIN photodiode can be modeled as a Poisson process, then the detected current can be represented as a sum of impulse responses to randomly arriving electrons.

$$i_d(t) = q \sum_{n=1}^{\infty} h_r(t - t_n) \tag{3.13}$$

where $h_r(t)$ is the impulse response of the receiver electronics and t_n is Poisson distributed. The probability that there are k incident photons in time T is given by

$$P[n = k] = e^{-\lambda(t)T} \frac{(\lambda(t)T)^k}{k!} \qquad k = 0, 1, \ldots \tag{3.14}$$

where $\lambda(t) = \frac{i_p(t)}{q}$ is the electron arrival rate. The electron arrival rate can be re-expressed by substituting (3.10) for $i_p(t)$ to yield

$$\lambda(t) = \frac{\eta}{h\nu} P_y(t) + \lambda_0 \tag{3.15}$$

where η is the quantum efficiency of the PIN diode and λ_0 is the dark current count in electrons per second.

The second characteristic function, $\Psi_{i_d(t)}(\omega)$, of $i_d(t)$ is used to find its mean and variance. The variance is given by $-\frac{\partial^2\Psi}{\partial\omega^2}|_{\omega=0}$ and the mean is given by $-j\frac{\partial\Psi(\omega)}{\partial\omega}|_{\omega=0}$ [35, p.158]. The first characteristic function for the Poisson process in (3.13) is [35, p.566]

$$\Phi_{i_d(\tau)}(\omega) = E[e^{j\omega i_d(\tau)}] = \exp\left[\int \lambda(t)(e^{jqh_r(\tau-t)\omega} - 1)dt\right] \tag{3.16}$$

Substituting (3.15) into (3.16), we obtain

$$\begin{aligned}
\Phi_{i_d(\tau)}(\omega) &= \exp\left[\int \left(\frac{\eta G}{h\nu} L_I L_O s^2(t) + \lambda_0\right) \cdot (\exp(\omega q h_r(\tau - t)) - 1)\, dt\right] \\
&\times \exp\left[\int \frac{\eta L_O}{h\nu}\left(n_c^2(t) + 2\sqrt{GL_I}\, n_c(t) s(t) \cos\phi_s(t)\right)\right. \\
&\qquad \left. \cdot (\exp(\omega q h_r(\tau - t)) - 1)\, dt\right] \\
&\times \exp\left[\int \frac{\eta L_O}{h\nu}\left(n_s^2(t) + 2\sqrt{GL_I}\, n_s(t) s(t) \sin\phi_s(t)\right)\right. \\
&\qquad \left. \cdot (\exp(\omega q h_r(\tau - t)) - 1)\, dt\right].
\end{aligned} \tag{3.17}$$

The next step is to assume that the ASE noise, $n_c(t)$ and $n_s(t)$, is constant over time intervals of duration $T_s = 1/B_o$ and independently random from interval to interval. This assumption is good for narrow B_o since the ASE noise is not constant over a large bandwidth. If each pulse period of duration T is divided into M subintervals of duration T_s, then the ASE noise can be written as a Riemann sum

$$n_c(t) = \sum_{k=-\infty}^{\infty} \sum_{l=0}^{M-1} n_c(k,l) p(t - kT - lT/M) \tag{3.18}$$

where $p(t) = U(t) - U(t - T/M)$, $U(t)$ is the unit step function, and $n_c(k,l)$ are samples of the continuous $n_c(t)$. The quadrature component of ASE noise, $n_s(t)$, can also be expressed similarly to (3.18).

The second characteristic function of (3.13), defined by $\Psi_{i_d(t)}(\omega) = \ln\Phi_{i_d(t)}(\omega) = \ln E[e^{j\omega i_d(t)}]$ can be evaluated by using (3.18) in (3.17). The result is

$$\begin{aligned}
\Psi_{i_d(\tau)}(\omega) &= \int \left(\frac{\eta G}{h\nu} L_I L_O s^2(t) + \lambda_0\right)(\exp(\omega q h_r(\tau - t)) - 1)\, dt \\
&\quad - \sum_k \sum_l \left(1 - 2P_n \frac{\eta L_O}{h\nu} \alpha(\omega, k, l)\right)
\end{aligned}$$

$$+\sum_k \sum_l \frac{P_n \frac{\eta\sqrt{GL_I}L_O}{h\nu}(\beta_c^2(\omega,k,l)+\beta_s^2(\omega,k,l))}{1-2P_n\frac{\eta L_O}{h\nu}\alpha(\omega,k,l)} \tag{3.19}$$

where the ASE noise power from the optical preamplifier incident upon the PIN photodiode is

$$P_n = (G-1)h\nu n_{sp}B_o = E[n_c(t)] = E[n_s(t)], \tag{3.20}$$

and where

$$\alpha(\omega,k,l) = \int_{(k+l/M)T}^{(k+(l+1/M))T} [\exp(\omega q h_r(\tau-t))-1]\,dt \tag{3.21}$$

$$\beta_c(\omega,k,l) = \int_{(k+l/M)T}^{(k+(l+1/M))T} s(t)\cos\phi_s(t)\,[\exp(\omega q h_r(\tau-t))-1]\,dt \tag{3.22}$$

$$\beta_s(\omega,k,l) = \int_{(k+l/M)T}^{(k+(l+1/M))T} s(t)\sin\phi_s(t)\,[\exp(\omega q h_r(\tau-t))-1]\,dt \tag{3.23}$$

Finally, the variance and mean can be computed from the second characteristic function of $i_d(\tau)$ by taking its derivatives and letting $\omega = 0$. The mean of $i_d(\tau)$ is

$$\mu_{i_d(\tau)} = \underbrace{\frac{\eta q G L_I L_O}{h\nu} s^2(\tau) * h_r(\tau)}_{\text{signal component}} + \left(\underbrace{\frac{2\eta P_n L_O}{h\nu}}_{\substack{\text{spontaneous}\\ \text{emission}\\ \text{component}}} + \underbrace{\lambda_0}_{\substack{\text{dark}\\ \text{current}\\ \text{component}}} \right) q \int h_r(t)dt \tag{3.24}$$

where $*$ denotes a convolution, and the variance is

$$\sigma^2_{i_d(\tau)} = \underbrace{\frac{\eta q^2 G L_I L_O}{h\nu}\left[s^2(\tau) * h^2(\tau)\right]}_{\text{Shot Noise}}$$

$$
\begin{aligned}
&+ \quad \underbrace{\lambda_0 q^2 \int h_r^2 dt}_{\text{Dark Current Noise}} \\
&+2P_n \sum_k \sum_l \underbrace{\left[\frac{\eta q^2 L_O}{h\nu} \int_{(k+l/M)T}^{(k+(l+1/M))T} h_r^2(\tau - t)dt \right.}_{\text{Spontaneous emission shot noise}} \\
&\qquad \underbrace{\left. + 2P_n \left(\frac{\eta q L_O}{h\nu} \int_{(k+l/M)T}^{(k+(l+1/M))T} h_r(\tau - t)dt \right)^2 \right]}_{\text{Spontaneous-Spontaneous Beat Noise}} \\
&+P_n \sum_k \sum_l \underbrace{\left[\left(\frac{2\eta q \sqrt{G L_I} L_O}{h\nu} \int_{(k+l/M)T}^{(k+(l+1/M))T} s(t) \cos\phi_s(t) h_r(\tau - t)dt \right)^2 \right.}_{\text{Signal-Spontaneous Beat Noise}} \\
&\qquad \left. + \left(\frac{2\eta q \sqrt{G L_I} L_O}{h\nu} \int_{(k+l/M)T}^{(k+(l+1/M))T} s(t) \sin\phi_s(t) h_r(\tau - t)dt \right)^2 \right]
\end{aligned}
\tag{3.25}
$$

The noise variance, given by (3.25), can be simplified with several assumptions. Assuming that the dark current is negligible (i.e. λ_0 is small), we can ignore the contribution due to the dark current. If it is assumed that the receiver filter has a perfect rectangular shape, and that the receiver filter transfer function is normalized such that $\int_{-\infty}^{\infty} h_r(t)dt = 1$ (hence $\int_{-\infty}^{\infty} h_r^2(t)dt = 2B_{el}$), noting that the sum of integrals involves a multiplicative factor of $dt = 1/B_o$, the number of polarization states detected equals 2 ($p = 2$), and both $s(t)$ and $\phi_s(t)$ are constant over the period T/M, then (3.25) can be simplified to:

$$N_{sh,s} = 2B_{el} \frac{\eta q^2 G L_I L_O}{h\nu} s^2(t) \tag{3.26}$$

$$N_{sh,sp} = 2pB_{el} P_n \frac{\eta q^2 L_O}{h\nu} \tag{3.27}$$

$$N_{sp-sp} = 2pP_n^2 \left(\frac{\eta q L_O}{h\nu} \right)^2 \tag{3.28}$$

$$N_{s-sp} = 4P_n \left(\frac{\eta q}{h\nu} \right)^2 G L_I L_O^2 s^2(t) \tag{3.29}$$

which are the noise terms used in the simulations presented in this paper and are

equivalent to the noise expressions given in [45].

3.2.2 Failings of the Model

There are several assumptions in the derivation of (3.26)-(3.29) which oversimplify the problem and may lead to inaccurate results. First, the noise spectrum from the EDFA is assumed flat, whereas it is known that the noise from an EDFA consists of two humps over a span of about 3 THz. Over narrow optical filter bandwidths ($B_o < 1$ nm) the noise spectrum is approximately flat, but over wider optical filter bandwidths ($B_o > 10$ nm), the noise spectrum is not flat, but has significant curvature. The value for B_o in simulations with large optical filter bandwidths is more of a fitting parameter rather than the actual 3-dB bandwidth of the optical filter used in the receiver.

The second problem with the model for the noise terms is the assumption that the noise probability density functions are gaussian for both the marks and the spaces. Even though these assumptions give reasonable sensitivity estimates, in a strict sense, the noise of the spaces is closer to a Bose-Einstein distribution convolved with a gaussian. Even though the Bose-Einstein noise statistics of a receiver has been theoretically derived before [15], for the first time, experimental data has been taken to confirm the theory[20]. Figure 3-5 shows experimental data for the probability density function of the spaces fitted to a gaussian and figure 3-6 shows the same data fitted to a Bose-Einstein distribution convolved with a gaussian. The Bose-Einstein curve lies closer to the experimental data.

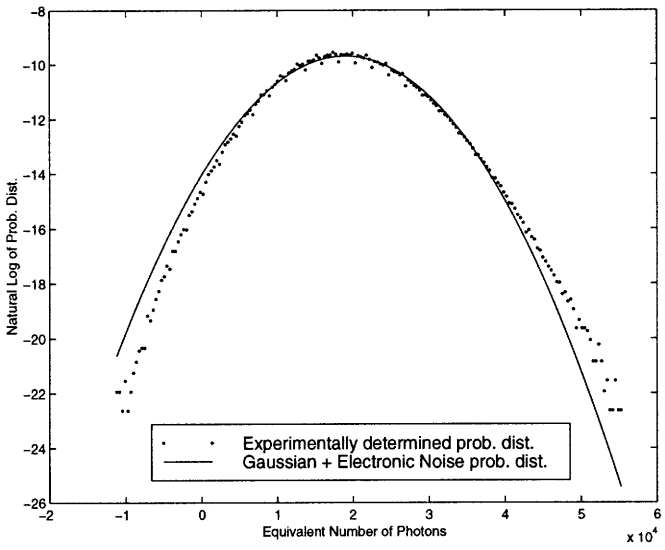

Figure 3-5: The probability density function for the spaces with gaussian fit. Dots indicate experimental data and solid line indicates the fit.

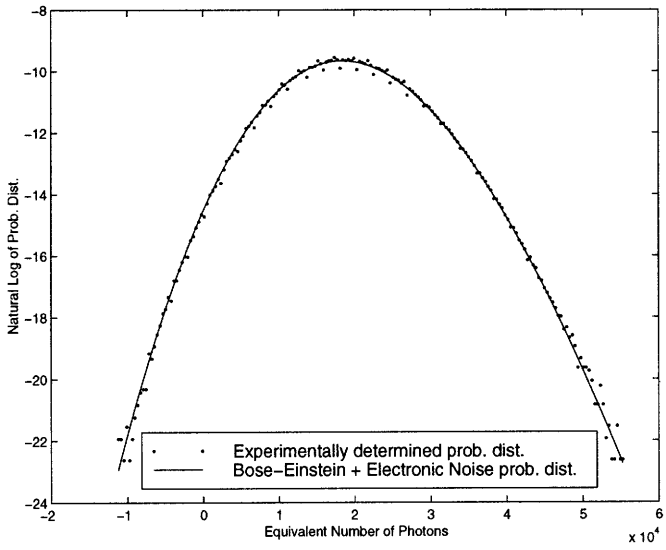

Figure 3-6: The probability density function for the spaces with Bose-Einstein convolved with a gaussian fit. Dots indicate experimental data and solid line indicates the fit.

Chapter 4

Optimal Filtering

Given a repeaterless duobinary transmission system, as shown in figure 4-1, it is important to determine how to choose optimal transmitting and receiving filters. Up until the present thesis, there has been very little reported work on how to choose optimal filters in an optical duobinary transmission system. There have been several observations that filtering at approximately half the bit rate of an AM-PSK duobinary signal leads to improved propagation distances.[52] This result is somewhat intuitive since the AM-PSK duobinary signal has its first null in its spectrum at half its bit rate. On the other hand, it is not intuitively clear how fast the electrical filters should roll-off, whether ripples in the filters amplitude or phase response cause serious degradations, or how the optimal filtering varies with the channel response.

The optimization criterion that will be used in this chapter is minimizing the bit-error rate (BER). This optimization criterion is preferable to the common method of optimizing the filters for the lowest signal-to-noise ratio (SNR) since the lowest SNR may not necessarily correspond to the lowest BER.

Chapter 3 developed the model for an optically pre-amplified direct-detection receiver. The main reason why it is not possible to simply write expressions for the optimal filters analytically is due to several nonlinearites in the transmission system. First, the Mach-Zender external modulator (MZM) has a sinusoidal relation between the driving electrodes and the optical output intensity. To achieve maximal eye-opening of the transmitted signal, external modulators are always driven in a range

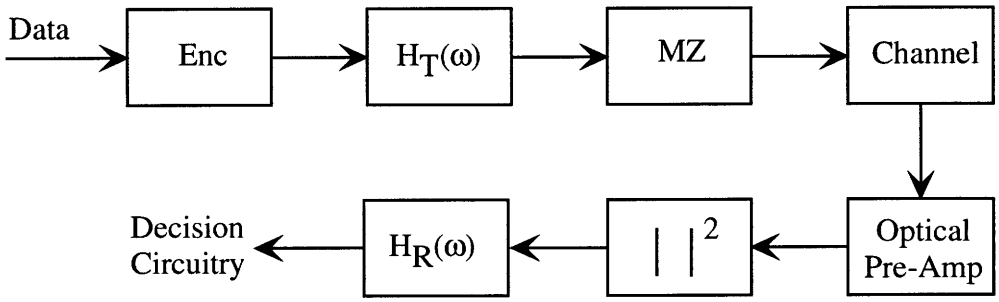

Figure 4-1: Simplified optical transmission system that will be discussed in this chapter. The duobinary encoder (labeled **Enc** in the diagram) can be an AM-PSK, alternating phase, or blocked phase duobinary encoder, for example. The electrical transmitting and receiving filters are $H_T(\omega)$ and $H_T(\omega)$, respectively. The **MZ** box is an external Mach-Zender modulator. The optical channel or fiber is connected to an optically preamplified receiver and subsequently to a square-law detector (*pin* diode) and finally to the receiving filter.

that cannot be approximated well with a linear function. The second difficulty with finding an analytical expression for the optimal filter is that noise is added by the optical pre-amplifier before a square-law detector. The detected current then contains signal-noise beat terms, thereby making the noise signal-dependent. Finally, another complication arises due to the fact that the signal is sampled at specified intervals, and only these samples determine the BER.

Since there is no simple analytical expression for the optimal filter, a computer is used to gain some insight. Butterworth, Bessel, and Chebyshev filters of various orders (2-12) and maximum ripple (0.1, 0.5, and 1 dB) were examined. These filters represent a wide range of properties. The Butterworth filter is known for its maximally flat amplitude response and the Bessel filter is known for its maximally flat phase response. The Chebyshev filter was examined to see the effects of ripple in the passband. For reference, the amplitude responses and group delays of these filters are plotted in appendix A.

A brief summary of the results of this chapter are

- The most sensitive filter parameters affecting the BER are the filter bandwidth and roll-off steepness. The ripple across the passband (with 1 dB maximum power variation) in either phase or amplitude plays a smaller role in determining the BER.

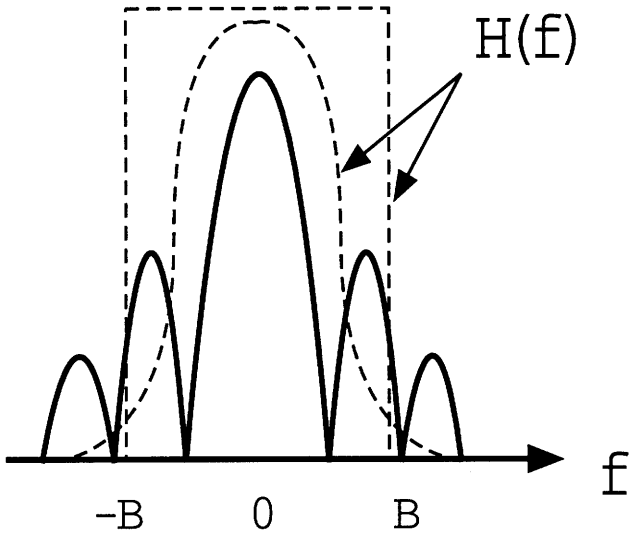

Figure 4-2: The power density spectrum of an AM-PSK duobinary signal. The dashed lines represent filtering at two different bandwidths and two different roll-offs. Intuitively, it is hard to see which filter will result in a lower BER.

- The best filtering for AM-PSK and blocked-phase duobinary format is obtained for low-order, slow-roll-off filters. The best bandwidths are approximately $0.6B$, where B is the bitrate.
- The optimal bandwidth increases for higher-order, steeper-roll-off filters.
- Since the alternating-phase duobinary signal has a broader spectrum, broader filters (with bandwidths of $1.1B$ after 80 km of propagation through SCF, for example) lead to better bit error rates.

4.1 Filtering of AM-PSK Duobinary Signals

The "width" of the AM-PSK duobinary signal spectrum refers to the first amplitude null which occurs at half the bit rate of the signal, $0.5B$ (see figure 4-2). Intuitively, the optimal filtering bandwidth should be about $0.5B$ since it contains most of the signal energy (77%). In fact, the optimal bandwidth can be between $0.6B$ and $1.1B$ depending on the filter type, order (roll-off steepness), and total channel dispersion.

The steepness of the filter roll-off (directly related to the filter order) is a very important filter parameter in determining the optimal filtering bandwidth. For AM-

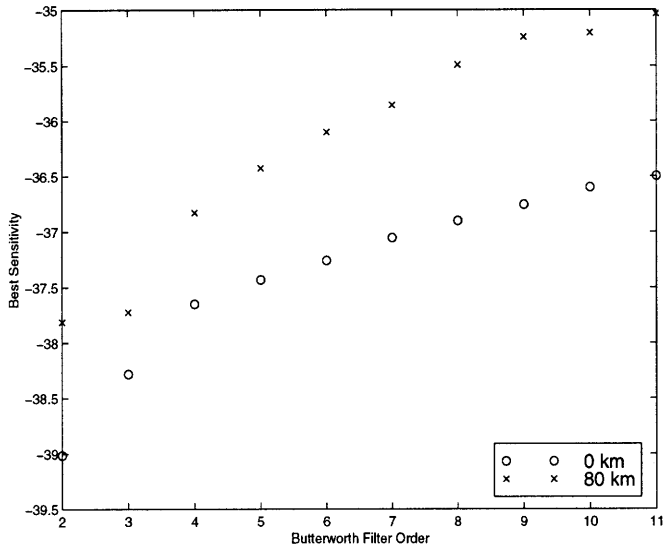

Figure 4-3: The receiver sensitivity is plotted against the electrical filter order. The "o"s correspond to the back-to-back sensitivity and the "x"s correspond to the sensitivity with a 80 km SCF channel. It is apparant that low-order filters, hence slower roll-offs, have better sensitivities than high-order filters. The receiver sensitivity for each filter order corresponds to the best filtering bandwidth. This plot was generated by using Butterworth electrical filters with zero channel dispersion. Similar trends are seen for different filter types and also different channel dispersions.

PSK duobinary signals, filters with slow roll-offs have better sensitivities than filters with higher roll-offs. This is apparant from figure 4-3, which shows a plot of the sensitivity (corresponding to the best filtering bandwidth) as a function of filter order for a Butterworth filter with a zero dispersion channel. The 3rd order Butterworth filter yields a 3-dB better senstivity than the 12th order Butterworth filter. The trend seen in figure 4-3 also applies to other filter types (e.g. Chebyshev) and to other channel dispersions.

The optimal filtering bandwidth depends on the filter roll-off. As expected, filters with fast roll-offs have wider optimal bandwidths than filters with slow roll-offs. As shown in figure 4-4, the optimal filtering bandwidth increases with filter order (from $0.7B$ to $1.1B$ with a 0 km channel) and decreases with increasing dispersion (by approximately $+0.1B$ over 80 km of propagation).

The filter bandwidth and order are the two most important parameters affecting the BER. Of lesser importance is the passband ripple in either magnitude or phase.

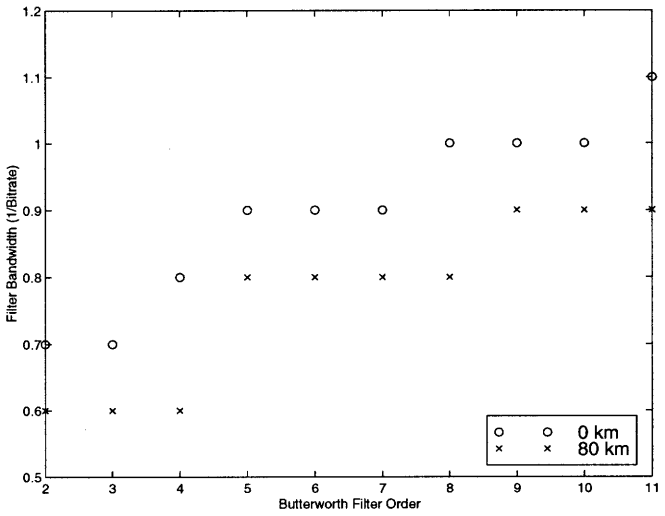

Figure 4-4: The optimal electrical bandwidth is plotted against the filter order. The optimal bandwidth increases with filter order and decreases with increasing dispersion. The plot was optimized over bandwidth steps of $0.1B$.

Chebyshev filters with different maximum passband ripple were analyzed. The difference in receiver sensitivity between ripple magnitudes of 0.1, 0.5 and 1 dB is small, as can be seen in figure 4-5. The sensitivity difference between the 0.1- and 1-dB maximum ripple Chebyshev filters is approximately 1 dB, but the difference is much smaller at the optimal filtering point.

4.2 Filtering of Alternating- and Blocked-Phase Duobinary Signals

Alternating- and blocked-phase duobinary formats have the unfortunate property that they are chirped with alternating signs at their pulse edges. The drastic dispersion penalty resulting from the chirped pulses has made these formats less interesting for non-dispersion-compensating, single-span transmission. Therefore, these formats will not be discussed in detail in this section. The only notable aspect is that alternating-phase duobinary signals have wider optimal filtering bandwidths than blocked-phase duobinary signals. This should be expected since the spectrum of a alternating-phase duobinary signal has twice the bandwidth of a blocked-phase duobinary signal. After

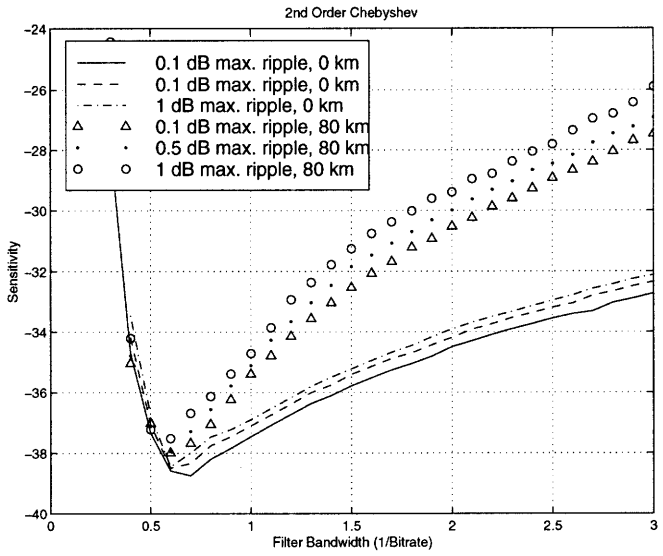

Figure 4-5: The sensitivity as a function of 2nd order Chebyshev filter bandwidths for a AM-PSK duobinary signal. The bottom three curves correspond to a 0 km channel and the top three curves correspond to an 80 km channel of regular silica core fiber. At the optimal filtering bandwidth, the sensitivity difference among 0.1-, 0.5- and 1-dB maximum ripple Chebyshev filters is less than 1 dB.

80 km of propagation through SCF, the optimal filtering bandwidths are $1.1B$ and $0.8B$ for alternating- and blocked-phase duobinary formats, respectively (see figure 4-6).

4.3 Receiving Filter Considerations

So far, the receiving electronic filter bandwidth was assumed to be the same as that of the transmitting filter, since this usually gives the best results. Figures 4-7 and 4-8 show the receiver sensitivity of a AM-PSK duobinary transmission simulation as a function of the transmitting and receiving electrical bandwidths of second-order Bessel filters. Figure 4-7 shows the sensitivity at 0 km of propagation and figure 4-8 shows the sensitivity after 100 km of propagation. Although simulations show that the best sensitivities are obtained for approximately equal transmitting and receiving bandwidths unless the receiving filter is cutting greatly into the signal spectrum, the BER is not a sensitive function of the receiving filter bandwidth. The choice of the receiving filter becomes more important at high dispersion, as can be seen in

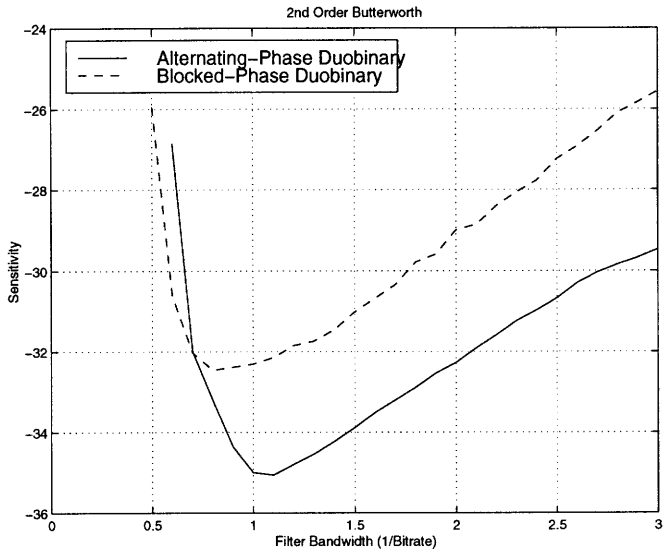

Figure 4-6: Receiver sensitivity is plotted as a function of the electrical filter bandwidth for alternating- and blocked-phase duobinary modulation formats. The channel is 80 km of standard silica core fiber, which yields a total dispersion of 1360 ps/nm. It can be seen that the optimal filtering bandwidths (corresponding to the minima) are $1.1B$ and $0.8B$ for alternating- and blocked-phase duobinary formats, respectively.

figure 4-8.

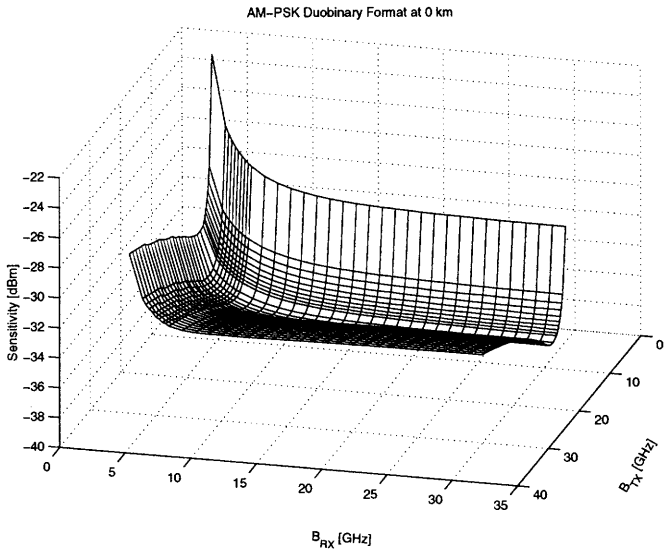

Figure 4-7: Sensitivity versus transmitter and receiver electrical bandwidth for 10 Gbit/s NRZ **AM-PSK duobinary format at 0 km** of standard fiber. The electrical filter in the transmitter is modeled as a 2nd order Bessel LPF. The optimal filtering is given by a transmitter bandwidth of about 7 GHz and an infinite receiver bandwidth.

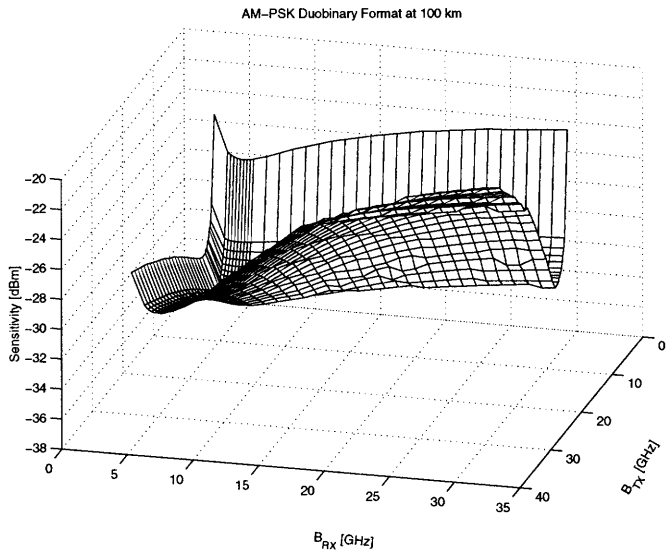

Figure 4-8: Sensitivity versus transmitter and receiver electrical bandwidth for 10 Gbit/s NRZ **AM-PSK duobinary format at 100 km** of standard fiber. The electrical filter in the transmitter is modeled as a 2nd order Bessel LPF. The optimal filtering is given by a transmitter bandwidth of about 7 GHz and a receiver bandwidth of about 6 GHz.

Chapter 5

The Relationship Between Noise and Dispersion Penalty

It has been general practice to measure the performance of a receiver in a transmission system by measuring its sensitivity when the transmitter is directly connected to the receiver. This parameter is called the back-to-back sensitivity. Therefore, according to this rating system, the top curve in figure 5-1 would be labeled a "poor" receiver when compared to the bottom curve, a "good" receiver, since the sensitivity of the "good" receiver is better than the sensitivity of the "poor" receiver at 0 km or 0 ps/nm total channel dispersion. This rating system of receivers is problematic when operating a transmission link with a net high total dispersion (a very common case) since the difference between sensitivities of the two receivers can be negligable. Therefore, classifying a receiver by its back-to-back performance is not necessarily an accurate indicator of its performance in a true linear dispersive repeaterless transmission system. Therefore the "best" receiver is dependent on the entire transmission system.

The reason why the sensitivities of the two receivers in figure 5-1 become comparable at high dispersions can be understood by carefully considering the amount of noise on a mark compared the amount of noise on a space, or, in other words, the mark to space standard deviation ratio (σ_1/σ_0). The only difference between the two receivers represented by the curves in figure 5-1 is the relative amount of noise on

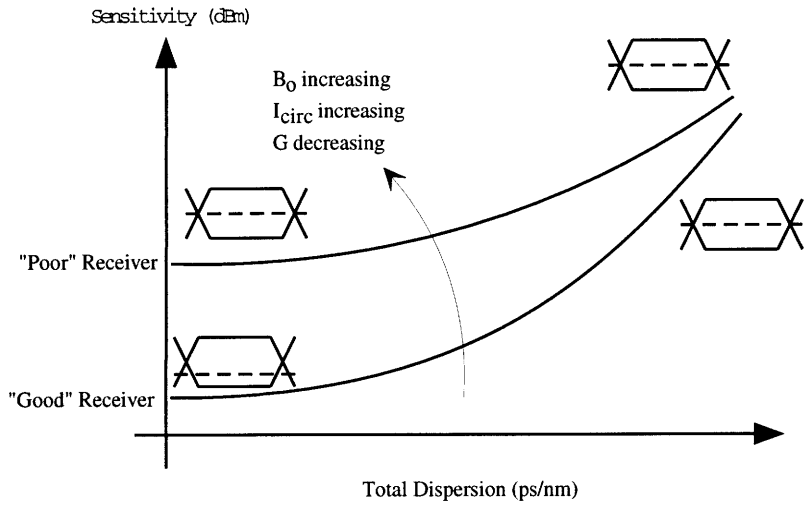

Figure 5-1: Sensitivity as a function of total dispersion for a "good" and "bad" receiver. The eye diagrams show the threshold (dashed line) at different parts of the curve. Notice that the threshold is very near the spaces for the"good" receiver at low dispersions. This means that signal-dependent noise terms dominate at that point.

the marks and spaces. As will be shown in subsection 5.2, the high σ_1/σ_0 ratios lead to high incremental power penalties. Since the lower curve initially has a high σ_1/σ_0 ratio, it experiences a larger penalty and hence the bottom curve is intially steeper than the top curve. At higher total dispersions, the two curves have σ_1/σ_0 ratios approaching 1 and the steepness of both curves are approximately the same. Therefore, the sensitivities of both receivers will approach each other at higher dispersion.

The next section will present simulation and experimental results that demonstrate the dependence of the dispersion penalty on the σ_1/σ_0 ratio. The following section will develop a conceptual model that explains this behavior.

5.1 Simulation and Experimental Results

To be more precise by what is meant by a "good" and "poor" receiver, a "poor" receiver could have a higher circuit noise, higher optical band pass filter bandwidth B_O (hence allowing more ASE power hit the detector) [1], or lower preamplifier gain, G, than a "good" receiver. Plots of the sensitivity as a function of the total dispersion

[1]Recall that there is an OBPF in the optical pre-amplifier.

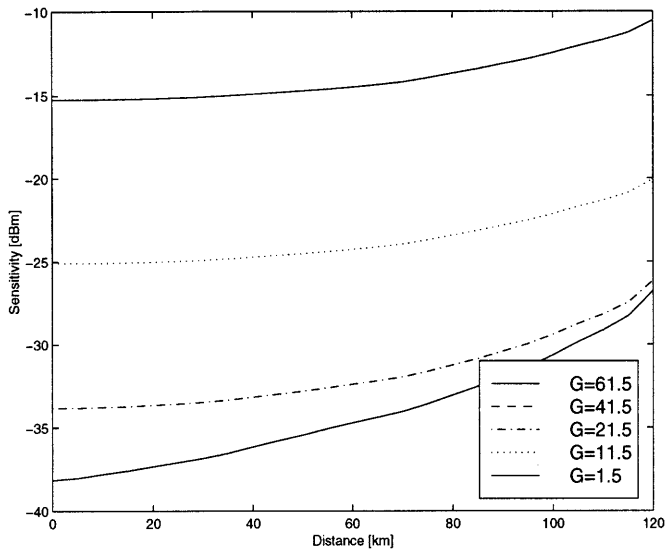

Figure 5-2: Sensitivity versus dispersion [ps/nm] for several optical pre-amplifier gains for a 10 Gbits/s binary amplitude modulated signal.

for different B_O and G are examined in this section.

Figure 5-2 and figure 5-3 show the total dispersion versus sensitivity for different pre-amplifier gain, G, values (the receiver parameters for the simulations in this section are tabulated in table 5.1). Figure 5-2 is plotted for binary NRZ format and figure 5-3 is plotted for AM-PSK duobinary format. Focusing on the 0 km or 0 total dispersion points in both figures, the receivers corresponding to higher G's have better sensitivities. Although not shown in the plots, at zero total dispersion the σ_1/σ_0 ratio increases for higher G. At higher total dispersions, the penalties for the curves corresponding to the greater G's are larger. This can more easily be seen if the penalties rather than the sensitivities are plotted. Figure 5-4 and figure 5-5 show the penalties for binary and AM-PSK duobinary NRZ formats respectively. In these plots, it is clear that the higher G's correspond to a greater penalty.

The "goodness" of a filter can also be varied by changing the optical bandwidth. By changing the width of the optical band-pass filter in the optical pre-amplifier, we can control the window in which the ASE noise is incident upon the detector. The wider the window, the more noise is allowed through. Figure 5-6 shows the receiver sensitivity for two different receiving optical filters. The wider 10 nm filter has a worse sensitivity than the narrower 0.33 nm filter. The squares and triangles correspond to

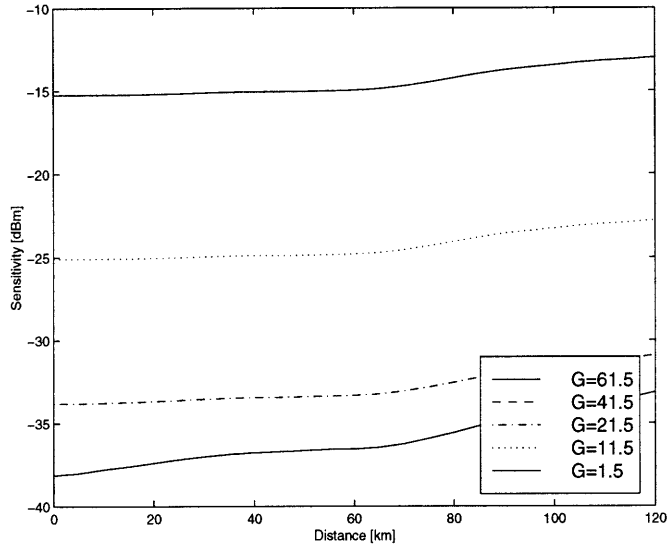

Figure 5-3: Sensitivity versus dispersion [ps/nm] for several optical pre-amplifier gains for a 10 Gbits/s AM-PSK amplitude modulated signal.

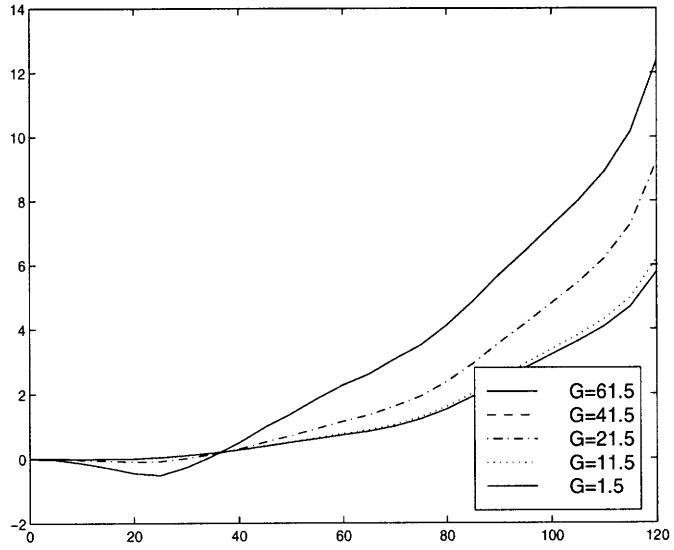

Figure 5-4: Penalty versus dispersion [ps/nm] for several optical pre-amplifier gains for a 10 Gbits/s binary amplitude modulated signal.

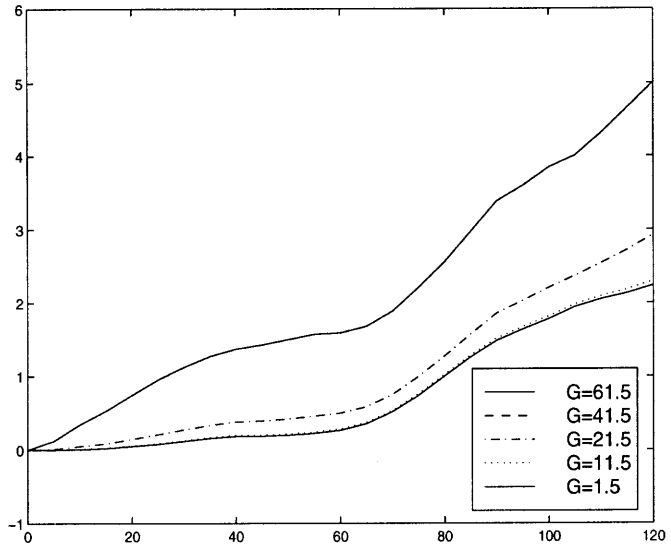

Figure 5-5: Penalty versus dispersion [ps/nm] for several optical pre-amplifier gains for a 10 Gbits/s AM-PSK duobinary amplitude modulated signal.

Symbol	Value used in Gain Simulations	Value used in Optical Filter Simulations	Explanation
q	1.6×10^{-19} C	1.6×10^{-19} C	Electron charge (positive)
p	2	2	Number of polarization states detected
B_{el}	6.5GHz (duobinary), 10 GHz (binary)	10 GHz	Bandwidth of the electronics in the receiver (single-sided)
B_0	0.33 nm	0.33, 10nm	Bandwidth of the optical filter in the receiver (double-sided)
η	0.8	0.8	Quantum efficiency of the PIN photodiode
n_{sp}	1.172	1.172	Amplifier spontaneous emission factor
σ_{th}	2.99785×10^{-11} A^2	2.99785×10^{-11} A^2	Thermal, Circuit, or Johnson Noise
L_0	0.7943	0.7943	Output coupling loss of optical pre-amplifier (expressed as a ratio)
L_I	1	1	Input coupling loss of optical pre-amplifier (expressed as a ratio)
G	1.5-301.5 dB	41.5 dB	Optical pre-amplifier gain
I_S			Input electrical current after the PIN photodiode= $\frac{\eta q}{h\nu} L_I G L_0 P_{\text{optical}}$
f			$\eta n_{sp}(G-1)L_0$

Table 5.1: Explanation of noise variable terms and values used in the simulations.

experimental data taken with a 10 Gb/s binary modulated $2^{31} - 1$ pseudo-random bit sequence. The other lines correspond to simulated values.

All the figures in this section show that there is indeed a connection between the dispersion penalty and the σ_1/σ_0 ratio. The next section will explain why this behavior should be expected.

5.2 A Conceptual Model

The conceptual model consists of considering four bits, perturbing the power level of the bits, and then computing how the power penalty grows as a function of increasing

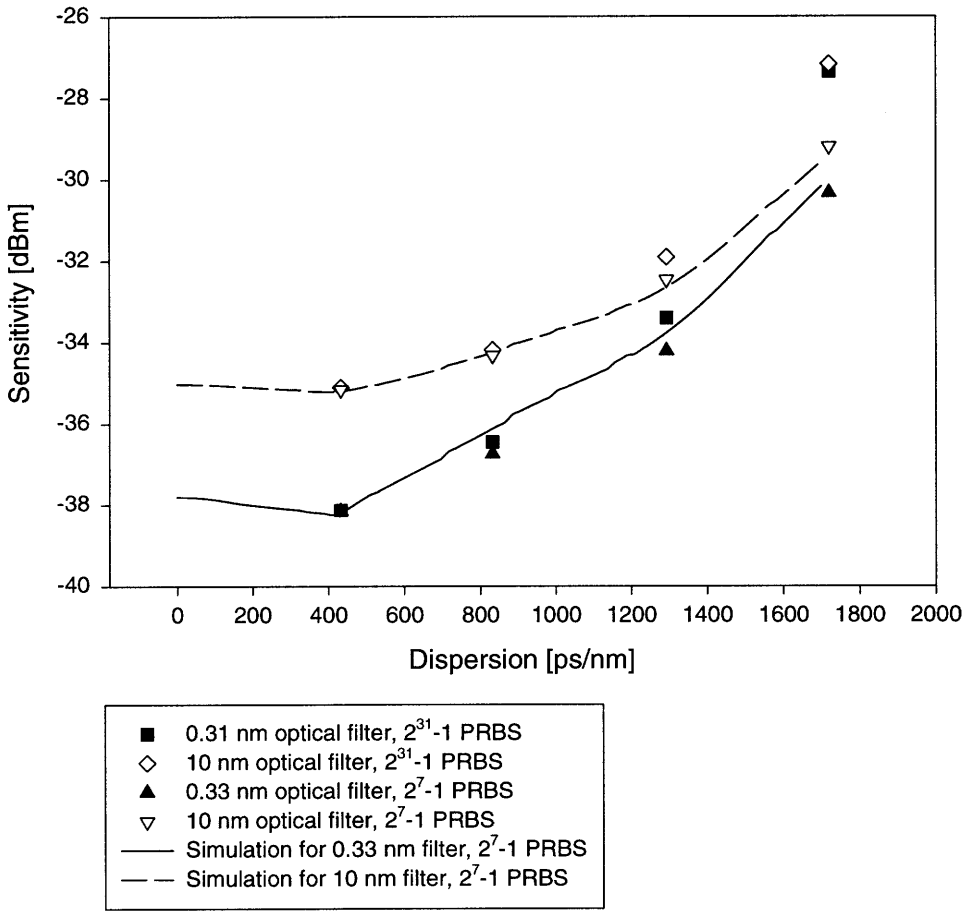

Figure 5-6: Dispersion [ps/nm] versus receiver sensitivity for different receiving optical filters. The squares and triangles represent experimental data taken with 10 Gbit/s binary modulated $2^{31} - 1$ pseudo-random bit sequences for optical filter bandwidths of 10 nm and 0.33 nm respectively. The circles and dashed lines represent the corresponding simulated values.

σ_1/σ_0.

Consider a signal consisting of 4 bits: 2 marks and 2 spaces whose eye diagram is plotted in figure 5-7. Each mark and space is assumed to have a gaussian distribution characterized by a mean and a variance. Initially the marks have the mean μ and variance σ_1, and the spaces have zero mean and variance σ_0. The ratio of the mark to space standard deviation is σ_1/σ_0 and the initial BER is 10^{-9} (This initial configuration corresponds to the first eye diagram in figure 5-7). A perturbation of the bits' power levels (or means) due to dispersion, nonlinearities or other effects causes an increase in the BER. More specifically, the perturbation causes a shift of the mean of one of two marks and one of the two spaces by Δp toward the center of the eye (see the second eye diagram in figure 5-7). The variances of the perturbed levels (see figure 5-7) are

$$\begin{aligned} \sigma_{1,top} &= \sigma_1 \\ \sigma_{1,bot} &= \sqrt{k(\mu - \Delta p) + \sigma_0^2} \\ \sigma_{0,top} &= \sqrt{k\Delta p} \\ \sigma_{0,bot} &= \sigma_0 \end{aligned} \tag{5.1}$$

where $k = \frac{\sigma_1^2 - \sigma_0^2}{\mu}$. The perturbed eye has an increased BER. To re-establish the initial BER of 10^{-9}, power must be added to the marks to separate the mark and space probability density distributions. This incremental power is $\Delta\mu$ and the third eye in figure 5-7 corresponds eye diagram with the incremental added power. The variances of the perturbed levels after the added power are

$$\begin{aligned} \sigma'_{1,top} &= \sqrt{k(\mu + \Delta\mu) + \sigma_0^2} \\ \sigma'_{1,bot} &= \sqrt{k(\mu + \Delta\mu - \Delta p) + \sigma_0^2}. \end{aligned} \tag{5.2}$$

The power penalty, $\Delta\mu$, can be computed as a function of the initial mark to space

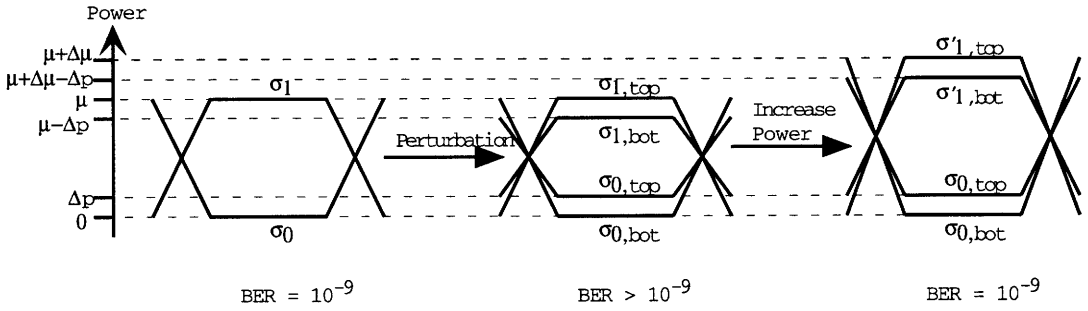

Figure 5-7: Schematic diagram of conceptual model.

standard deviation, σ_1/σ_0. Letting $\mu = 1$ and $\Delta p = \mu/100$, the power penalty is computed and plotted in figure 5-8. This figure shows that the power penalty increases with increasing σ_1/σ_0.

Now it is possible to explain the behavior of the sensitivity plots in the previous section. A "good" receiver generally has a high σ_1/σ_0 value at low total dispersions. This is another way of saying that the noise in a "good" receiver is dominated by signal-dependent noise, since the signal-independent noise is comparatively lower. As the received eye is increasingly perturbed by dispersion, the mark and space levels spread. The spreading of the space levels causes the spaces to have non-zero energy. Since the variances of the spaces are dependent on the power-level (also refered to as the mean or first moment), the variances of the spaces start to increase and approach the variances of the marks. This means that σ_1/σ_0 approaches 1 and the dispersion penalty of the "good" receiver starts to decrease relative to the "poor" receiver.

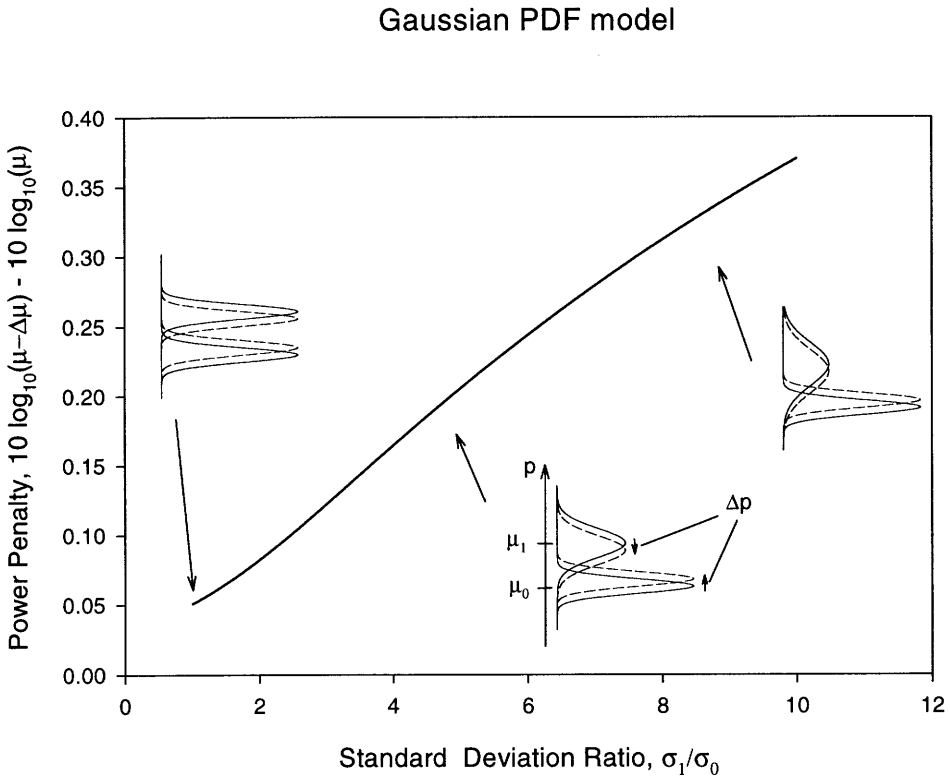

Figure 5-8: The dispersion penalty plotted against the ratio of the mark and space standard deviations. Sample Gaussian probability density functions are shown for different variances.

Chapter 6

Stimulated Brillouin Scattering of Duobinary Optical Signals

6.1 Overview

Stimulated Brillouin scattering (SBS) is the scattering (ω_s) of a pump or signal (ω_p) from a travelling refractive index gradient in a fiber. The refractive index gradient is induced by an acoustic wave (ω_A). A diagram of the three interacting k-vectors is shown in figure 6-1. This nonlinear process is currently the greatest limiting factor in repeaterless optical communications since SBS limits the launch power. In addition, the interaction between the pump and Stokes wave is a chaotic process that causes variation of the transmitted bits and hence degrades the BER. The amount of backscattering power increases quickly as the pump power increases past the SBS

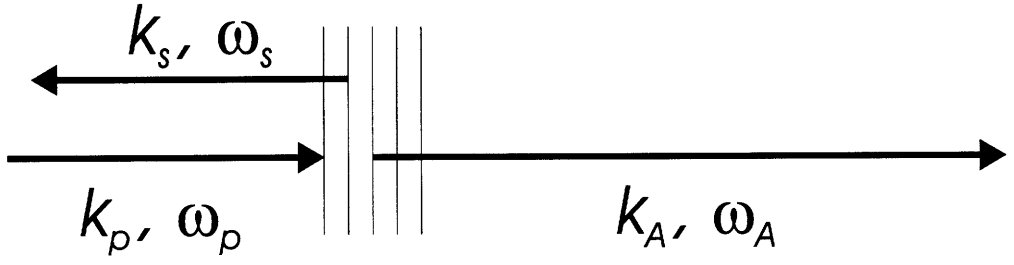

Figure 6-1: Schematic illustration of stimulated Brillouin scattering. The three k-vectors correspond to the Stokes (ω_s), pump (ω_p) and acoustic (ω_A) waves.

threshold power. According to the conventional definition, the SBS threshold is the input power at which the Stokes power is equal to signal power at the end of the fiber.[47] Since the length of the fiber is arbitrary, it makes more sense to re-define the SBS threshold as the necessary input power so that the backscattered SBS power equals the Rayleigh backscattered power[1].

The goal is to find the SBS threshold for different modulation formats as a function of bit rate. The power of the backscattered SBS wave grows exponentially in the reverse direction according to $I_s(0) = I_s(L)\exp(G - \alpha L)$ where G is the SBS gain, $I_s(L)$ is the initial input power at $z = L$, and α is the loss coefficient. The first section will use the signal spectra derived in chapter 2 to find G. The next section will show how to find the threshold power from G. The last section will contain both experimental and theoretical plots of the SBS threshold power for the different signal formats mentioned previously.

6.2 The SBS Gain Coefficients

The gain of a Stokes wave in stimulated Brillouin scattering is characterized with the SBS gain parameter, G, and will be the single most important parameter for determining the SBS threshold in the following section. The SBS Stokes wave's growth is proportional to $\exp[G]$. The SBS gain, as derived in Appendix C, is

$$G = g\Gamma L_{eff} \int_{-\infty}^{\infty} \frac{I_p(f)}{\Gamma^2 + (f - f_S - f_A)^2} df \tag{6.1}$$

where g is the SBS gain coefficient, Γ is the Brillouin linewidth, f_S is the Stokes (SBS) wave frequency, L_{eff} is the effective length of the fiber, and f_A is the acoustic wave frequency. Equation (6.1) is a convolution of the signal spectrum, $I_p(f)$, with the Lorentzian Brillouin gain spectrum.

Given a CW pump wave with the power spectral density $I_p(f) = I_0\delta(f)$, the

[1]Rayleigh scattering is the scattering from random density fluctuations in fused silica due the imperfect manufacturing process. Rayleigh scattered light is omnidirectional and the scattering loss varies as $1/\lambda^4$. Therefore, Rayleigh scattering becomes a major problem at short wavelengths.

Signal Format	SBS gain, G
NRZ Binary[17, p.449]	$G_{CW}\left[1-\frac{1}{4\pi\Gamma_B T}\left(1-e^{-2\pi\Gamma_B T}\right)\right]$
NRZ AM-PSK Duobinary	$G_{CW}\left[1-\frac{1}{4\pi\Gamma T}\left(1-e^{-4\pi\Gamma T}\right)\right]$
NRZ Alternating Phase Duobinary	$G_{CW}\Gamma_B^2 T\int_{-\infty}^{\infty}\frac{\mathrm{sinc}^2(\pi fT)(1-\cos 2\pi fT)}{\Gamma_B^2+f^2}df$
NRZ Blocked Phase Duobinary	$G_{CW}\left[1-\frac{1}{4\pi\Gamma T}\left(1-e^{-4\pi\Gamma T}\right)\right]$
RZ Binary	$G_{CW}\Gamma_B\left\{\pi e^{-2\pi^2\Gamma_B^2/\alpha}\left(1-\mathrm{erf}\left(\pi\Gamma_B\sqrt{\frac{2}{\alpha}}\right)\right)+\frac{1}{T}\sum_{k=-\infty}^{\infty}\frac{\exp\left(\frac{-2\pi^2\left(\frac{k}{T}\right)^2}{\alpha}\right)}{\Gamma_B^2+\left(\frac{k}{T}\right)^2}\right\}$
RZ Alternating Phase Duobinary	$G_{CW}\Gamma^2\sqrt{\frac{2\pi}{\alpha}}\int_{-\infty}^{\infty}\frac{e^{-2\pi^2 f^2/\alpha}(1-\cos 2\pi fT)}{\Gamma^2+f^2}df$
RZ Blocked Phase Duobinary	$G_{CW}\Gamma^2\sqrt{\frac{2\pi}{\alpha}}\int_{-\infty}^{\infty}\frac{e^{-2\pi^2 f^2/\alpha}(1+\cos 2\pi fT)}{\Gamma^2+f^2}df$

Table 6.1: SBS Gain for several binary PAM formats

steady-state SBS gain is

$$G_{CW}=\frac{gI_0L_{eff}}{\Gamma_B} \tag{6.2}$$

and substituting this into (6.1) yields

$$G=G_{CW}\frac{\Gamma_B^2}{I_0}\int_{-\infty}^{\infty}\frac{I_p(f)}{\Gamma_B^2+(f-f_S-f_A)^2}df \tag{6.3}$$

As shown in (6.3), the SBS gain depends on the signal spectrum, $I_p(f)$, or, in other words, the modulation format. The SBS gain for NRZ binary, NRZ blocked phase duobinary, RZ alternating phase duobinary, and RZ blocked phase duobinary signals can be found by substituting (2.23), (2.26), (2.27), (2.35), and (2.36) respectively into (6.3). The results are tabulated in table 6.1.

6.3 The SBS Threshold Power

In this paper, the SBS threshold is defined as the necessary input power so that the backscattered SBS power equals the backscattered Rayleigh scattered power. The total stimulated Brillouin backscattered power at the launch end of the fiber can be

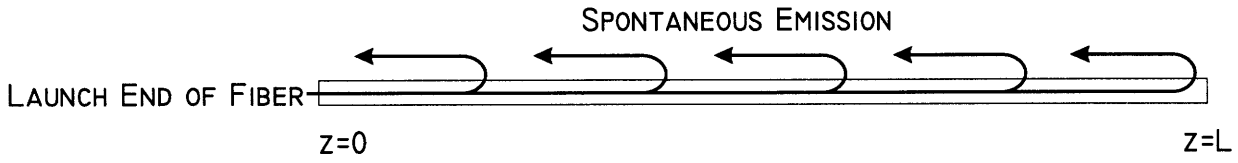

Figure 6-2: Spontaneous emission occurs along the length of a fiber. Each spontaneously emitted photon experiences Brillouin gain in the backward direction.

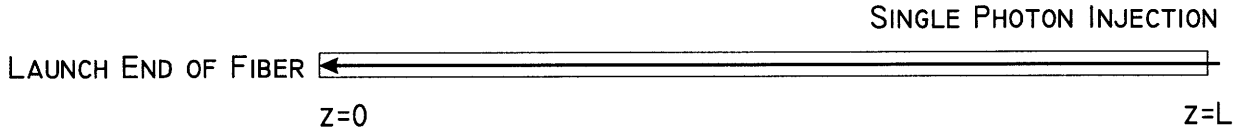

Figure 6-3: The SBS power at the launch end of the fiber can be calculated by injecting 1 photon per mode at $z = L$.

found by summing all the contributions from spontaneous emission multiplied by the gain of the Brillouin process along the fiber (see figure 6-2). Smith [47] has shown that for purely spontaneous scattering, this summation is approximately equivalent to the injection of a single Stokes photon per mode at the point ($z = L$) along the fiber where the nonlinear gain ($I_s(0)/I_s(L)$) exactly equals the loss of the fiber, α (see figure 6-3). According to Smith, the SBS backscattered power can be written as

$$P_s(0) = \int df_s h f_s \exp\left[-\alpha L + G(f_s)\right] \tag{6.4}$$

where $P_s(0) = I_s(0)A_{eff}$ is the backscattered Stokes power, hf_s is the power of the injected Stokes photon at $z = L$, α is the loss of the fiber, and G (a function of f_s) is the SBS gain defined by (6.1), and it is assumed that a single-mode fiber is used. The Stokes frequency, f_s, that contributes the most power to the Stokes wave returning to the beginning of the fiber is the frequency that maximizes G. Since G is exponentially related to backscattered power, only the f_s corresponding to maximum G will contribute significantly to the backward propagating power. Therefore, it is reasonable to approximate (6.4) with

$$P_s(0) = hf_s' \exp\left[-\alpha L + G(f_s')\right] \tag{6.5}$$

where f_s' is the Stokes frequency that maximizes G. Solving this equation for G yields

$$G = \ln \frac{P_s(0)}{hf_s} + \alpha L. \tag{6.6}$$

where the prime in f_s' has been dropped for notational convenience. Next, we can invoke the definition of G (6.1) and write the SBS gain as

$$\begin{aligned} G &= g\Gamma L_{eff} \int_{-\infty}^{\infty} \frac{I_p(f)}{\Gamma^2 + (f - f_s - f_A)^2} df \\ &= \langle I_p \rangle \cdot g\Gamma L_{eff} \int_{-\infty}^{\infty} \frac{I_p^{normalized}(f)}{\Gamma^2 + (f - f_s - f_A)^2} df \\ &= \langle I_p \rangle \cdot \tilde{G} \end{aligned} \tag{6.7}$$

where $I_p(f) = \langle I_p \rangle I_p^{normalized}(f)$ (the brackets denote a spectral average so that $\int I_p^{normalized}(f) df = 1$), and $\tilde{G}$ is a normalized SBS gain such that it is purely a function of the shape of the pump spectrum,

$$\tilde{G} = g\Gamma L_{eff} \int_{-\infty}^{\infty} \frac{I_p^{normalized}(f)}{\Gamma^2 + (f - f_s - f_A)^2} df. \tag{6.8}$$

Substituting (6.7) for G in (6.6) and solving for $\langle I_p \rangle$ yields

$$\langle I_p \rangle = \frac{\ln \frac{P_s(0)}{hf_s} + \alpha L}{\tilde{G}} \tag{6.9}$$

The threshold power is achieved when $P_s(0)$ equals the Rayleigh backscattered power (which is approximately 30 dB less power than the launched signal power in standard silica core fiber). The numerator of (6.9) is equal to K at the threshold power,

$$\langle I_p^{threshold} \rangle = \frac{K}{\tilde{G}} \tag{6.10}$$

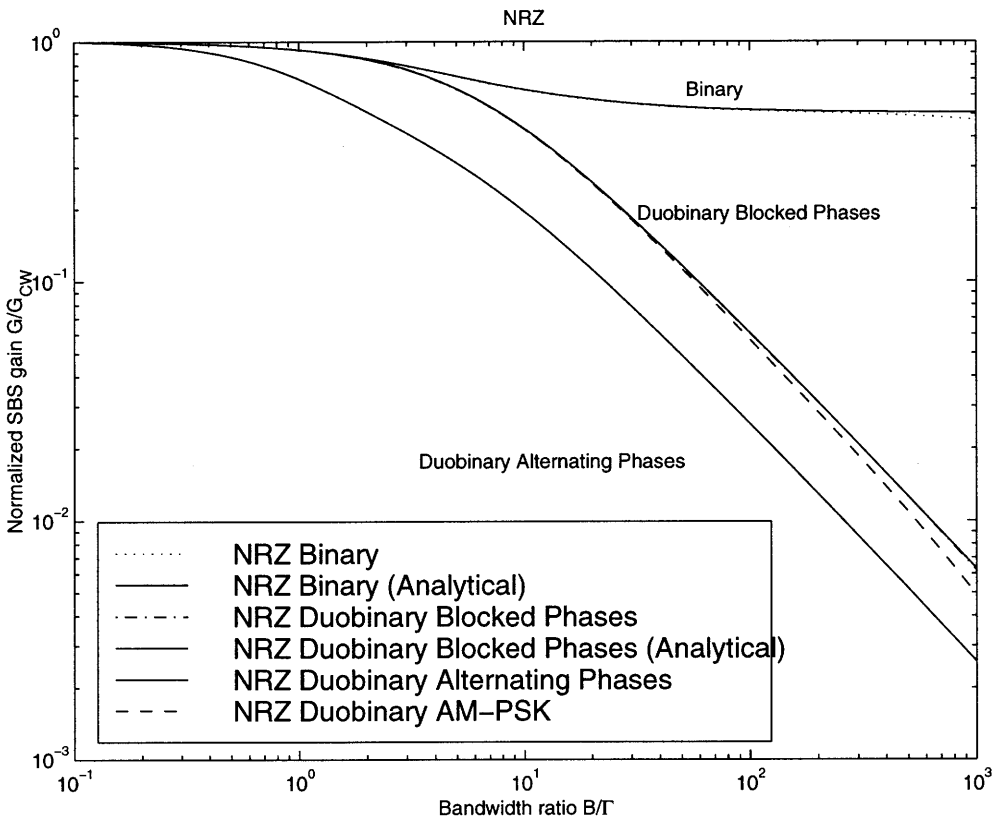

Figure 6-4: The SBS gains for NRZ transmission.

which means that the threshold power is proportional to $1/\tilde{G}$. For cw input, the threshold power becomes (by using (6.2) and normalizing according to (6.8))

$$\langle I_p^{threshold,cw} \rangle = \frac{K\Gamma}{gL_{eff}}. \tag{6.11}$$

The threshold power can be normalized to the cw threshold power by combining (6.10) and (6.11) and solving for K to obtain

$$\frac{\langle I_p \rangle}{\langle I_p^{threshold,cw} \rangle} = \frac{gL_{eff}}{\Gamma\tilde{G}}. \tag{6.12}$$

This form of the threshold power is convenient to plot. The SBS gains are plotted in figures 6-4, 6-5, and the normalized threshold powers are plotted in 6-6, and 6-7 for NRZ and RZ transmission. The cw SBS threshold power was measured to be 5 mW in our experiments with silica core fiber.

In figure 6-4, we see that for increasing bitrates, the SBS gain coefficient for

binary NRZ modulation levels off at half the value of the SBS gain coefficient for CW light. Intuitively, this makes sense, since a binary signal contains half its energy at the carrier frequency. At increasingly higher bitrates, the NRZ binary spectrum flattens but the carrier frequency power remains the same. According to the SBS gain coefficient integral, (6.3), the carrier frequency of the NRZ binary signal contributes almost entirely to SBS at high bit rates.

It is also interesting to notice in figure 6-4 that the G of the NRZ duobinary modulations decrease linearly. The power density spectra for these signals do not have delta functions in their power spectra. Therefore, at a higher bitrate, the power spectral density broadens, and the energy in the signal is spread over a larger frequency range. The SBS gain coefficient is the convolution of the broad signal power spectrum with the Lorentzian Brillouin gain spectrum. The maximum value of this convolution decreases with increasing bit rate, or in other words, the SBS threshold increases with increasing bit rate.

Experimentally, it was found that the threshold power of the NRZ alternating phase duobinary signal ranges from 17.78 dBm at 1 Gb/s to 26.02 dBm at 7 Gb/s. The threshold power of the blocked phase duobinary signal 14.7 dBm at 1 Gb/s to 21.7 dBm at 7 Gb/s. The threshold of the NRZ alternating phase duobinary signal is about 3 dB greater than the threshold of the NRZ blocked phase duobinary signal and the NRZ AM-PSK duobinary signal in this range. This can be explained by the power spectral densities for these signals in figures 2-20, 2-19 and 2-18 respectively, it is easy to see that the individual humps of the NRZ alternating phase duobinary signal have twice the width of the blocked phase or AM-PSK duobinary signals. This means that for the same power, the peak frequency of the alternating phase duobinary signal should be half the height, or 3 dB lower than the blocked phase and AM-PSK duobinary signals.

In figure 6-5 a similar picture to NRZ transmission is seen. For RZ binary modulation, the SBS gain levels out at about one-tenth of the CW SBS gain. The curves in figure 6-5 are for gaussian pulses whose FWHM occupies 16/100 of the bit slot. This number was picked since our experiments involved 16 ps FWHM pulses at 10

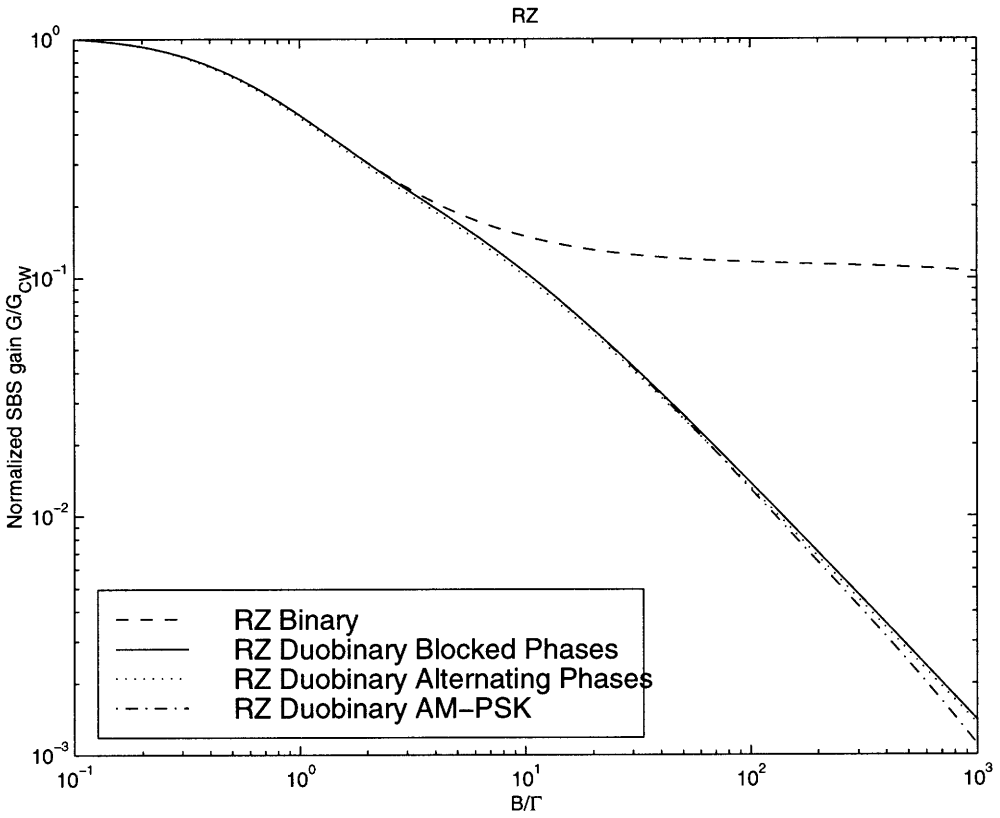

Figure 6-5: The SBS gains for RZ transmission.

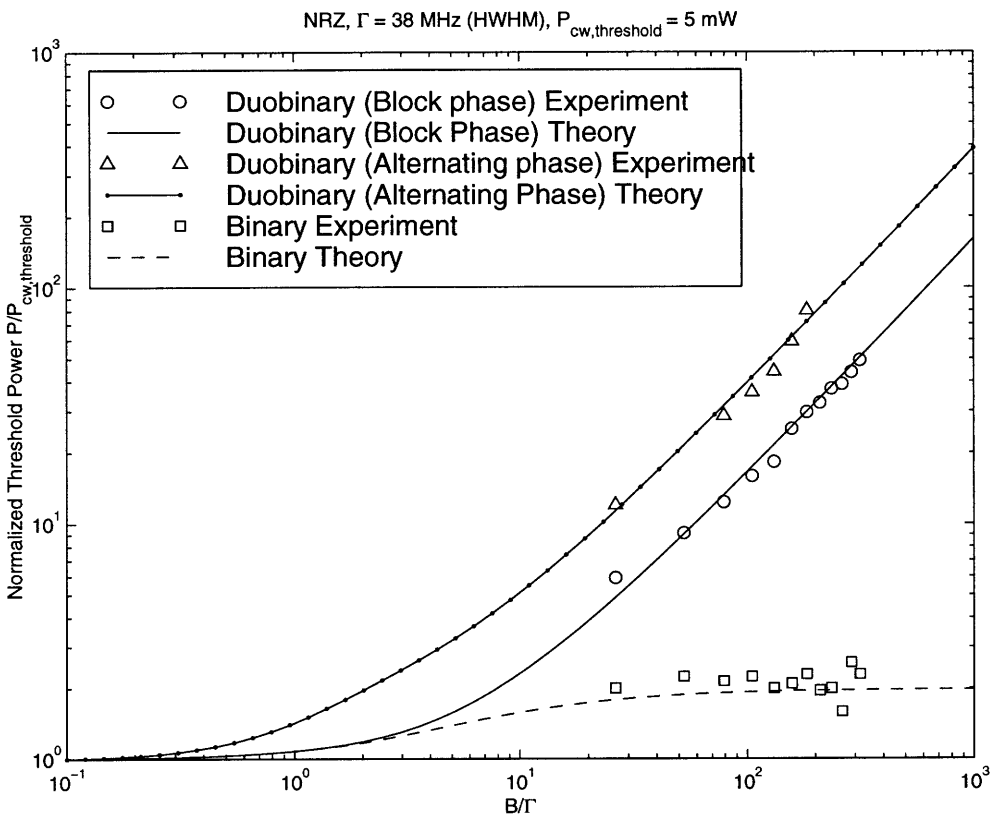

Figure 6-6: The normalized threshold powers for NRZ transmission. The experimental values are given by the circle, triangles, and squares.

Gbit/s. If the FWHM of the pulses were decreased *and* the pulse energies were fixed, the signal spectra would be broader, and therefore, the SBS gain should decrease. This would correspond to a downward shift of the curves in figure 6-5. Increasing the FWHM of the pulses would have the opposite effect.

Figures 6-6 and 6-7 show the normalized threshold powers for NRZ and RZ transmission. These curves were generated by plotting $1/(G/G_{CW})$ or the multiplicative inverse of figures 6-4 and 6-5. According to these plots, the SBS threshold for duobinary signals increases without bound as the bitrate increases, whereas the SBS threshold for binary modulated signals levels off after about $B = 10\Gamma$.

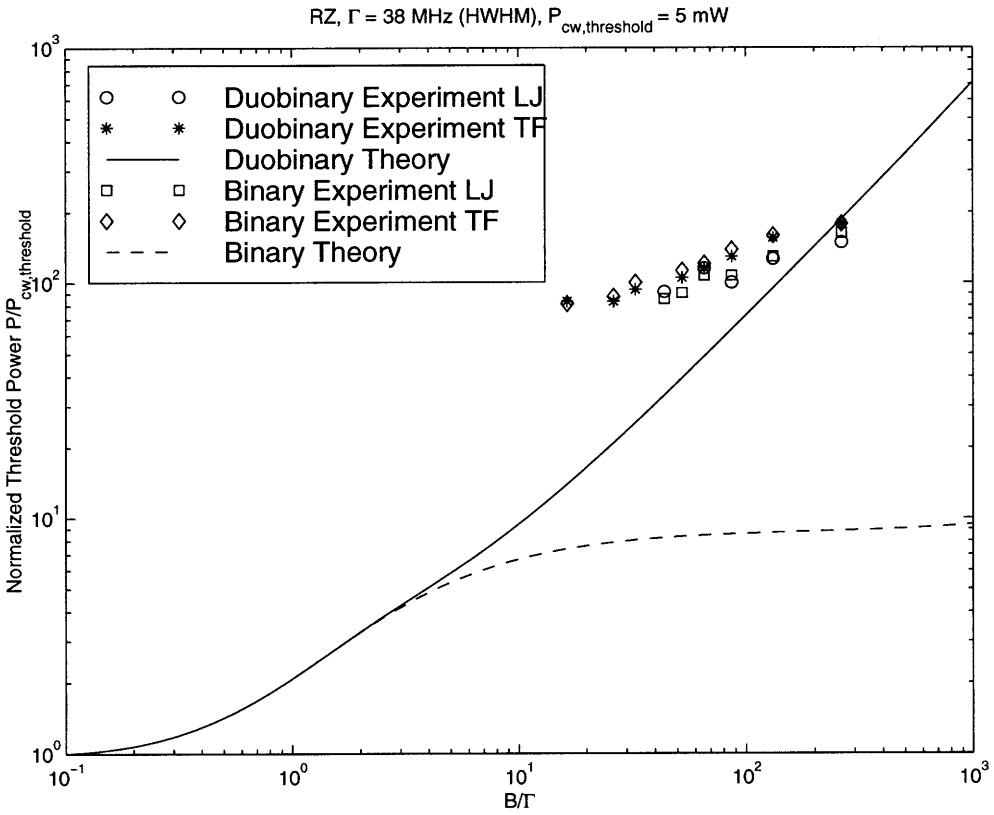

Figure 6-7: The normalized threshold powers for RZ transmission (assuming gaussian pulses with FWHM of 16 ps if bit slot has width 100 ps).

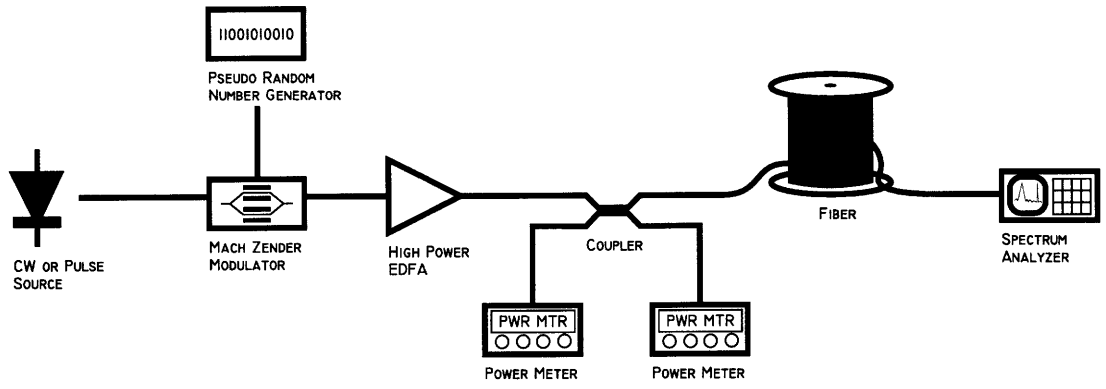

Figure 6-8: The experimental setup for determining the SBS threshold for various transmission formats.

6.4 Experiment

In the last section, we saw that the SBS threshold for RZ duobinary pulses increased without bound. This would be wonderful if it were actually true! Unfortunately, RZ pulses are limited by stimulated Raman scattering (SRS) and not SBS.

The experimental setup for finding the SBS threshold is shown in figure 6-8. The setup consists of a modulated laser source at 1557 μm, a high power erbium-doped amplifier, an attenuator, a coupler, several power meters, a spectrum analyzer, and 120 km if dispersion-shifted fiber (DSF) plus 40 km of silica-core fiber (SCF). The dispersion-shifted fiber was used to minimize dispersion, so that the modulated optical pulses could maintain their shape throughout the fiber.

The SBS threshold data for NRZ transmission, taken previously by Thorkild Franck [14], is plotted along with its values predicted by theory in figure 6-6. The experimental data corresponds well with theory showing that the theory developed in the previous section works well for NRZ transmission.

The RZ threshold experiments were slightly more complicated since the FWHM of the pulses could not be tuned. A 16 ps pulse source was used. In order to reduce the bitrate, rather than broadening the pulses, zeros were inserted after every digit in the $2^{13}-1$ pseudo-random bit sequence impressed by a Mach-Zender modulator onto the optical pulse stream. In effect this reduced both the bit-rate and the duty-cycle of the signal.

The backscattering threshold powers for RZ transmission (see figure 6-5) did not correspond well to the theory developed in this chapter. The measured threshold values were generally higher than the predicted thresholds. One hypothesis for the discrepancy between the measured and predicted values is that the pulses experienced a great amount of self-phase modulation (SPM) due to their high peak powers. Self-phase modulation leads to a broadening of the pulse spectrum. A broader pulse spectrum has a higher SBS threshold. Therefore, SPM causes an increase in the SBS threshold power, or in other words, the solid line in figure 6-5 is pushed upwards. Another reason for the discrepancy between the measured and predicted values is due to stimulated Raman scattering (SRS). As measured at the end of the fiber, the output spectrum showed that a considerable amount of the signal's energy was converted into Stokes radiation downshifted from the signal (see figures 6-9 and 6-10). This implies that less energy was available for the backward stimulated Brillouin scattering process, which effectively increases the SBS threshold.

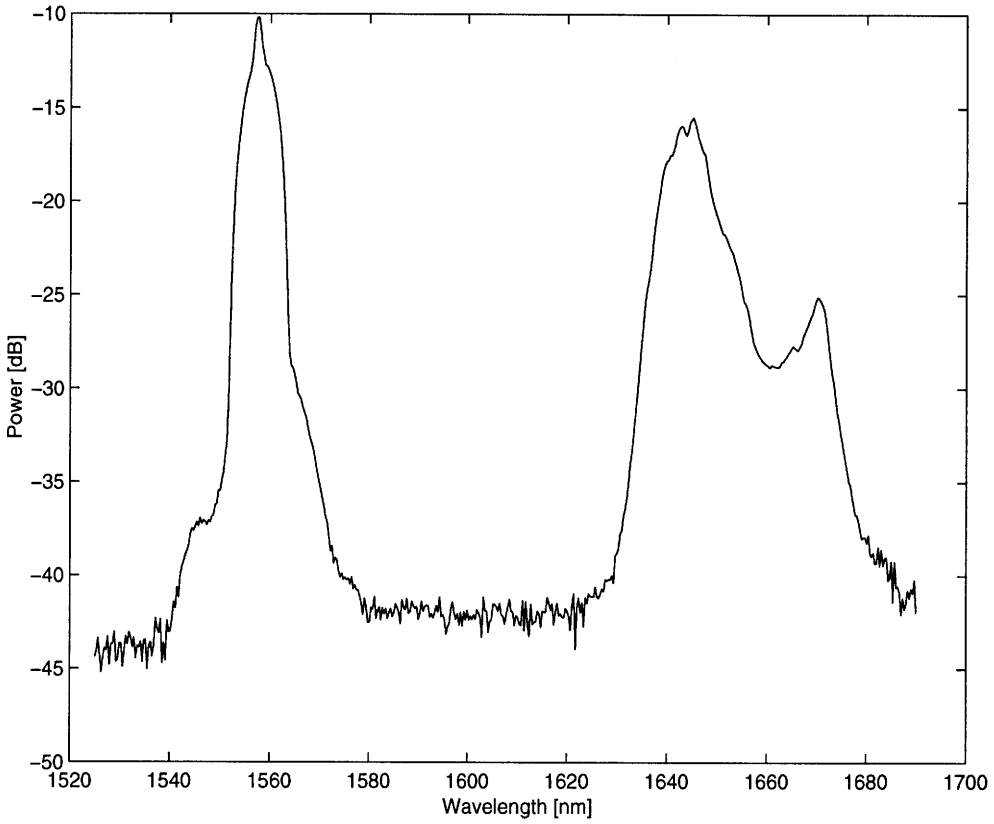

Figure 6-9: A sample spectrum of a $2^{13} - 1$ PRBS sequence taken at the end of the transmission fiber with a spectrum analyzer. Notice the SRS spectrum downshifted in frequency from the pump spectrum centered at 1560 nm.

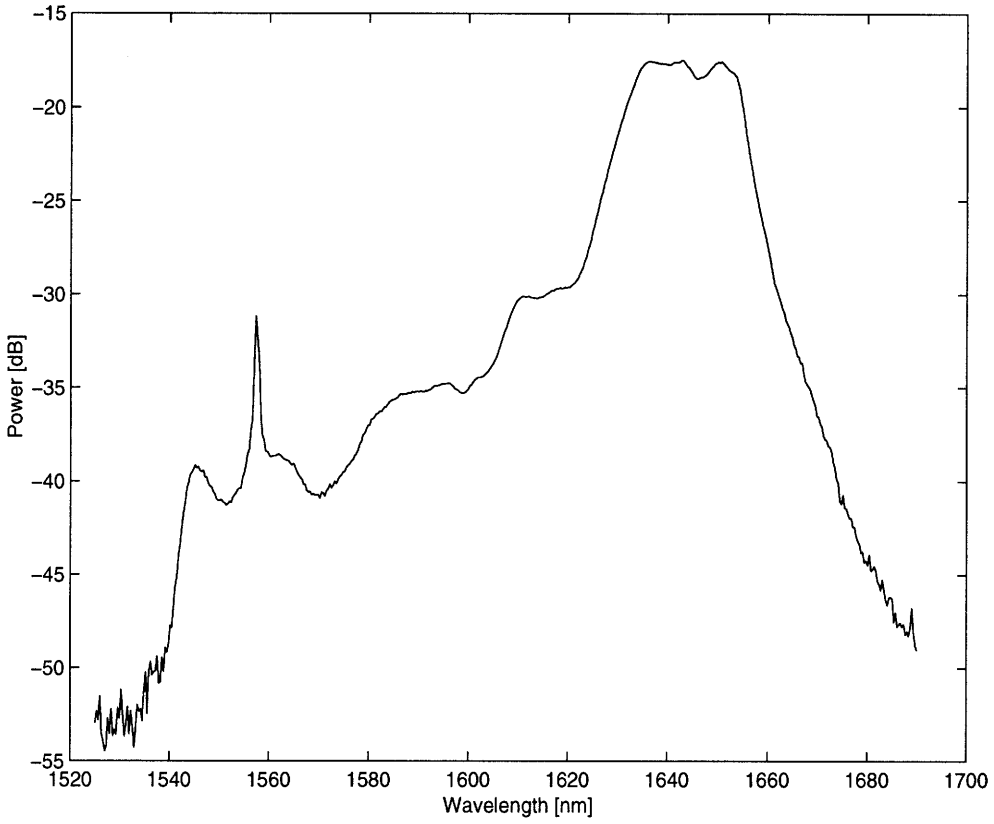

Figure 6-10: A sample spectrum of a $2^{13} - 1$ PRBS sequence with two spaces inserted between every bit, taken at the end of the transmission fiber with a spectrum analyzer. The pump is at 1560 nm.

Chapter 7

WDM of duobinary signals

Silica core fiber has an enormous usable bandwidth around the low loss 1.3 μm and 1.5 μm optical wavelengths. The approximate usable bandwidth (defined by the region in which the silica-core-fiber loss is less than approximaely 0.3 dB/km) around 1.5 μm is approximately 25,000 GHz wide [23, p.514]. In order to take full advantage of the 1.5 μm band with a single channel (a single laser diode), a laser diode or external Mach-Zender modulator would have to be modulated at 25,000 Gbit/s. This speed is impossible to obtain electronically and the current state-of-the-art modulators are only capable of approximately 50 Gbit/s modulation. In order to take advantage of the low loss 1.5μm band, it is necessary to use multiple channels. Wavelength division multiplexing (WDM) is the simultaneous broadcast of multiple independent signals with different carrier frequencies over a single fiber. WDM has become a popular way to expand capacity to meet the growing demand for information transfer.

Using multiple channels in a single fiber presents problems of crosstalk. Crosstalk occurs mainly through three mechanisms: (1) Individual channels have spectral tails that can become increasingly problematic as the channel spacing is decreased. (2) Non-ideal filtering or selection of a single channel which leads to a leakage of energy between neighboring channels. This interference manifests itself as high frequency wiggles of the marks in an eye diagram of the received signal. The high frequency wiggles arise from incompletely extinguished higher frequency neighboring channels. (3) Four-wave mixing (FWM), a phase-matching process allowed by the nonlinearity

of the fiber, causes an interaction between neighboring channels. In the spectral domain, the FWM spectrum centered at $\omega_4 = \omega_1 + \omega_2 - \omega_3$ can be thought of as a convolution of three (possibly doubly or triply degenerate) spectra corresponding to three channels centered at ω_1, ω_2 and ω_3.

As channels are packed more closely, the three aforementioned problems are exacerbated. As current WDM technology progresses from WDM (10 nm channel spacing) to dense WDM (1 nm channel spacing) and beyond, cross-talk will become an increasingly greater problem. One way to combat cross-talk between channels by linear mechanisms (specifically by mechanisms (1) and (2) mentioned above) is to increase the spectral efficiency of the modulation format by narrowing the channel spectrum. Duobinary format accomplishes exactly this.

Yano et al. [55] demonstrated 2.6 Terabit/s (132 ch. $\times$ 20 Gbit/s) WDM duobinary encoded transmission over 120 km silica-core fiber with a worst channel sensitivity of -27 dBm. The high density WDM signal had a 0.6 bit/s/Hz spectrum efficiency. This system used an IM duobinary format: 20 Gb/s binary signals were pre-coded and converted to three-level duobinary signals with 5 GHz 5th-order Bessel filters in the electrical part of the transmitter. In comparison, AT&T Labs demonstrated 1 terabit/s (50 ch. $\times$ 20Gbit/s) over 55 km in dispersion shifted fiber with binary NRZ format[8]. Fujitsu Laboratories demonstrated 1.1 Tb/s (50 ch. $\times$ 20 Gb/s) over 150 km in silica-core fiber with NRZ binary format. Assuming that the NRZ binary group used Erbium-doped fiber amplifiers with the same bandwidth as the Yano group (4.3 THz bandwidth), then the NRZ binary transmission experiments only had a spectrum efficiency of 0.25 bit/s/Hz.

Using the simulator developed in chapter 3, the sensitivities of a three channel system were computed for binary, AM-PSK duobinary, and IM (intensity modulated) duobinary modulation formats. Each channel was modulated at 20 Gbit/s and the back-to-back sensitivity (the sensitivity with the transmitter directly attached to the receiver) was computed for different channel spacings. For each modulation format, an exponential function was fitted to the sensitivities of all three channels. The result is plotted in figure 7-1 and the simulation parameters are tabulated in table 7.1. IM

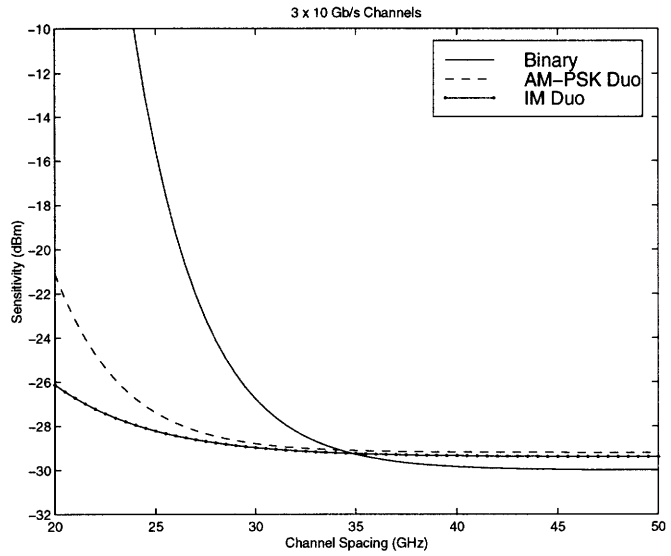

Figure 7-1: Sensitivity as a function of channel spacing for a 3 × 20 Gb/s WDM transmission simulation for binary, AM-PSK duobinary, and IM (intensity modulated) duobinary modulation formats.

and AM-PSK duobinary formats have better sensitivities at tighter channel spacing. Here, the tightest channel spacing, or channel efficiency, is defined to be the point at which the sensitivities increase by 1-dB. For channel spacings tighter than this, the sensitivity worsens very quickly. The 1-dB turning point for binary, AM-PSK duobinary, and IM duobinary modulation formats are 34 GHz, 27 GHz, and 25.8 GHz respectively, and the corresponding channel efficiencies are 0.59, 0.74 and 0.76 bit/s/Hz. Although the simulated channel efficiency values do not correspond exactly to experimental values, the relative values between modulation formats yields the important information. The deviation from experimental values comes from an inexact choice of parameters for the receiver, nonlinear effects in the fiber (FWM), and more complicated experimental setups that were not modeled, such as pre- and post-amplifiers. The important results from the simulation is that, (1) IM duobinary and AM-PSK duobinary formats yield better channel efficiencies than binary modulation format because of its narrower spectrum, and (2) IM duobinary channels can have slightly tighter packing than AM-PSK duobinary channels.

Parameter	Value
Channels	3
Bit Rate	20 Gbit/s
TX and RX electrical filters	20 GHz 2nd order Bessel LPF (for Binary modualation) 13 GHz 2nd order Bessel LPF (for AM-PSK duobinary modualation) 5 GHz 5th order Bessel LPF (for IM duobinary modualation)
PRBS	$2^7 - 1$
Samples per bit	32
Pre-amplifier gain, G	41.5 dB
Detector quantum efficiency, η	0.8
Receiver optical BPF bandwidth	0.3 nm
Circuit Noise	2.99785×10^{-11} AA
Pre-amplifier insertion loss	0
n_{sp}	1.172

Table 7.1: Simulation parameters used to generate figure 7-1.

Chapter 8

Conclusion

Duobinary encoding of optical NRZ signals presents a simple method of increasing the transmission distance over regular NRZ binary transmission without extra dispersion compensating devices. The only added complexity of a duobinary transmitter are the low-pass filters and the delay-and-add circuit block. Since the information of an optical duobinary signal is directly extracted from the signal's amplitude, the same direct-detection receiver as in binary NRZ communications can be used. The four reasons why duobinary encoding has become so attractive for optical transmission are: (1) it has a narrower bandwidth than binary format and hence suffers less from dispersion, (2) it has a greater spectrum efficiency than binary format due to its narrower bandwidth and hence allows tighter packing of wavelength division multiplexed channels, (3) it suffers less from stimulated Brillouin backscattering, the major limiting factor in repeaterless transmission, and (4) is easy to implement since the transmitter only requires modest changes from an externally modulated binary transmitter and since the receiver is a direct detection receiver, the same as for binary format.

In chapter 3, a computational model of a single-span, optically pre-amplified transmission system was presented. The optical pre-amplifier injected noise before a square-law detector (the *pin* photodiode receiver). Squaring the signal plus noise leads to beat terms. This means that part of the noise is signal-dependent and hence required the use of a computer to find bit-error rates. This computational model was

used in the rest of the thesis.

In chapter 4, sensitivities of Bessel, Butterworth, and Chebyshev filters of various orders were computed to understand what baseband filter (in both the transmitter and receiver) characteristics lead to the best BER. It was found that the most sensitive parameters affecting the BER are the bandwidth and roll-off steepness. The ripple across the passband in either phase or amplitude plays a smaller role in determining the BER. The best filtering for AM-PSK duobinary format is obtained for low-order, slow-roll-off filters with a bandwidth of approximately $0.6B$, where B is the bitrate. The optimal filtering bandwidth increases for higher-order, steeper-roll-off filters.

In chapter 5, the dispersion penalty of a receiver was shown to depend on the ratio of the mark-to-space noise (σ_1/σ_0). The main result was that high σ_1/σ_0 ratios lead to high dispersion penalty. This result has significance in the characterization of two receivers. The relative performance of two receivers with a 0 km fiber channel does not necessarily maintain that performance difference at 100 km, for example.

In chapter 6, the SBS threshold for AM-PSK, alternating- and blocked-phase duobinary formats were computed and experimentally verified. AM-PSK duobinary format has approximately a 20 times higher threshold at 10 Gbit/s and 40 times higher threshold at 20 Gbit/s than binary format (which, in our experiment, had a threshold of 10 mW). Alternating-phase duobinary format had approximately a 3-dB higher SBS threshold than AM-PSK and blocked-phase duobinary formats since its spectrum is approximately twice as wide. Since duobinary format has a high threshold, more power can be launched into a fiber than with a binary format, and hence longer transmission distances can be achieved.

Chapter 7 considered wavelength-division multiplexing of duobinary channels. It was shown through simulations that IM duobinary channel efficiencies of 0.76 bit/s/Hz could be expected (experiments have shown a channel efficiency of 0.6 bit/s/Hz). This corresponds to approximately twice the packing efficiency of binary format.

As the demand for more bandwidth increases, there will be a natural thrust towards creating amplifiers with broader bandwidths and using modulation formats that are more bandwidth efficient. Due to the excellent propagation properties of

duobinary format and the increasing interest in duobinary format in large firms such as Lucent Technologies, British Telecom, and NEC, it seems likely that duobinary transmission will play a larger role in future repeaterless transmission systems.

Appendix A

Filters

The squared-magnitude response, group delay, and impulse response of Butterworth, Bessel, and Chebyshev filters are plotted in this appendix. For all plots, the 3-dB cutoff frequency is normalized to 1.

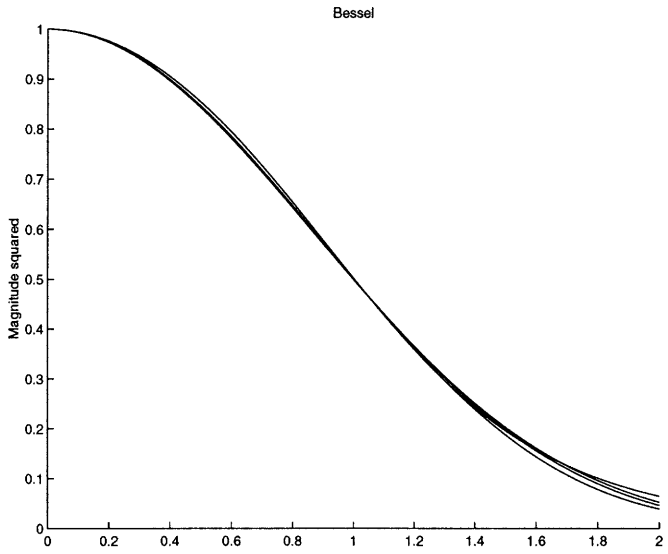

Figure A-1: Bessel filter squared-magnitude response.

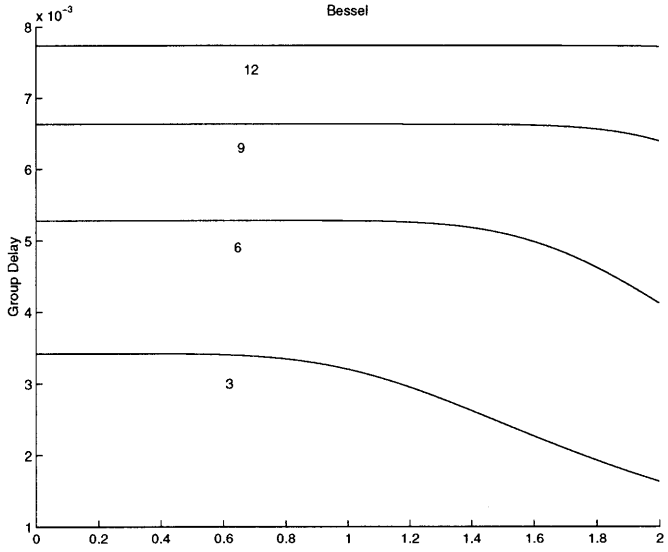

Figure A-2: Bessel filter group delay.

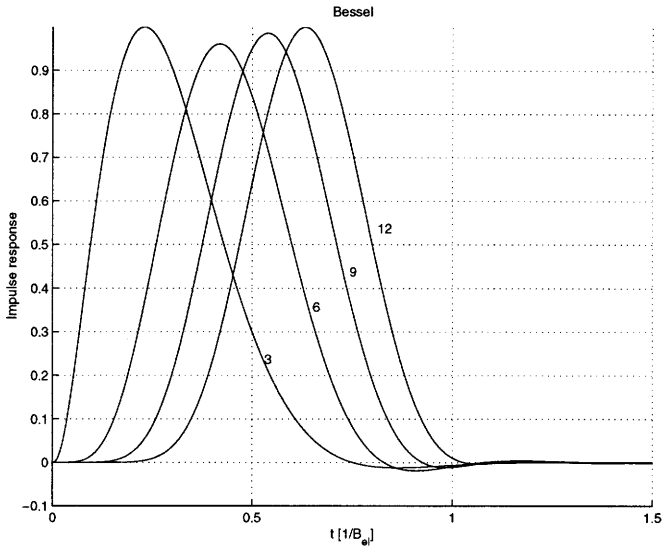

Figure A-3: Bessel filter time impulse response.

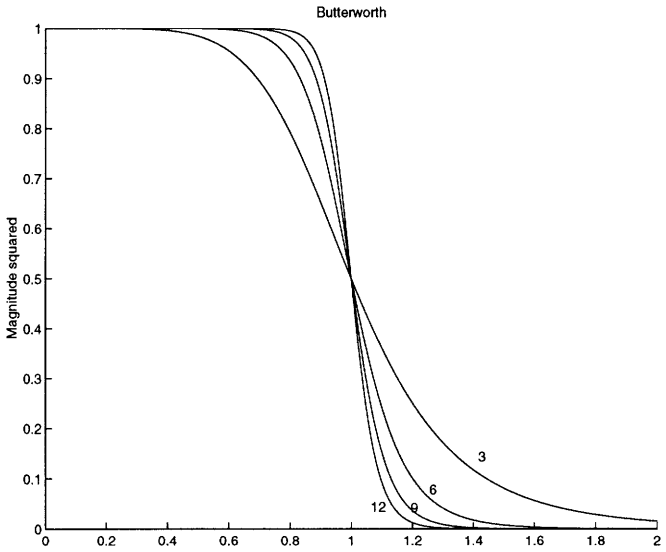

Figure A-4: Butterworth filter squared-magnitude response.

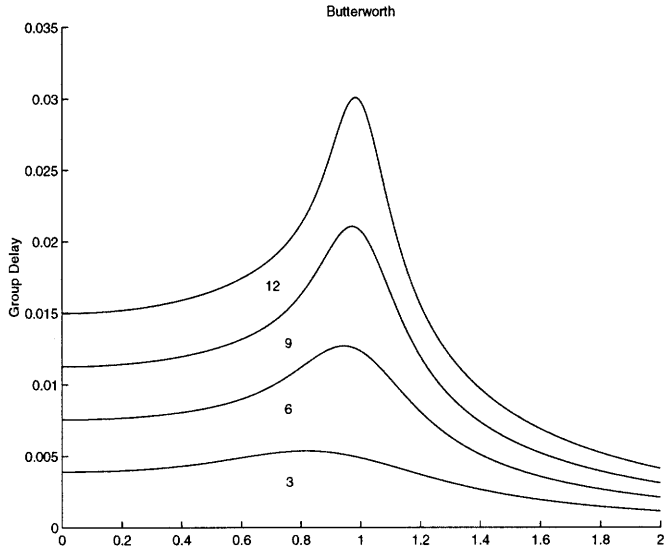

Figure A-5: Butterworth filter group delay.

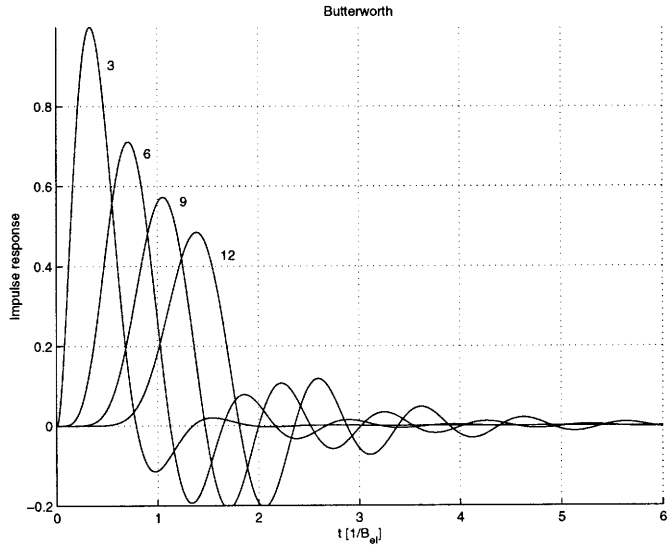

Figure A-6: Butterworth filter time impulse response.

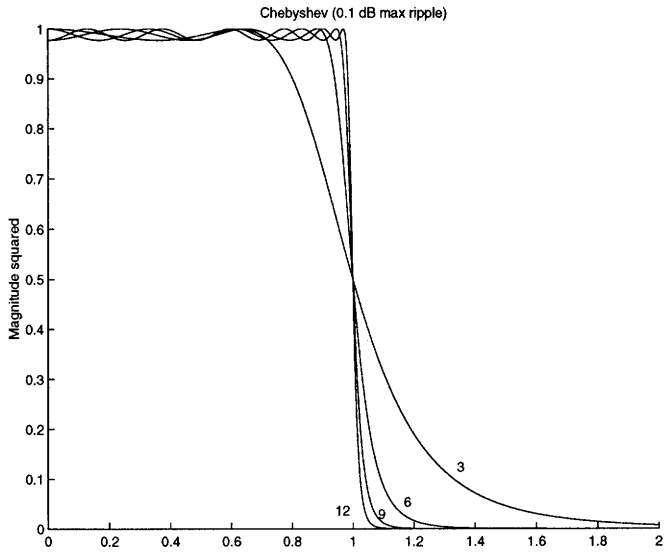

Figure A-7: Chebyshev (0.1 dB max ripple) squared magnitude response.

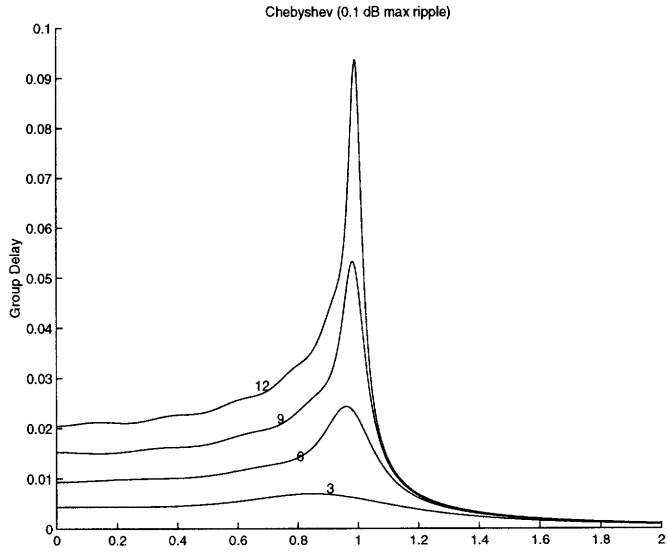

Figure A-8: Chebyshev (0.1 dB max ripple) group delay.

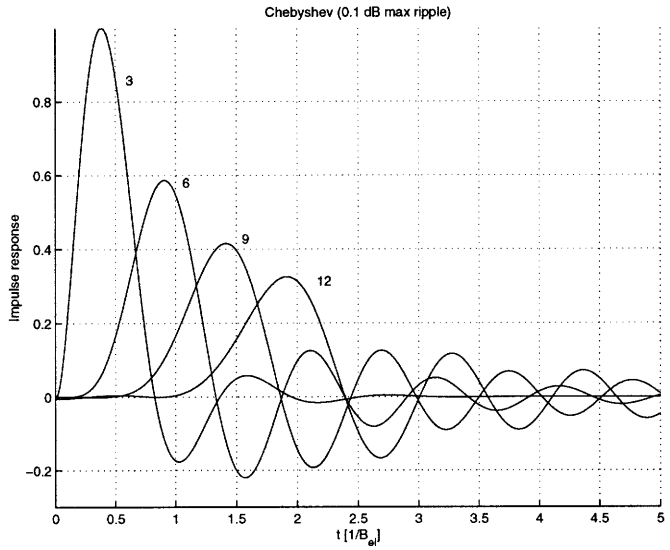

Figure A-9: Chebyshev (0.1 dB max ripple) time impulse response.

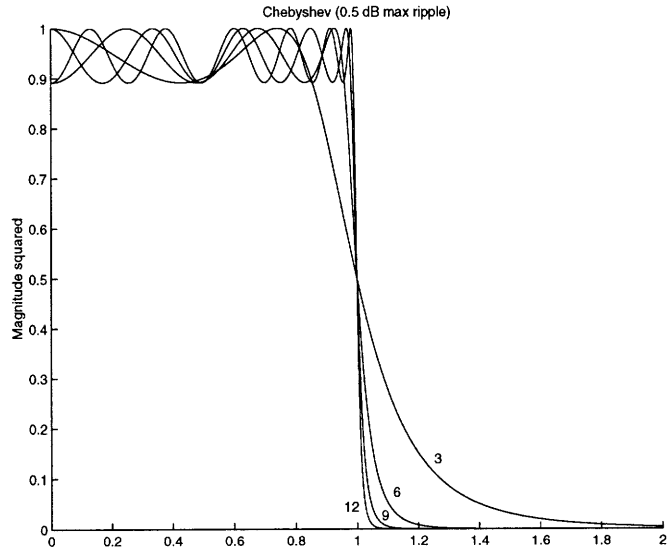

Figure A-10: Chebyshev (0.5 dB max ripple) squared magnitude response.

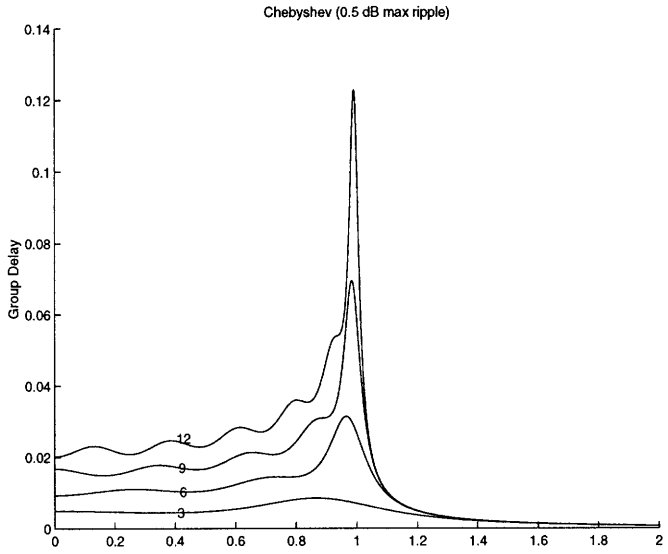

Figure A-11: Chebyshev (0.5 dB max ripple) group delay.

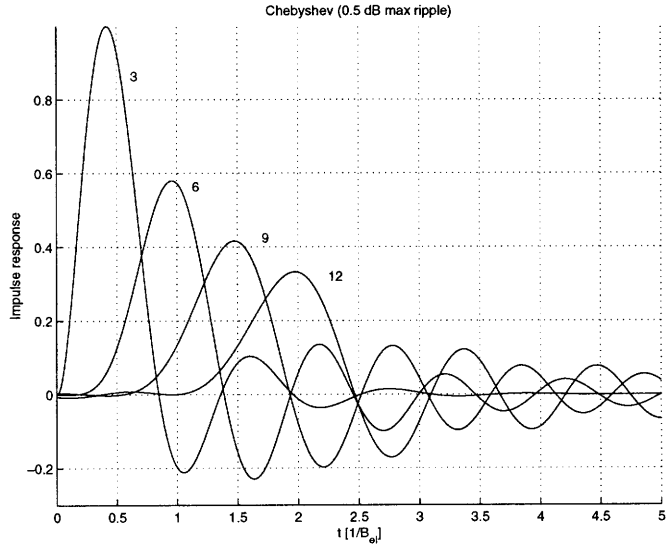

Figure A-12: Chebyshev (0.5 dB max ripple) time impulse response.

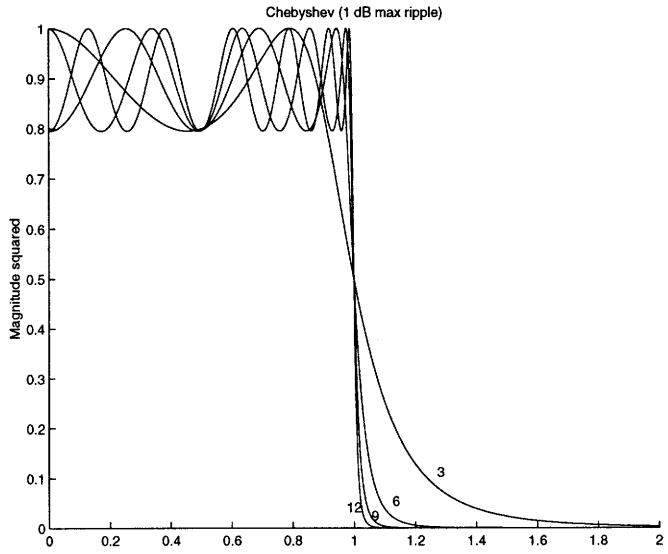

Figure A-13: Chebyshev (1 dB max ripple) squared magnitude response.

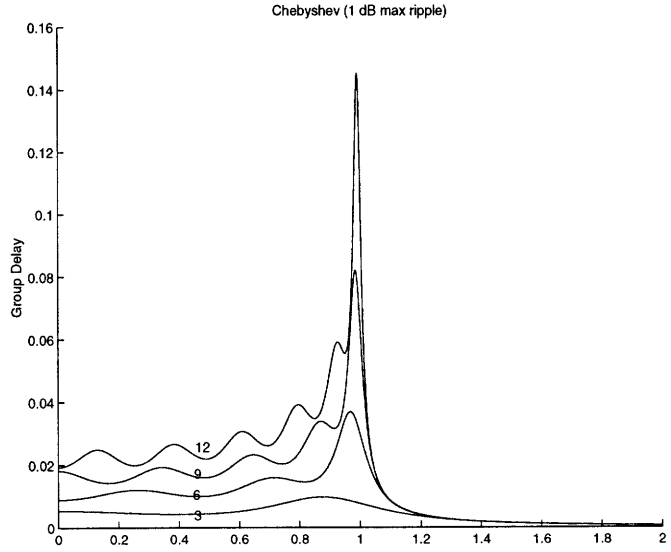

Figure A-14: Chebyshev (1 dB max ripple) group delay.

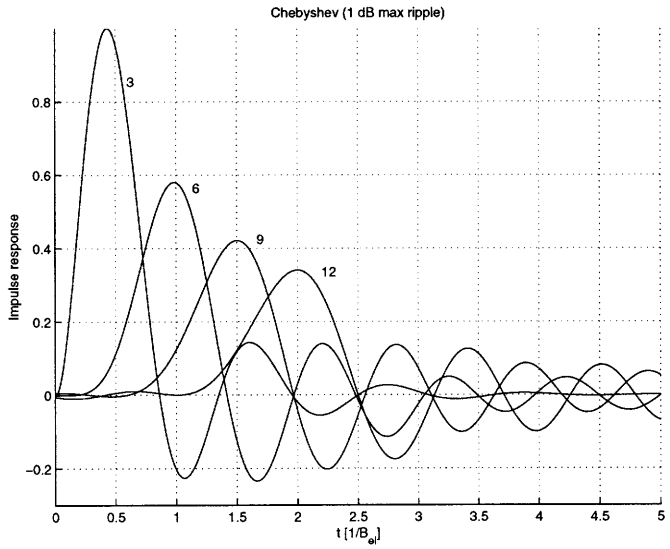

Figure A-15: Chebyshev (1 dB max ripple) time impulse response.

Appendix B

Acoustic Wave Equation Derivaton for Acoustic Phonons

The acoustic wave equation will be important for the derivation of the gain for the Stokes wave in stimulated Brillouin scattering.

This derivation of the acoustic wave equation will use notation from [48, p.490]. The main variables are given in table B.1.

The acoustic wave equation arises from the conservation of mass, the use of Newton's force law, assuming an externally applied force (the applied optical fields) and assuming a viscous drag force.

The first step in the derivation of the acoustic wave equation is the invocation of the conservation of mass which states that the total mass of the system does not change with time:

$$\frac{d}{dt}\int_{V(t)} \rho(\vec{r},t)dv = 0 \tag{B.1}$$

where the integration is over the volume under consideration, $V(t)$. The application

$P(\vec{r},t)$	:	$\left[\frac{N}{m^2}\right]$	fluid pressure
$\rho(\vec{r},t)$	:	$\left[\frac{kg}{m^3}\right]$	fluid mass density
$\vec{U}(\vec{r},t)$	:	$\left[\frac{m}{s}\right]$	fluid velocity

Table B.1: Acoustic variables and units

of the Liebnitz identity and then the use of the divergence theorem allows us to write (B.1) as

$$\begin{aligned}\frac{d}{dt}\int)V(t)\rho(\vec{r},t)dv &= \int_{V(t)} dv + \oint_{A(t)} \rho(\vec{r},t)\vec{U}_A(\vec{r},t)\cdot\hat{n}da \\ &= \int_{V(t)}\left[\frac{\partial\rho(\vec{r},t)}{\partial t} + \nabla\cdot\left(\rho(\vec{r},t)\vec{U}_A(\vec{r},t)\right)\right]dv \qquad \text{(B.2)}\end{aligned}$$

where $\vec{U}_A(\vec{r},t)$ is the velocity of the surface $A(t)$. The Liebnitz identity simply states that the rate of change of the quantity $\rho(\vec{r},t)$, contained in a moving volume $V(t)$ is the sum of the intrinsic rate of change of $\rho(\vec{r},t)$ and the rate at which the moving boundaries are encompassing $\rho(\vec{r},t)$.

For the sake of notational simplicity, the subscript A will be dropped from the fluid velocity,

$$\vec{U}(\vec{r},t) \equiv \vec{U}_A(\vec{r},t)$$

In addition, the functional arguments will also, at times, be dropped.

By substituting (B.2) into (B.1), the following relation is revealed

$$\int_{V(t)}\left[\frac{\partial\rho(\vec{r},t)}{\partial t} + \nabla\cdot\left(\rho(\vec{r},t)\vec{U}_A(\vec{r},t)\right)\right]dv = 0 \qquad \text{(B.3)}$$

Since $V(t)$ is an arbitrary volume, the integrand must vanish, or

$$\frac{\partial\rho(\vec{r},t)}{\partial t} + \nabla\cdot\left(\rho(\vec{r},t)\vec{U}_A(\vec{r},t)\right) = 0 \qquad \text{(B.4)}$$

The next step in the derivation of the acoustic wave equation is to use Newton's Force Law (the ubiquitous F=ma) in integral form:

$$\int_{V(t)} F_x(\vec{r},t)dv = \frac{d}{dt}\int_{V(t)}\rho(\vec{r},t)U_x(\vec{r},t)dv + \int_{V(t)}\mu\frac{\partial^2}{\partial x^2}U_x dv + \int_{V(t)} f_x dv \qquad \text{(B.5)}$$

where the left-hand-side is the total force in the x-direction (units of [N] which makes F_x have units of [N/m^3]), the first term of the right-hand-side (rhs) is the force from pressure gradients in the fluid, the second term on the rhs is the force due to viscosity,

and the last term on the rhs is the externally applied force from optical fields. The rhs contains the coefficient of viscosity with units of [kg/m/s] [42, p.312], which is given by [3, p.303]

$$\mu = \frac{4}{3}\eta_s + \eta_b + \frac{\kappa}{c_p}(\gamma - 1) \tag{B.6}$$

where η_s is the sheer velocity coefficient, η_b is the bulk velocity coefficient, κ is the thermal conductivity, c_p is the specific heat [J/kg/K], and γ is the adiabatic index.

Liebnitz's identity can be used on (B.5) to obtain

$$\int_{V(t)} \left[\frac{\partial}{\partial t}(\rho U_x) + \nabla \cdot (\rho U_x \vec{U})\right] dv = \int_{V(t)} F_x(\vec{r},t)dv - \int_{V(t)} \mu \frac{\partial^2}{\partial x^2} U_x dv - \int_{V(t)} f_x dv \tag{B.7}$$

Again, the integrands must be equal since the volume of integration, $V(t)$, is arbitrary. Equating integrands yields

$$\frac{\partial}{\partial t}(\rho U_x) + \nabla \cdot (\rho U_x \vec{U}) = F_x - \mu \frac{\partial^2 U_x}{\partial x^2} - f_x \tag{B.8}$$

Pressure is related to force through the relation $\vec{F} = -\nabla P$, or $F_x = -\frac{\partial P}{\partial x}$, and simplifies (B.8) to

$$\frac{\partial}{\partial t}(\rho U_x) + \nabla \cdot (\rho U_x \vec{U}) = -\frac{\partial P}{\partial x} - \mu \frac{\partial^2 U_x}{\partial x^2} - f_x \tag{B.9}$$

and this is also true for the other dimensions (y and z):

$$\frac{\partial}{\partial t}(\rho U_y) + \nabla \cdot (\rho U_y \vec{U}) = -\frac{\partial P}{\partial y} - \mu \frac{\partial^2 U_y}{\partial y^2} - f_y \tag{B.10}$$

and

$$\frac{\partial}{\partial t}(\rho U_z) + \nabla \cdot (\rho U_z \vec{U}) = -\frac{\partial P}{\partial z} - \mu \frac{\partial^2 U_z}{\partial z^2} - f_z \tag{B.11}$$

Adding (B.9), (B.10), and (B.11) yields

$$\frac{\partial}{\partial t}(\rho \vec{U}) + \nabla \cdot (\rho \vec{U}\vec{U}) = -\nabla P - \mu \nabla^2 \vec{U} - \vec{f} \tag{B.12}$$

where the term $\vec{U}\vec{U}$ is a second rank tensor.

Next, it is assumed that the field quantities ρ, P, and $\vec{U}$ can be represented as a constant field plus a small fluctuation:

$$\begin{aligned} \rho &= \rho_0 + \rho_1(\vec{r}, t) \\ P &= P_0 + p(\vec{r}, t) \\ \vec{U} &= \vec{U}_0 + \vec{u}(\vec{r}, t) \end{aligned} \tag{B.13}$$

Assume that the fluctuations in pressure and density are small so that

$$\begin{aligned} |\rho_1| &\ll |\rho_0| \\ |p| &\ll |P_0| \end{aligned} \tag{B.14}$$

Assume the fluid to be, on average, at rest so that

$$\vec{U}_0 = 0 \tag{B.15}$$

Substituting (B.14) and (B.15) into the conservaion of mass equation (B.4) yields

$$\frac{\partial \rho_1}{\partial t} + \rho_0 \nabla \cdot \vec{u} = 0 \tag{B.16}$$

Next, the approximations (B.14) and (B.15) are substituted into Newton's Force Equation (B.12) to yield

$$\rho_0 \frac{\partial}{\partial t} \vec{u} = -\nabla p - \mu \nabla^2 \vec{u} - \vec{f} \tag{B.17}$$

The acoustic frequency is assumed to be sufficiently high so that the heat flux in the fiber is zero which implies that the pressure and density are related adiabaticallly by the isentropic acoustic constitutive relation:

$$\frac{\partial \rho}{\partial P} = \frac{\rho}{K} \tag{B.18}$$

or rearranging and substituting (B.13) gives

$$\rho_1 = \left(\frac{\rho_1}{K}\right) p \tag{B.19}$$

where K is the bulk modulus [N/m^2]. This can be substituted into (B.16) to yield

$$\nabla \cdot \vec{u} = -\frac{1}{K}\frac{\partial P}{\partial t} \tag{B.20}$$

or into (B.17) to yield

$$\nabla p = -\rho_0 \frac{\partial \vec{u}}{\partial t} + \mu \nabla^2 \vec{u} - \vec{f} \tag{B.21}$$

To find the acoustic wave equation, take the divergence of (B.21) and insert (B.20) to get

$$\nabla^2 p = \frac{\rho_0}{K}\frac{\partial^2 p}{\partial t^2} - \frac{\mu}{K}\nabla^2 \frac{\partial p}{\partial t} - \nabla \cdot \vec{f} \tag{B.22}$$

where the identity, $\nabla \cdot (\nabla^2 u) = \nabla^2 (\nabla \cdot u)$, was used. This equation can be rewritten and converted from describing the pressure in the medium to describing the density of the medium by noting that the group velocity of the acoustic wave is given by $v_g^2 = \frac{K}{\rho_0}$ and by using (B.19) to get

$$\frac{\partial^2 \rho_1}{\partial t^2} - v_g^2 \nabla^2 \rho_1 - \frac{\mu}{\rho_0}\nabla^2 \frac{\partial \rho_1}{\partial t} = \nabla \cdot \vec{f} \tag{B.23}$$

The external force per unit volume, $\vec{f}$, is given by

$$\vec{f} = -\nabla p_{st} \tag{B.24}$$

where

$$p_{st} = \gamma_e \frac{\epsilon_0 \langle |\vec{E}|^2 \rangle}{4} \tag{B.25}$$

is the contribution to the pressure of a material in the presence of an electric field [3, p.329], and

$$\gamma_e = \rho \frac{\partial \epsilon}{\partial \rho}|_{\rho=\rho_0} \tag{B.26}$$

is the electrostrictive constant. The brackets, $\langle \cdot \rangle$, denote a time average over the optical period.

Appendix C

Derivation of the gain for the Stokes wave in stimulated Brillouin scattering

The following derviation of the Stokes wave in stimulated Brillouin scattering follows the development in [26] and [3], but fills in the gaps and uses MKS units.

The derivation begins by considering a fiber segment with a forward propagating pump wave, ω_p, and a backward propagating stokes wave with frequency ω_s, and a forward propagating acoustic wave with frequency ω_A (see figure C-1).

According to the acoustic phonon dispersion relation:

$$\omega_A = |\vec{k}_A| v \tag{C.1}$$

where v is the velocity of sound. Conservation of energy dictates that

$$\hbar\omega_p = \hbar\omega_s + \hbar\omega_A \tag{C.2}$$

Figure C-1: The pump, Stokes, and acoustic waves in a fiber segment.

or dividing out the $\hbar$ gives the relation

$$\omega_p = \omega_s + \omega_A \tag{C.3}$$

Conservation of momentum yields

$$\vec{k}_p = \vec{k}_s + \vec{k}_A \tag{C.4}$$

and considering the geometry in figure C-1 withh counter-propagating pump and Stokes waves yields

$$\frac{n_p w_p}{c} = -\frac{n_s \omega_s}{c} + \frac{\omega_A}{v} \tag{C.5}$$

where the optical dispersion relation $|\vec{k}| = n\omega/c$ and the acoustic phonon dispersion relationg were used. Reorganizing (C.5) yields

$$\omega_A = \frac{vn}{c}(\omega_p + \omega_s) \tag{C.6}$$

which follows from assuming that $n_p = n_s$, that is, the indices of refraction fo he pump and Stokes waves are approximately equal. Using (C.3) in (C.6) gives

$$\omega_A = \frac{\frac{2vn}{c}\omega_p}{1 + \frac{vn}{c}} \tag{C.7}$$

Since the speed of sound is much slower than the speed of light ($v \ll c/n$), the above simplifies to

$$\omega_A = \frac{2nv}{c}\omega_P \tag{C.8}$$

This implies that

$$|\vec{k}_A| = 2|\vec{k}_p|$$

Consider the forward and backward traveling optical waves represented by

$$E_1(z,t) = A_1(z,t)e^{ik_1 z - i\omega_1 t} + c.c. \tag{C.9}$$

and

$$E_2(z,t) = A_2(z,t)e^{ik_2 z - i\omega_2 t} + c.c. \tag{C.10}$$

where ω_1 does not necessarily equal ω_p and ω_2 does not necessarily equal ω_s. Let the frequency difference between the two oppositely traveling waves be denoted by $\Omega = \omega_1 - \omega_2$.

The acoustic field induced by the optical waves can be described as a material density wave

$$\rho(z,t) = \rho_0 + \left[\rho_1(z,t)e^{ikz - i\Omega t} + c.c.\right] \tag{C.11}$$

where $k = k_1 + k_2 \approx 2k_1$ and ρ_0 is the mean density of the medium. The material density obeys the acoustic wave equation derived in Appendix B.

$$\frac{\partial^2 \rho_1}{\partial t^2} - \frac{\mu}{\rho_0}\nabla^2 \frac{\partial \rho_1}{\partial t} - v_g^2 \nabla^2 \rho_1 = \nabla \cdot \vec{f} \tag{C.12}$$

where, from Appendix B,

$$\begin{aligned} \nabla \cdot \vec{f} &= \nabla \cdot \left[-\nabla\left(\gamma_e \frac{\epsilon_0 \langle |E_1 + E_2|^2 \rangle}{2}\right)\right] \\ &= \frac{\gamma_e \epsilon_0 k^2}{2}\left(A_1 A_2^* e^{ikz - i\Omega t} + c.c.\right) \end{aligned} \tag{C.13}$$

Now substitute this value and (C.11) into the wave equation (C.12) and assuming a slowly varying envelope in space and time ($\partial^2/\partial t^2 \to 0, \partial^2/\partial z^2 \to 0$) to get

$$-2i\Omega \frac{\partial \rho_1}{\partial t} + (\omega_A^2 - \Omega^2 - i\Omega\Gamma)\rho_1 - 2ikv_g^2 \frac{\partial \rho_1}{\partial z} = \gamma_e \epsilon_0 k^2 A_1 A_2^* \tag{C.14}$$

where $\omega_A = v_g k$, and the Brillouin linewidth (FWHM)

$$\Gamma = k^2\left(\frac{\mu}{\rho_0}\right) \tag{C.15}$$

was used. The phonon lifetime is $\tau_p = 1/\Gamma$.

Since the phonon propagation distance is typically small compared to the distance over which the source term on the right hand side of (C.12) varies significantly, $\partial \rho_1/\partial z$

can be dropped for SBS. In addition, assuming steady-state conditions, $\partial\rho_1/\partial t$ also vanishes. Therefore, the steady-state acoustic amplitude is simply

$$\rho_1(z,t) = \frac{\frac{1}{2}\gamma_e\epsilon_0 k^2 A_1 A_2^*}{\omega_A^2 - \Omega^2 - i\Omega\Gamma} \tag{C.16}$$

The evolution of the optical field is given by the electromagnetic wave equation

$$\frac{\partial^2}{\partial z^2}E - \frac{1}{(c/n)^2}\frac{\partial^2}{\partial t^2}E = \mu_0\frac{\partial^2}{\partial t^2}P_{NL} \tag{C.17}$$

The nonlinear polarization term is given by

$$\begin{aligned} P_{NL} &= \epsilon_0\Delta\epsilon E \\ &= \epsilon_0\left(\frac{\partial\epsilon}{\partial\rho}\Delta\rho\right)E \\ &= \frac{\epsilon_0\gamma_e}{\rho_0}\left(\rho_1 e^{ikz-i\Omega t} + c.c.\right)E \end{aligned} \tag{C.18}$$

Since $E = E_1 + E_2$,

$$P_{NL} = \frac{\epsilon_0\gamma_e\rho_1}{\rho_0}\left[A_2 e^{ik_1 z - i\omega_1 t} + A_1 e^{-ik_2 z - i\omega_2 t} + c.c.\right] \tag{C.19}$$

by using (C.9) and (C.10) and choosing only the phase-matched terms.

By substituting C.19), (C.9) and (C.10) into the wave equation (C.17), and making the slowly-varying-envelope approximation yields

$$\begin{aligned} 2ik_1\tfrac{\partial A_1}{\partial z}e^{ik_1 z - i\omega_1 t} - 2ik_2\tfrac{\partial A_2}{\partial z}e^{-ik_2 z - i\omega_2 t} + \tfrac{1}{(c/n)^2}\left(2i\omega_1\tfrac{\partial A_1}{\partial t}e^{ik_1 z - i\omega_1 t} + 2i\omega_2\tfrac{\partial A_2}{\partial t}e^{-ik_2 z - i\omega_2 t}\right) = \\ -\tfrac{\gamma_e\epsilon_0\mu_0}{\rho_0}\left[\rho_1^*\omega_2^2 A_1 e^{-ik_2 z - i\omega_2 t} + \rho_1\omega_1^2 A_2 e^{ik_1 z - i\omega_1 t}\right] \end{aligned} \tag{C.20}$$

This equation can be split into two equations by equating the exponential terms and using the relation $\omega/k = c/n$:

$$\frac{\partial A_1}{\partial z} + \frac{1}{c/n}\frac{\partial A_1}{\partial t} = \frac{i\omega_1\gamma_e\eta_0\eta_0\epsilon_0}{2n\rho_0}\rho_1 A_2 \tag{C.21}$$

and

$$\frac{\partial A_2}{\partial z} + \frac{1}{c/n}\frac{\partial A_2}{\partial t} = \frac{i\omega_2\gamma_e\eta_0\eta_0\epsilon_0}{2n\rho_0}\rho_1^* A_1 \tag{C.22}$$

Substituting $\omega = \omega_1 \approx \omega_2$, assuming steady-state ($\partial/\partial t \to 0$), and substituting (C.16) into the previous coupled equations yields:

$$\frac{\partial A_1}{\partial z} = \frac{i\omega k^2\gamma_e^2\epsilon_0}{4nc\rho_0}\frac{|A_2|^2 A_1}{\omega_A^2 - \Omega^2 - i\Omega\Gamma} \tag{C.23}$$

and

$$\frac{\partial A_2}{\partial z} = \frac{i\omega k^2\gamma_e^2\epsilon_0}{4nc\rho_0}\frac{|A_1|^2 A_2}{\omega_A^2 - \Omega^2 + i\Omega\Gamma} \tag{C.24}$$

Next, the intensities can be found by using the relation

$$I = \frac{|E|^2}{2\eta} = \frac{|E|^2}{2\sqrt{\frac{\mu_0}{\epsilon}}} = \frac{n|E|^2}{2\eta_0} \tag{C.25}$$

This implies

$$\begin{aligned}\frac{\partial}{\partial z}I_1 &= \frac{n}{2\eta_0}\frac{\partial}{\partial z}(A_1^* A_1) \\ &= -\frac{\gamma_e^2\omega^2}{nvc^3\rho_0\Gamma}\frac{(\Gamma/2)^2}{(\omega_A - \Omega)^2 + (\Gamma/2)^2} I_1 I_2\end{aligned} \tag{C.26}$$

The relations $k = k_1 + k_2 \approx 2k_1 = 2\omega n/c$ and $\Omega = 2\pi v/\lambda_{phonon} = vk$ were used in simplifying the above expression. With the following definitions

$$g_0 \equiv \frac{\gamma_e^2\omega^2}{nvc^3\rho_0\Gamma} \tag{C.27}$$

and

$$g\prime \equiv g_0\frac{(\Gamma/2)^2}{(\omega_A - \Omega)^2 + (\Gamma/2)^2} \tag{C.28}$$

(C.26) becomes

$$\frac{\partial I_1}{\partial z} = -g\prime I_1 I_2 \tag{C.29}$$

$\omega_s = \omega_2$	to	f_s
$\omega_p = \omega_1$	to	f_p
ω_A	to	f_A
$\Gamma/2$ (FWHM)	to	Γ (HWHM)
$Lg_0(\Gamma/2)^2$	to	$g\Gamma L_{eff}$

Table C.1: Substitutions to convert this chapter's notation to that found in chapter 6.

and, likewise, it is easy to show

$$\frac{\partial I_2}{\partial z} = -g\prime I_1 I_2 \tag{C.30}$$

with the undepleted pump approximation, or $I_1(z) = constant$, then

$$I_2(z) = I_2(L)\exp\left[g\prime(L-z)I_1\right] \tag{C.31}$$

for each pump frequency. To sum over the pump spectrum to obtain the total Stokes intensity, the pump intensity can be integrated: (we are interested in z=0)

$$I_2(0) = I_2(L)\exp\left[\int_{-\infty}^{\infty} g\prime L I_1(\omega_1)\right] \tag{C.32}$$

In addition, loss in the fiber can be accounted for by adding a constant term $e^{-\alpha L}$. Hence, the above equation becomes

$$I_2(0) = I_2(L)\exp\left[g_0 L(\Gamma/2)^2 \int_{-\infty}^{\infty} \frac{I_1(\omega_1)}{(\omega_A-\Omega)^2+(\Gamma/2)^2} d\omega_1 - \alpha L\right] \tag{C.33}$$

Note that $\Omega = \omega_1 - \omega_2$,

$$I_2(0) = I_2(L)\exp\left[g_0 L(\Gamma/2)^2 \int_{-\infty}^{\infty} \frac{I_1(\omega_1)}{(\omega_1-\omega_2-\omega_A)^2+(\Gamma/2)^2} d\omega_1 - \alpha L\right] \tag{C.34}$$

This equation can be converted into the notation given in chapter 6 by making the substitutions found in table C.1.

The last entry in table C.1 implies that

$$g = \frac{L}{L_{eff}} \frac{2\pi^2 \gamma_e^2 f_p^2}{nvc^3 \rho_0} \tag{C.35}$$

where

$$L_{eff} = \frac{1 - e^{-\alpha L}}{\alpha} \tag{C.36}$$

Rewriting (C.34) with the new notation specified in table C.1 yields

$$I_s(0) = I_s(L) \exp \left[\underbrace{g\Gamma L_{eff} \int_{-\infty}^{\infty} \frac{I_p(f_p)}{\Gamma^2 + (f_p - f_s - f_A)^2} df_p}_{\text{SBS Gain, } G} - \alpha L \right] \tag{C.37}$$

This equation shows that the SBS gain in long fibers is given by the convolution between the pump spectrum and the spontaneous Brillouin linewidth. For the case of a CW pump wave, where $I_p(f) = I_0 \delta(f)$, the steady-state SBS gain is given by

$$G_{CW} = \frac{g I_0 L_{eff}}{\Gamma} \tag{C.38}$$

Appendix D

Multiresolution Split-step Fourier Transform Method

The split-step Fourier transform method is useful for quickly propagating a waveform along a fiber in optical simulations [2, p.50]. The normalized equation that governs wave propagation in lossy fibers is [2, p.165].

$$i\frac{\partial u}{\partial \xi} + \frac{\partial^2 u}{\partial \tau^2} + |u|^2 u = -i\Gamma u \tag{D.1}$$

The prescription for the split-step Fourier transform method is as follows: (1) divide the optical fiber into N discrete segments (2) alternately designate the segments as dispersive only or nonlinear only, (3) propagate the signal in each segement. The dispersive effects (segments) of the fiber are computed in the frequency domain whereas the nonlinear effects (segments) are computed in the time domain. Switching from one domain to the other is accomplished through the FFT. The computational advantage of the Fourier transform method lies in the usage of the FFT algorithm ($O(N\log(N))$ operations per step). One alternative to the split-step Fourier method is to do the computation in the time domain only. This would require $O(N^2)$ operations per convolution, which is tremendously slower for large N.

A further improvement upon the split-step Fourier transform method is the usage of a variable step size (i.e. multiresolution). The step size or fiber segment length is

equal to some fraction of the minimum of the dispersion and nonlinear lengths. In the simulations in this paper, the step was chosen according to

$$dz = \frac{\min(L_D, L_{NL})}{100} \tag{D.2}$$

where $L_D = T_0^2/|\beta_2|$ is the dispersion length and $L_{NL} = 1/\gamma P_0$ is the nonlinear length, i.e. the length over which dispersion or nonlinearities are noticable. By adjusting the spatial step size by monitoring the change in the nonlinear length brought about by a change in the power of the optical signal, there is a great computational advantage when considering a signal that experiences large losses along the fiber. The RZ duobinary nonlinear nonrepeatered transmission experiments in silica core fiber, where the signal begins with high power and subsequently experiences large losses, is an example of where multiresolution is advantageous.

Another reasonable alteration to the split-step algorithm is to ignore the nonlinearity of the fiber at the point where the nonlinear length is much greater (a factor of 100 in the simulations used in this thesis) than the length of the remaining fiber. Linear propagation is very fast and only requires only one Fourier transform pair.

The error of the split-step method is related to the commutation of the dispersion and nonlinear operators, which is unfortunately unbounded. Therefore there is no nice mathematical formula bounding the error of this method. Nevertheless, despite this mathematical complication, this method, if used with a narrow enough grid often subtends insightful answers. Two checks that one should use on the split-step Fourier transform is to (1) use a smaller step size and see whether this gives a similar answer, and (2) to check that the energy of the signal depletes by only the fiber loss.

Appendix E

Glossary

Back-to-Back Sensitivity Sensitivity at zero dispersion. In other words, the sensitivity when the transmitter is directly connected to the receiver.

BER Bit error rate.

dBm A unit of power, $P(\text{dBm}) = 10\log(P(\text{W})/1\text{mW})$. Therefore -30 dBm, 0, and 10 dBm correspond to a power of 1 μW, 1 mW, and 10 mW respectively.

DCF, Dispersion Compensating Fiber Fiber that is used to compensate channel dispersion. Often refers to negative dispersion fiber which will compensate SCF.

Direct Detection Refers to a square law detector with no homo- or heterodyning. In an optical system a direct detector is often a *pin* photodiode.

Dispersion Penalty or Dispersion Power Penalty The additional incremental received power needed to attain at 10^{-9} BER due to degradations from dispersion in the fiber.

Mark Another name for a "1" in a digital communications system.

Power Penalty The additional incremental received power needed to attain at 10^{-9} BER.

SCF, Silica Core Fiber Refers to the most popular fiber that has zero dispersion at 1.3μm but approximately 17 ps/nm/km dispersion at 1.5μm wavelengths. This fiber is currently the lowest loss fiber with losses of 0.173 dB/km.

Sensitivity The necessary received power needed to achieve a $10^{-}9$ BER.

Space Another name for a "0" in a digital communications system.

Total Dispersion or Dispersion Often refers to the dispersion (ps/nm/km) times the length of the fiber (km) and hence has units of (ps/nm).

Bibliography

[1] Govind Agrawal. *Fiber-Optic Communication Systems.* John Wiley and Sons, Inc., New York, 1992.

[2] Govind Agrawal. *Nonlinear Fiber Optics.* Academic Press, New York, 1995.

[3] Robert W. Boyd. *Nonlinear Optics.* Academic Press, Inc., Boston, 1992.

[4] John C. Cartledge and Aly F. Elrefaie. Effect of chirping-induced waveform distortion on the performance of direct detection receivers using traveling-wave semiconductor optical preamplifiers. *Journal of Lightwave Technology, Vol. 9, No.2, Feb.*, 1991.

[5] Andrew R. Chraplyvy. Limitations on lightwave communications imposed by optical fiber nonlinearities. *Lucent Technologies Technical Memorandum*, 1989.

[6] Milorad Cvijetic. *Coherent and Nonlinear Lightwave Communications.* Artech House, Boston, 1996.

[7] Emmanuel Desurvire. *Erbium-doped fiber amplifiers: principles and applications.* John Wiley and Sons, Inc., New York, 1994.

[8] A. H. Gnauck et al. One terabit/s transmission experiment. In *OFC*, volume PD-20, 1996.

[9] E. Yamada et al. Generation of terabit per second optical data pulse train. *Electonics Letters*, 31, 1995.

[10] H. Onaka et al. 1.1 tb/s wdm transmission wdm transmission over 150 km 1.3 μm zero-dispersion single-mode fiber. In *OFC*, volume PD-19, San Jose, USA, February 1996.

[11] T. Morioka et al. 100 gbit.s $\times$ 10 channel otdm/wdm transmission using a single supercontinuum wdm source. In *OFC*, volume PD-21, 1996.

[12] T. Franck, P.B. Hansen, T.N. Nielsen, and L. Eskildsen. Novel duobinary transmitter. *Not published*, 1996.

[13] T. Franck, T.N. Nielsen, and A. Stentz. Experimental verification of sbs suppression by duobinary modulation. *Not published*, 1996.

[14] Thorkild Franck, Torben Nielsen, and Andrew Stentz. Experimental verification of sbs suppression by duobinary modulation. In *ECOC*. ??, September 1997.

[15] Robert M. Gagliardi and Sherman Karp. *Optical Communications.* John Wiley and Sons, Inc., New York, second edition, 1995.

[16] Solomon W. Golomb. *Digital Communications with Space Applications.* Prentice-Hall, Inc., Englewood Cliffs, NJ, 1964.

[17] I.S. Gradshteyn and I.M. Ryzhik. *Table of Integrals, Series, and Products.* Academic Press, New York, 1980.

[18] X. Gu, S.J. Dodds, L.C. Blank, D.M. Spirit, S.J. Pycock, and A.D. Ellis. Duobinary technique for dispersion reduction in high capacity optical systems — modelling, experiment and field trial. *IEE Proc.-Optoelectron. Vol 143, No.4, August*, 1996.

[19] Waldemar Hauk, Bross Franz, and Manfred Ottka. The calculation of error rates for optical fiber systems. *IEEE Transactions on Communications, Vol. COM-26, No.7, July*, 1978.

[20] Hermann A. Haus. *Electromagnetic Noise and Quantum Optical Measurements.* Not yet published.

[21] K.O. Hill, D.C. Johnson, B.S. Kawasaki, and R.I. MacDonald. Cw three-wave mixing in single-mode optical fibers. *Journal of Applied Physics 49(10), October*, 1978.

[22] T. Ito, T. Ono, Y. Yano, K. Fukuchi, H. Yamazaki, M. Yamaguchi, and K. Emura. Tuj1 — feasibility study on over 1 bit/s hz high spectral efficiency wdm with optical duobinary coding and polarization interleave multiplexing. In *OFC*, Dallas, Texas, February 1997.

[23] Michel C. Jeruchim, Philip Balaban, and K. Sam Shanmugan. *Simulation of Communication Systems.* Plenum Press, New York, 1992.

[24] Leonid Kazovsky, Sergio Bendetto, and Alan Willner. *Optical Fiber Communication Systems.* Artech House, Inc., Boston, 1996.

[25] Adam Lender. Correlative digital communication techniques. *IEEE Transactions on Communication Technology, vol. COM-12, pp.128-135, Dec.*, 1964.

[26] Adam Lender. Correlative level coding for binary-data transmission. *IEEE Spectrum, pp.104-115, Feb.*, 1966.

[27] E. Lichtman, R.G. Waarts, and A.A. Friesem. Stimulated brillouin scattering excited by a modulated pump wave in single-mode fibers. *Journal of Lightwave Technology, Vol.7, No.1, January*, 1989.

[28] W.H. Loh, R.I. Laming, A.D. Ellis, and D. Atkinson. 10 gb/s transmission over 700 km of standard-single mode fiber with 10-cm chirped fiber grating compensator and duobinary transmitter. *IEEE Photonics Technology Letters, Vol.8, No.9., September*, 1996.

[29] C. Lorattanasane and K. Kikuchi. Design theory of long-distance optical transmission systems using midway optical phase conjugation. *Journal of Lightwave Technology*, 15(6), June 1997.

[30] P.D. Maker and R.W. Terhune. *Phys. Rev. 137, A801*, 1965.

[31] D. Marcuse. Derivation of analytical expressions for the bit-error probability in lightwave systems with optical amplifiers. *Journal of Lightwave Technology, Vol. 8., No. 12, December*, 1990.

[32] D. Marcuse. Calculation of bit-error probability for a lightwave system with optical amplifiers and post-detection gaussian noise. *Journal of Lightwave Technology, Vol. 9, No. 4, April*, 1991.

[33] M. Matsumoto and H. A. Haus. Streched-pulse long-distance fiber communications. In *OFC Technical Digest Paper ThN6*, 1997.

[34] David J. Morris. *Pulse Code Formats for Fiber Optical Data Communications.* Marcel Dekker, Inc., New York, 1983.

[35] R. J. Nuyts, L. D. Tzeng, O. Mizuhara, and P. Gallion. Effect of transmitter speed and receiver bandwidth on the eye margin performance of a 10-gb/s optical fiber transmission system. *IEEE Photonics Technology Letters*, 9(4), April 1997.

[36] Athanasios Papoulis. *Probability, Random Variables, and Stochastic Processes.* McGraw-Hill Book Company, New York, 1965.

[37] D. Penninckx, M. Chabat, L. Pierre, and J.-P. Thiery. The phase-shaped binary transmission (psbt): A new technique to transmit far beyond the chromatic dispersion limit. *IEEE Photonics Technology Letters, Vol.9, No.2, February*, 1997.

[38] S. D. Personick. Receiver design for optical fiber systems. *Proceeding of the IEEE, Vol. 65, No. 12, December*, 1977.

[39] S. D. Personick, P. Balaban, and J. H. Bobsin. A detailed comparison of four approaches to the calculation of the sensitivity of optical fiber system receivers. *IEEE Transactions on Communications, May*, 1977.

[40] S.D. Personick. Receiver design for digital fiber optic communication systems. *The Bell System Technical Journal, July-August*, 1973.

[41] A. J. Price and N. Le Mercier. Reduced bandwidth optical digital intensity modulation with improved chromatic dispersion tolerance. *Electronics Letters, Vol.31, No.1, January 5,*, 1995.

[42] A.J. Price, L. Pierre, R. Uhel, and V. Havard. 210 km repeaterless 10 gb/s transmission experiment through nondispersion-shifted fiber using partial response scheme. *IEEE Photonics Technology Letters, Vol.7, No.10, October*, 1995.

[43] Baron Rayleigh and John William Strutt. *The Theory of Sound.* Dover Publications, New York, 1945.

[44] C. Britton Rorabaugh. *Digital Filter Designer's Handbook.* McGraw-Hill, New York, 1997.

[45] F.F. Ruhl and R.W. Ayre. Explicit expressions for the receiver sensitivity and system penalties of optically preamplified direct-detection systems. *IEEE Photonics Technology Letters, Vol.5, No.3, March*, 1993.

[46] Sam K. Shanmugam. *Digital and Analog Communication Systems.* John Wiley and Sons, New York, 1979.

[47] N. Shibata, R.P. Braun, and R.G. Waarts. Phase-mismatch dependence of efficiency of wave generation through four-wave mixing in single-mode optical fiber. *IEEE Journal of Quantum Electronics, Vol. QE-23, No.7., July*, 1987.

[48] R. G. Smith. Optical power handling capacity of low loss optical fibers as determined by stimulated raman and brillouin scattering. *Applied Optics*, 11(11), November 1972.

[49] David H. Staelin, Ann W. Morgenthaler, and Jin Au Kong. *Electromagnetic Waves.* Prentice Hall, Englewood Cliffs, New Jersey, 1994.

[50] Lightwave systems with optical amplifiers. Olsson, n.a. *Journal of Lightwave Technology*, 7(7), July 1989.

[51] M.C. Tatham, X. Gu, L.D. Westbrook, G. Sherlock, and D.M. Spirit. 200 km transmission of 10 gbit.s directly modulated dfb signals using mid span spectral inversion in a semiconductor optical amplifier. In *ECOC*, volume We.B.4.3, Firenze, Italy, 1994.

[52] Sheldon Walklin and Jan Conradi. Effect of mach-zender modulator dc extinction ratio on residual chirp-induced dispersion in 10 gb/s binary and am-psk duobinary lightwave systems. *IEEE Photonics Technology Letters*, 9(10), October 1997.

[53] Sheldon Walklin and Jan Conradi. On the relationship between chromatic dispersion and transmitter filter response in duobinary optical communication systems. *IEEE Photonics Techonology Letters, Vol.9, No.7, July*, 1997.

[54] Arthur B. Williams and Fred J. Taylor. *Electronic Filter Design Handbook.* McGraw-Hill, New York, 1995.

[55] Y. Yamamoto and T. Kirmura. Coherent optical fiber transmission systems. *IEEE Journal of Quantum Electronics*, QE-17, 1981.

[56] Y. Yano, K. Fukuchi, T. Ito, H. Yamazaki, M. Yamaguchi, and K. Emura. 2.6 terabit/s wdm transmission experiment using optical duobinary coding. In *22nd European Conference on Optical Communication*, Oslo, Norway, 1996.

[57] A. Yariv. *Optical Electronics.* Saunders College Publishing, Philadelphia, 1991.

[58] K. Yonenaga, S. Kuwano, S. Norimatsu, and N. Shibata. Optical duobinary transmission system with no receiver sensitivity degradation. *Electronics Letters, Vol.31, No.4, February 16*, 1995.